RASA MARDOSAITĖ

SYNTHESIS, STRUCTURE AND ELECTROCHEMICAL PROPERTIES OF S-CONTAINING Co–Mo OXIDE FILMS

DOCTORAL DISSERTATION

Kaunas
2019

KAUNAS UNIVERSITY OF TECHNOLOGY

RASA MARDOSAITĖ

SYNTHESIS, STRUCTURE AND ELECTROCHEMICAL PROPERTIES OF S-CONTAINING Co–Mo OXIDE FILMS

Doctoral Dissertation
Physical Sciences, Chemistry (03P)

Kaunas, 2019

This doctoral dissertation was prepared at Kaunas University of Technology, Faculty of Chemical Technology, Department of Physical and Inorganic Chemistry during the period of 2014–2018.

Scientific Supervisor:

Prof. Dr. Eugenijus VALATKA (Kaunas University of Technology, Physical Sciences, Chemistry, 03P)

Doctoral dissertation has been published in:
http://ktu.edu

Editor:

Antony Richard Bexon (Centre of Foreign Languages, Kaunas University of Technology)

ISBN 978-609-02-1560-9

The bibliographic information about the publication is available in the National Bibliographic Data Bank (NBDB) of the Martynas Mažvydas National Library of Lithuania.

KAUNO TECHNOLOGIJOS UNIVERSITETAS

RASA MARDOSAITĖ

SIEROS TURINČIŲ Co–Mo OKSIDINIŲ DANGŲ SINTEZĖ, STRUKTŪRA IR ELEKTROKATALIZINĖS SAVYBĖS

Daktaro disertacija
Fiziniai mokslai, chemija (03P)

Kaunas, 2019

Disertacija rengta 2014-2018 metais Kauno technologijos universiteto Cheminės technologijos fakultete Fizikinės ir neorganinės chemijos katedroje.

Mokslinis vadovas:

Prof. dr. Eugenijus VALATKA (Kauno technologijos universitetas, fiziniai mokslai, chemija, 03P)

Interneto svetainės, kurioje skelbiama disertacija, adresas:
http://ktu.edu

Redagavo:

Antony Richard Bexon (Užsienio kalbų centras, Kauno technologijos universitetas)

ISBN 978-609-02-1560-9

Leidinio bibliografinė informacija pateikiama Lietuvos nacionalinės Martyno Mažvydo bibliotekos Nacionalinės bibliografijos duomenų banke (NBDB).

TABLE OF CONTENTS

SYMBOLS AND ABBREVIATIONS

a, b	Tafel slope constants
AAS	atomic absorption spectroscopy
AFM	atomic force microscopy
AP	acidification potential
ATTM	ammonium tetrathiomolybdate
at. %	atomic percentage
a.u.	arbitrary units
CC	carbon cloth
$Co{-}P_i$	cobalt phosphate catalyst
CV	cyclic voltammetry / voltammogram
DSSC	dye-sensitized solar cell
E	electrode potential
E°	standard electrode potential
e^-	electron
EDX	energy dispersive X-ray spectroscopy
EPD	electrophoretic deposition
FD	formamidine disulfide
FTO	fluorine doped tin oxide
FT-IR	Fourier transform infrared spectroscopy
GWP	global warming potential
h^+	hole
HER	hydrogen evolution reaction
I	current
IEA	International Energy Agency
IED	ion exchange deposition
ITO	indium doped tin oxide
j	current density
M	metal
MOF	metal organic framework
NHE	normal hydrogen electrode
OER	oxygen evolution reaction
PEC	photoelectrochemical cell
PEM	polymer-electrolyte membrane
PEN	polyethylene naphthalate
PV	photovoltaic
R	resistance
R_a	average roughness
R^2	coefficient of determination
RGO	reduced graphene oxide
RHE	reversible hydrogen electrode
SA	self-assembled
SEM	scanning electron microscopy
SHE	standard hydrogen electrode
SILAR	successive ionic layer adsorption and reaction

SOE	solid oxide electrolyzer
t	time
T-NT	titania nanotube
TM	transition metal
TMTU	tetramethyl thiourea
TU	thiourea
UV–Vis	Ultraviolet–visible spectroscopy
XRD	X-ray diffraction
XPS	X-ray photoelectron spectroscopy
η	overpotential
θ	Bragg‘s diffraction angle
ΔG	Gibbs‘ free energy change
ΔH	enthalpy change

INTRODUCTION

Relevance of the work. The energy used today is based on fossil fuels, which have been stored naturally over millions of years. In order to shift the world to a synthetic fuel, like hydrogen, the economy must first be convinced to pay for H_2 production. In this regard, water electrolysis would be one of the most economically and environmentally friendly, renewable, and a clean method to produce hydrogen. However, one of the greatest challenges is to find the path toward an effective and noble-metal-free electrocatalyst formation.

Recently, amorphous cobalt and molybdenum sulfide systems showed an increased interest in individual catalytic features. Particularly, the distinctive activity characteristics that were prescribed for cobalt sulfides while the stability features were mostly expressed for molybdenum compounds. Substantial benefits could probably be provided if synergy would affect the mixed composition of Co and Mo sulfide compounds. However, the development of molybdenum sulfide-based materials is limited by the lack of economically and environmentally friendly Mo and S precursors. In order to overcome this drawback, the aqueous solution of an alternative composition with simple inorganic Co and Mo salts and thiourea as a S source may be of great importance when compared to the most commonly used expensive complex precursors.

The aim of the work was to form S-containing cobalt-molybdenum catalytic films on conductive glass substrate using the potentiodynamic deposition method, and to study their structure and electrocatalytic performance for hydrogen evolution reaction in an aqueous neutral phosphate solution.

In order to achieve the aim of the work, the following tasks were formulated:

1. To prepare S-containing cobalt oxide, molybdenum oxide, and cobalt-molybdenum oxide films on conductive glass substrate and to propose possible deposition mechanism of these films.
2. To investigate the structure and morphology of the deposited films and to compare their electrocatalytic performance in a pH 7 phosphate buffer solution.
3. To optimize the synthesis conditions of mixed S-containing cobalt-molybdenum oxide films by assessing the effects of various deposition parameters on films electrocatalytic activity and stability behavior in a hydrogen evolution reaction.

Scientific novelty of the dissertation. For the first time, an electrodeposition bath containing thiourea and ammonium molybdate as the S and Mo precursors was introduced for the synthesis of various S-containing molybdenum and cobalt-molybdenum oxide films.

The optimized electrolysis conditions, enabling synthesis of high quality, stable and electroactive S-containing cobalt-molybdenum oxide films, were determined. The activation-induced effect was suggested as the reason for the enhanced catalytic performance during electrolysis in a phosphate buffer solution.

Practical significance of the dissertation. The results presented in the dissertation expand the knowledge in the development of new materials for electrocatalytic hydrogen generation from a neutral aqueous solution. The

combination of the separate Mo and S precursors, presented in this work, can be suggested as an alternative bath for the dominant and widespread use of the more expensive and practically limited reactants. It was demonstrated that Co–Mo–O–S films are able to maintain the harsh HER conditions at 5 mA/cm^2.

Approval and publications of research results. The results of the research are presented in 6 publications: 3 scientific articles in the journals indexed in *Clarivative Analytics Web of Science* database and 3 articles in the proceedings of scientific conferences.

Structure and content of the dissertation. The dissertation consists of three main chapters; covering a literature review, the applied methodology, and the results of the research and their discussion. The thesis begins with an introduction and ends with the conclusions, a list of references and a list of publications on the topic of the dissertation. The dissertation text covers 100 pages, it features 6 tables and 53 figures. The list of references includes 147 bibliographic sources.

Statements presented for the defense:

1. Highly active and stable Co–Mo–O–S electrocatalyst can be developed by a one-step electrodeposition technique.
2. Cathodic polarization of Co–Mo–O–S films in phosphate buffer provoke the *in-situ* activation of these HER electrocatalysts.
3. The optimization of Co–Mo–O–S synthesis condition is essential for the synergy of components in terms of film activity-stability characteristics.

1. LITERATURE REVIEW

1.1. Hydrogen production and storage: current status and trends

1.1.1. World energy consumption and forecast for H_2

The 21st century is challenged by a striking appetite for energy. In the past decades, the world's energy consumption has increased rapidly; due to the growth of the population and rising standards of living. According to the forecasts of the International Energy Agency [1], global energy needs will expand by 30% between 2017 and 2040, together with an increase of the population from 7.4 billion today to more than 9 billion in 2040. Typical energy producer-consumer calculations are going to be blurred by an impact of the major developing countries, led by India together with China and Southeast Asia.

The growing demand for energy is predicted to coinside with the cleaner energy consumption. As carbon-based resources have fueled technological advances from the Industrial Revolution to the present day, fossil fuels still remains a global leader in primary energy supply (coal 30%, liquid oil 33%, natural gas 22%) [2, 3]. Inevitably, environmental issues related to global warming and climate change, along with concerns about greenhouse-gas emissions from fossil-fuel sources and also their limited nature and nonhomogeneous distribution stimulate the deep interest in alternative energy sources [4]. According to the European Environment Agency [5], the European Union is currently on track (~17%) to meet its renewable energy target (20%) for 2020. Renewable electricity, driven by wind power and solar photovoltaic, and transport sector act together with renewable heating and cooling, which dominants the renewable market sector in Europe. For example, in Lithuania (as well as in the other 17 Member States in 2015), renewable heating and cooling represented over half of the national gross final consumption of renewables.

However, in a worldwide context, developing countries in Asia account for two-thirds of the global energy consumption and make a major impact on global statistics and energy trends. For instance, “energy revolution with a fight against pollution“ became a new choice for China. In parallel with China, the global statistics are at the edge of low-carbon energetics. World Energy Outlook 2017, reported by IEA, noted a bright future for renewables working together with natural gas.

Considering the historical development of energy carriers, zero-carbon and hydrogen rich fuels have been considered as an ideal, advanced and innovative type of energy [2]:

$$\text{C (coal)} \rightarrow \text{–CH}_2\text{– (oil)} \rightarrow \text{CH}_4 \text{ (natural gas)} \rightarrow \text{H}_2 \text{ (hydrogen)}$$

Currently, pure H_2 is one of the most favorable fuels of choice. Even though it still requires significant efforts in research and development (R&D), a lot of experience has been gained since its first applications [6]. A brief history of hydrogen was summarized by Grochala and Edwards [7]. It was modified according to the current status and is shown in Figure 1.1.

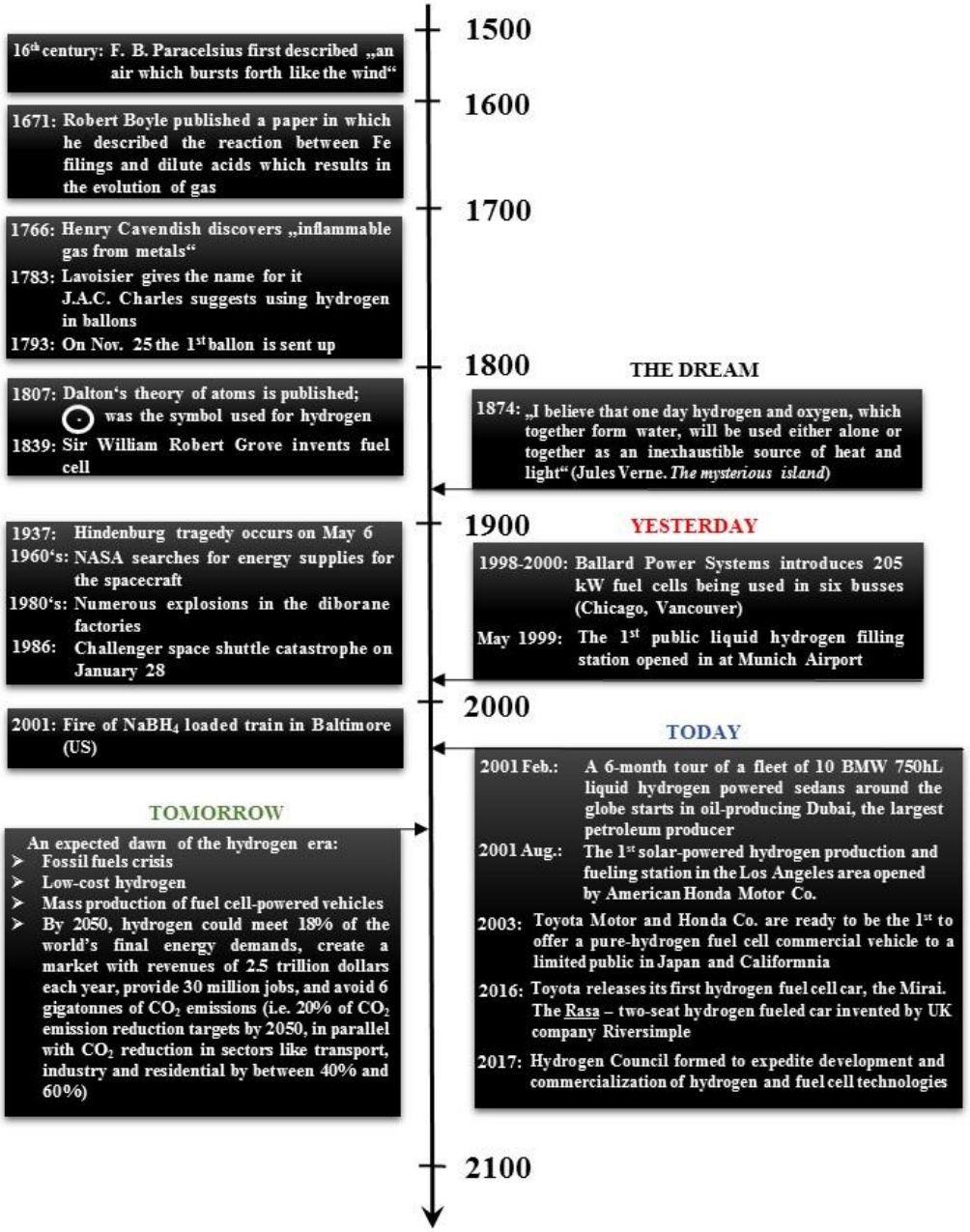

Fig. 1.1. Brief history and timeline of hydrogen (Modified from Ref. [7])

Numerous advantages of hydrogen, as a sustainable energy carrier, are based on the experience, fundamental knowledge, and current research. According to the ideal plan, hydrogen can be produced and consumed with zero-carbon emissions. It also has high-energy conversion efficiencies, abundance, different forms of storage, long distance transportation and easy conversion to other forms of energy [4].

However, before hydrogen can become a significant part of the global energy, economical and technical challenges (such as production, transport, storage, and distribution) must be addressed. Beforehand, production was a key combination of issues. For example, the energy used today is still based on fossil fuels, which were stored naturally over millions of years. Therefore, humans are accustomed to paying only the mining costs of fossil fuels. In order to shift the world to a synthetic fuel like hydrogen, the economy must first be convinced to pay for H_2 production [2].

1.1.2. Hydrogen production methods

Even though hydrogen is the most abundant element in the universe, it cannot be found in its pure state in nature. The main methods to produce hydrogen can be classified by the source of raw material. Fossil fuels, biomass and water decomposition based technologies are typically outlined as the potential hydrogen production methods. Up to 95% of hydrogen is produced from fossil fuels, around 4% from water and <1% from other sources [8].

1) Fossil fuels processing. Fossil fuels processing technologies convert hydrogen containing materials (such as oil, coal, natural gas) into a hydrogen rich stream. Hydrocarbons reforming and coal gasification are the most common employed methods. Steam reforming, partial oxidation, and autothermal reforming are the three primary reforming techniques that produce a gas stream composed of H_2, CO and CO_2. In general, all three reforming processes can be characterized briefly and expressed by reactions of methanol fuel which can be made from natural gas [9, 10]:

a. Steam reforming is endothermic and requires an external heat source. It does not demand oxygen to drive the process, has a lower operating temperature and a higher H_2/CO ratio (~3:1) than the other two techniques. However, it has the highest emissions. For methanol fuel it can be expressed as follows:

$$CH_3OH + H_2O \rightarrow CO_2 + 3H_2 \quad \Delta H = +49\ \text{kJ/mol} \qquad (1.1)$$

b. Partial oxidation is an exothermic process, driven by the heat of oxidation reaction itself, that converts hydrocarbons to H_2 by partially oxidizing (combusting) them with oxygen. No catalyst is required and the process is more tolerant to sulfur than the other two reforming techniques. However, H_2/CO ratio here is low, while the process works at high temperatures with some soot formation. For methanol reaction:

$$CH_3OH + \frac{1}{2}O_2 \rightarrow CO_2 + 2H_2 \quad \Delta H = -193.2\ \text{kJ/mol} \qquad (1.2)$$

c. Autothermal reforming is a thermally neutral process, as it combines partial oxidation by oxygen to provide the heat and steam reforming to increase the H_2 level. However, it has a limited commercial experience and for methanol it can be expressed by the following reaction:

$$4CH_3OH + 3H_2O + \frac{1}{2}O_2 \rightarrow 4CO_2 + 11H_2 \qquad \Delta H = 0 \qquad (1.3)$$

Since all three processes produce large amounts of carbon dioxide and carbon monoxide (in natural gas processing), high (>350 °C) and low (210–330 °C) temperature reactors are needed to convert CO to a lower level. In addition, with the exception of methanol, most hydrocarbon fuels such as propane, gasoline or logistic

fuels, contain some amount of sulfur and therefore desulfurization is required to avoid catalysts poisoning. Compared to others, steam reforming of methane is at present the most common method to produce H_2 from fossil fuels. The process is low cost, between 1 and 3 euros per kilogram of hydrogen including the cost of CO_2 sequestration, and has an efficiency from 70% to 80% [11, 12].

In gasification, coal is partially oxidized with steam and O_2 in a high-temperature and high-pressure reactor. H_2, CO and CO_2 are the main products that can be processed and cleaned if needed. Despite the fact that the unit cost of coal is lower, natural gas steam reforming is a more economical process than coal gasification [4].

2) Hydrogen from biomass. Biomass is the most likely renewable organic substitute to petroleum. Usually, two types of biomass feedstocks are considered [10, 13]: dedicated bioenergy crops and less expensive regular agricultural farming and wood processing residues. Typically, the methods for H_2 production from biomass can be divided into two categories: the thermochemical route (such as pyrolysis, gasification, steam reforming, supercritical fluid or water extraction, etc.) and the biological route (such as water biophotolysis by green algae and blue-green algae (cyanobacteria), photo-fermentation, dark-fermentation and hybrid reactor system) [14].

The advantages of the thermochemical processes are their higher overall efficiency (thermal to hydrogen) and lower production cost. However, the major disadvantage is the decomposition of the feedstock leading to char and tar formation [14]. Even though biomass gasification and pyrolysis are, probably, the most popular thermo-techniques, it is not generally considered as economically competitive with steam methane reforming: the price is about three times higher for biomass gasification than methane reforming. Generally, at temperatures of about 875–1275 K solid biomass undergoes thermal decomposition and the gasification process can be expressed as follows [14]:

$$\begin{gathered}\text{Biomass} + O_2(\text{or } H_2O) \rightarrow \\ CO, CO_2, H_2O, H_2, CH_4 + \text{other CHs} + \text{tar} + \text{char} + \text{ash}\end{gathered} \tag{1.4}$$

Biological hydrogen production processes are found to be more environment-friendly and less energy intensive. There are three types of microorganisms for so-called biohydrogen generation: cyano-bacteria (algae), anaerobic bacteria and fermentative bacteria. Light-sensitive microalgae are used as biological converters in a specially designed photobioreactor. The process is called biophotolysis, and is based on the algae‘s photosynthesis capabilities to generate oxygen and hydrogen ions at a standard temperature and pressure. However, the process is not fully developed for commercial use and suffers from low conversion efficiencies. Additionally, it requires H_2-O_2 separation and large surface area decisions [15]. The general reactions of H_2 production with the help of photo-activated enzymes are [4]:

$$6H_2O + 6CO_2 \xrightarrow{h\nu} C_6H_{12}O_6 + 6O_2 \tag{1.5}$$

$$C_6H_{12}O_6 + 6H_2O \xrightarrow{h\nu} 6CO_2 + 12H_2 \tag{1.6}$$

A promising method is the biological production of hydrogen by fermentation using pure sugars, such as glucose and lactose, and feedstocks, which are obtained as byproducts from agricultural and the food industry, municipal waste or wastewaters.

Typically, the gas produced is a mixture of hydrogen, carbon dioxide, methane, carbon monoxide and some hydrogen sulfide [16]. A combination of dark and photo-fermentation methods can improve the overall yield of H_2 [14].

3) Hydrogen from water. Water is widely agreed to be the most interesting renewable source for sustainable hydrogen of the future. In this case, electrolysis, thermolysis and photoelectrolysis are considered to be the most promising techniques for water splitting [10].

In general, *water electrolysis* uses an external electrical current as a driving force. Alkaline, polymer-electrolyte membrane (PEM) and solid oxide electrolyzers (SOE) are three key technologies for electrochemical hydrogen production via electrolysis. The fundamentals of electrolysis are based on the electrochemical water decomposition reaction on cathodes or anodes and will be adequately discussed later in Section 1.2.

The greatest advantage of water electrolysis is that the electrolyzers are capable of producing high purity hydrogen and operate under high-pressure conditions. Only renewable power generation from solar, wind and hydro might be used to produce electricity to drive electrolysis. Finally, on site production possibilities of hydrogen via electrolysis may be less expensive than H_2 shipping in cylinders or tankers when produced, for example, via natural gas reforming [10, 17].

In thermochemical water splitting, also called *thermolysis*, heat alone is used to decompose water into H_2 and O_2. Thermolysis reaction can be simplified as [4, 18]:

$$H_2O \xrightarrow{\text{heat}} H_2 + \frac{1}{2}O_2 \tag{1.7}$$

Water decomposition with direct hydrogen production requires temperatures >2500 ^oC [19], however thermochemical cycles with various intermediate steps are currently used to produce hydrogen at reduced temperatures of about 850–1000 ^oC, but with higher pressures. These processes have several drawbacks related to the recombination of hydrogen and oxygen, along with corrosion and heat exchange problems caused by both high temperatures and the chemicals used. It is believed that overall efficiences of about 50% can be achieved during thermolysis; however, it is still not competitive with other H_2 production techniques [10].

Photoelectrolysis is still a developing technique that has only been tested at a laboratory scale. It is one of the most expensive hydrogen production methods. Photoelectrolysis uses sunlight to directly split water molecule into H_2 and O_2 on semiconductor materials. The energy carried by the photon is proportional to the frequency of the radiation and is given by hν, where h is the Plank constant and ν is the frequency. Similarly to water electrolysis, photoelectrolysis can be expressed via oxidation/reductions reactions [4, 20]:

$$\text{Photo-reduction:} \quad 2H_2O + 2e^- \xrightarrow{h\nu} H_2 + 2OH^- \tag{1.8}$$

$$\text{Photo-oxidation:} \quad 2H_2O \xrightarrow{h\nu} O_2 + 4H^+ + 4e^- \tag{1.9}$$

Devices for photoelectrolysis operation are photoelectrochemical cells (PEC), where solar light is absorbed by one or both of the photoelectrodes with at least one of them as a semiconductor. The biggest advantage of PECs is that they do not require a separate power generator such as a PV cell. The hydrogen production efficiency here

is directly related to the semiconductor band gap. The most promising materials so far is agreed to be TiO_2, ZnO, Fe_2O_3, WO_3 and some other oxides. The target efficiency is >16% from solar to hydrogen [10].

Acar and Dincer [4] reviewed, evaluated and comparatively assessed the environmental, financial and technical performance of nineteen selected hydrogen production methods. They were cathegorized by primary energy and material sources. Electrical, thermal, photonic, biochemical, electro-thermal, photo-electric and photo-biochemical types of energy were considered to be potential primary sources to drive various H_2 production methods. Several criteria of parameters, adapted from various reported studies, were selected in order to adequately compare H_2 production methods. The environmental impact was evaluated by *global warming potential* (GWP) and *acidification potential* (AP) according to the life cycle assessment standartized procedures. In this case, GWP is the measure of CO_2 emmisions (g CO_2/ kg H_2), AP indicates SO_2 discharge on soil and into water and measures the change in the degree of acidity (g SO_2/ kg H_2) [21]. The economical impact for each method was assessed by the obtained data of hydrogen *production cost* (\$ / kg H_2). Technological impact was evaluated by means of *energy* and *exergy efficiencies*. The overall comparison of parameters was implemented by normalizing them and ranking between 0 and 10, where 0 means poor performance and 10 indicates the ideal case. Higher rankings mean higher efficiency, lower cost and lower emissions. The hypothetical ideal case was created for zero-cost, zero emmisions, 100% efficiency and ranked by 10. The normalized parameters for various H_2 production methods are adapted from Acar and Dincer work [4] and presented in Table 1.1.

As can be seen in Table 1.1, fossil fuel sourced methods are potentially the most environmentally harmful ways to produce H_2. On the contrary, photonic energy based production is more environmentally benign. However, photo methods are found to be the least attractive when production costs and efficiencies are considered. Electrical based hydrogen production shows the combination of the highest energy efficiency and lowest production cost. In terms of energy and exergy efficiency, the closest performance to the ideal case is reached by fossil fuel reforming and biomass gasification. However, biomass gasification gives considerably high acidification potential over other methods.

Table 1.1. Normalized comparative assessment of various hydrogen production methods based on primary energy sources (Modified from Ref. [4])

Hydrogen Production Method	Energy efficiency	Exergy efficiency	Production Cost	GWP	AP
Electrical energy based	**6.15**	**2.85**	**8.26**	**2.08**	**7.00**
Electrolysis	5.30	2.50	7.34	3.33	8.86
Plasma arc decomposition	7.00	3.20	9.18	0.83	5.14
Thermal energy based	**5.04**	**4.06**	**7.69**	**7.08**	**3.94**
Thermolysis	5.00	4.00	6.12	7.50	7.43
Thermochemical water splitting	4.20	3.00	8.06	9.17	9.43
Biomass conversion	5.60	4.50	8.10	6.67	2.00
Biomass gasification	6.50	6.00	8.25	5.83	0.00
Biomass reforming	3.90	2.80	7.93	6.25	0.86
Photonic energy based	**0.71**	**0.32**	**3.23**	**8.89**	**9.05**
PV electrolysis	1.24	0.70	4.50	7.50	7.71
Photocatalysis	0.20	0.10	5.19	9.58	9.71
Photoelectrochemical method	0.70	0.15	0.00	9.58	9.71
Hybrid	**2.13**	**1.87**	**7.08**	**8.73**	**9.41**
Dark fermentation	1.30	1.10	7.52	9.58	9.71
High temperature electrolysis	2.90	2.60	5.54	7.92	8.57
Hybrid thermochemical cycles	5.30	4.80	7.41	9.43	9.02
Coal gasification	6.30	4.60	9.11	0.00	1.31
Fossil fuel reforming	8.30	4.60	9.28	2.50	5.71
Biophotolysis	1.40	1.30	7.27	7.50	9.71
Photofermentation	1.50	1.40	7.61	9.58	9.71
Artificial photosynthesis	0.90	0.80	7.54	9.58	9.71
Photoelectrolysis	0.78	0.34	7.09	8.33	9.71
Ideal (zero-emissions, zero-cost, 100% efficiency)	*10.00*	*10.00*	*10.00*	*10.00*	*10.00*

1.1.3. Hydrogen storage

Hydrogen storage is one of the key challenges in developing hydrogen economy [22]. This challenges researchers and developers to find a lightweight, safe, efficient and reversible storage material with a high hydrogen density. According to the future prospects of hydrogen economy, H_2 should be stored in various ways depending on the application, e.g. mobile or stationary. For this purpose, the storage is desired to operate at temperatures of 0–100 ^oC and pressures of 1–10 bar.

The key difficulty for H_2 to be stored arises from its low critical temperature of -240 ^oC. In this case, the strong repulsion interaction between molecules is responsible for hydrogen being a gas at ambient temperature. At low temperatures hydrogen is a solid with a density of 70.6 kg/m^3 at –262 ^oC, at higher temperatures it is a gas with a

density of 0.089 kg/m^3 at 0 °C and 1 bar. At a small range of temperatures around – 253 °C, where hydrogen has a density of 70.8 kg/m^3, it is in a liquid phase [23]. Therefore, H_2 storage basically implies the reduction of the enormous volume of hydrogen gas; 1 kg of hydrogen at ambient temperature and atmospheric preasure requires a volume of 11 m^3. Most of the hydrogen storage methods are based on three parameters that allow it to increase the density of hydrogen in a storage system: high pressure, low temperature and stabilization of H atoms by interaction with other materials. In addition, the reversability of the hydrogen uptake and release is also important for a H_2 storage system [23]. The basic storage methods and corresponding characteristics are adapted from Zuttel's works [2, 23] and are listed in Table 1.2.

Table 1.2. The basic hydrogen storage methods (Modified from Ref. [2, 23])

Hydrogen Storage	**Gravimetric density (mass %)**	**Volumetric density (kg H_2/m^3)**	***T*** **(°C)***	***p*** **(bar)**	**Highlights**
Gas cylinders	13	< 40	RT	800	Compressed H_2 gas in lightweight composite high-pressure cyclinder; established.
Cryogenic tanks	Size dependent	70.8	–252	1	Liquid H_2; continuous loss of hydrogen in a few % per day at RT.
Physisorption	~ 4	20	–196	100	Fully reversable physisorption of H_2 on materials, e.g. carbon with a very large specific surface area.
Metalhydrides	~ 2	150	RT	1	Absorbtion in metals; H_2 intercalates in host metals; fully reversable at RT.
Complex hydrides	< 18	150	RT	1	Complex compounds ($[AlH_4]^-$, $[BH_4]^-$), adsorption at high pressures, desorption at elevated temperature.
Alkali+H_2O	< 40	> 150	RT	1	Chemical oxidation of reactive metals with water and liberation of hydrogen;

*RT stands for Room Temperature (25 °C), T – temperature, p – pressure

As can be seen, hydrogen can be physically stored as pressurized gas and cryogenic liquid, and material-based stored as a solid fuel (i.e. chemical or physical combination with materials, such as metalhydrides, complex hydrides, and carbon materials) [22, 24]. Each of these options possesses attractive attributes and main incompatibilities for hydrogen storage specifics. For instance, if hydrogen will be used for mobile applications, the method with the largest as possible values for the gravimetric and volumetric densities is required. The parameter of gravimetric density describes the ratio of the mass of hydrogen to the mass of the storage material/system. The volumetric hydrogen density is an important parameter as a mass of hydrogen in the volume of material/system.

Physical hydrogen storage. High pressure gaseous hydrogen storage, primarily for its technical simplicity and fast filling-releasing rate, has become the most popular and mature method. Compressed H_2 storage systems have been demonstrated in hundreds of prototyped fuel cell vehicles and are available commercially at low production volumes. Here, hydrogen can be compressed by a standard piston-type mechanical compressor [23]. The gravimetric hydrogen density decreases with efforts to increase the pressure: therefore the thickness of the cylinder walls have to be increased. Contrary, the volumetric storage density increase with the increase of pressure and it is typically sacrificed with the reduction of mass % [2, 23, 25].

Storage vessels are the key equipment for high pressure H_2 storage systems. According to different usage scenarios, vessels can be divided into three types, namely: stationary, vehicular and bulk transportation. The potential risks of high pressured H_2 storage includes vessel explosion, gas leakage, temperature rise in fast filling process, and hydrogen embrittlement [26]. In parallel, relatively low hydrogen density, together with the very high gas pressures in the systems, are important drawbacks of the technically simple and, on a laboratory scale, well-established high-pressure hydrogen storage methods.

As compressed gas storage principally focuses on the near-term pathway, cold or cryo-compressed hydrogen storage is dedicated to the long-term strategy [27]. When stored in cryogenic tanks at –252 ^{o}C and ambient pressure, hydrogen is in a liquid form [22, 23]. Even though the density of hydrogen is increased and pressure vessels are insulated, there are large challenges for liquid H_2 storage. In general, the energy-efficient liquefaction process and the thermal insulation of the cryogenic storage vessel to reduce the boil-off of hydrogen are the key issues. For instance, specific and expensive storage vessels (large sized spherical containers) are preferred for a minimal evaporation rate. In this case, boil-off losses can reach 0.4% per day in a 50 m^3 storage vessel [23]. Despite the serious limitations of liquid hydrogen storage, these systems are preferred to be utilized where the cost is not an important issue, where H_2 needs to be stored and transported in a large volume over long distances and H_2 fuel is consumed in a relatively short time, e.g. air and space applications [23, 28].

Material-based hydrogen storage. Hydrogen storage materials can be categorized by the nature of their sorption mechanism e.g. physisorption or chemisorption, and the identity of the material.

Hydrogen storage by *physisorption* on materials is based on weak Van der Waals forces between the adsorbate molecules and the adsorbent. The process is completely reversible and fast refueling is possible. However, higher hydrogen storage capacities can be obtained only at low temperatures (typically between –196 ^{o}C and RT [23]). Different classes of materials, such as active charcoal, nanostructured carbon, zeolites, and a metal organic framework have been investigated for solid-state hydrogen storage by physisorption. Among others, carbon nanostructures and the metal organic framework are the most promising systems [22].

Carbon microporous materials, developed with a large specific surface area and high microporosity with a small pore dimensions ($\leq$ 0.7 nm), are known to be ideal for hydrogen storage [29, 30]. Carbon nanostructures basically consist of benzene-like carbon hexagons that are differently arranged in each nanomaterial [22]. In a great

variety of carbon nanostructures (such as activated carbons and other graphitic structures, carbon nanofibers / nanotubes / nanohorns, etc.) activated Carbon I, obtained from the reaction of coke with KOH, is labeled as the best hydrogen adsorbent. It has a specific surface area of 2564 m^2/g, an average pore diameter of 1.18 nm (11.75 Å), and pore volume of 0.75 cm^3/g. However, the amount of hydrogen adsorbed is limited to 0.54 wt. % H_2 at room temperature and 65 bar, and to 4.4 wt. % at saturation and –196 ºC [29].

Metal organic frameworks (MOF) are a relatively new class of microporous materials with a specific surface area between 2500 and 4000 m^2/g. These materials allow the design of a network of groups of metal oxide connected to each other by a rigid structure. They are known to be the lightest crystalline materials with the densities of < 0.21 g/cm^3 [22]. The most famous structure is MOF-5, which is known to operate a maximum uptake of hydrogen of 4.5–5.2 wt. % at –196 ºC and 50 bar. Basically, MOF-5 is a crystalline solid material with a 1.2 nm pores diameter and a structure of a cube, which consists of $\{Zn_4O\}$ clusters at the corners and carboxylate-based ligands as connections to the 3D cubic framework [31, 32].

Hydrogen storage by *chemisorption* is based on the dissociation of hydrogen molecules and subsequent chemical bonding (absorption) of H atoms by integration into the lattice of material (metal, alloy) or by formation of a new chemical compound [22]. Different metal-hydride systems, complex hydrides, alanates and intermetallic compounds can be formed. Among others, Mg-based metal hydrides and complex hydrides are probably the most promising systems.

Metal hydrides have higher hydrogen-storage density (6.5 H atoms/cm^3 for MgH_2) than hydrogen gas (0.99 H atoms/cm^3) or liquid hydrogen (4.2 H atoms/cm^3) [24]. This primarily makes metal hydride storage a safe, volume-efficient storage method for on-board vehicle applications.

Complex hydrides are known as “one-pass” hydrogen-storage systems, which mean that H_2 evolves upon contact with water [24]. Here, transition of metals to an ionic or covalent compound occurs upon hydrogen absorption. Intense interest has developed in low weight complex hydrides such as alanates $[AlH_4]^-$ and borohydrides $[BH_4]^-$. However, they are known to be stable and decompose only at elevated temperatures, often above melting point of complex [23, 33].

1.2. Fundamentals of hydrogen production by electrolysis

1.2.1. Principles of the electrolysis cell

In the electrolytic cell, two electrodes, with a current flow between them, have to be separated with a membrane or diaphragm to avoid the recombination of the hydrogen and oxygen generated at the cathode and anode, respectively. Depending on the kind of electrolyte, and thus the type of ionic agent (OH^-, H^+, O^{2-}), and the operation temperature, water electrolyzers are classified into three main categories: alkaline, polymer-electrolyte membrane (PEM) and, a latest system, solid oxide electrolyzer (SOE) (Fig. 1.2) [34]. The principles of the water splitting path at anode and cathode are presented according to electrolysis techniques. However, the overall electrolysis reaction is as follows [10]:

$$H_2O \rightarrow H_2 + \frac{1}{2}O_2 \quad \Delta H = -288\ \text{kJ/mol} \tag{1.10}$$

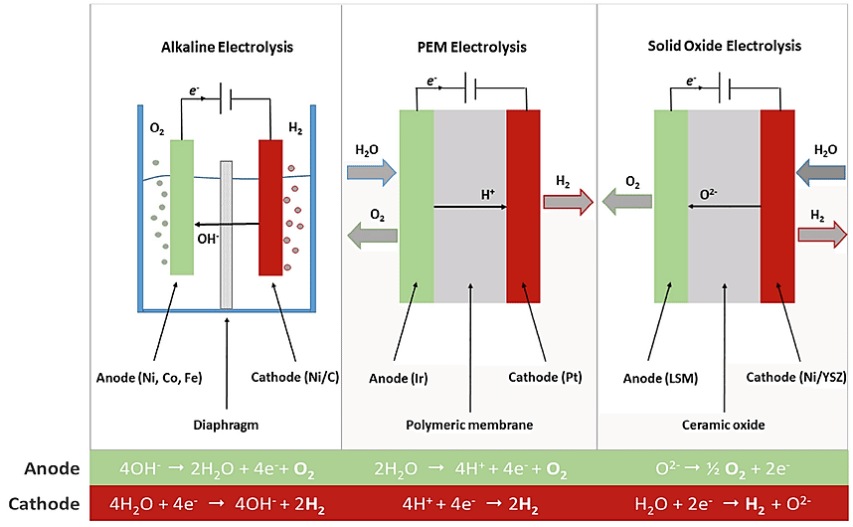

Fig. 1.2. Operation principles of alkaline, polymer–electrolyte membrane and solid oxide water electrolyzers (Modified from Ref. [34])

The most common electrolysis method operates in an alkaline electrolyzer. It is typically composed of electrodes immersed in an aqueous alkaline electrolyte of about 30 wt % KOH or NaOH and separated with a microporous diaphragm, permeable for OH^- only [9, 35]. H_2O in the cell is decomposed into H_2 and OH^- by cathode. Then OH^- travels through the electrolyte to the anode for O_2 formation. The hydrogen left in the alkaline solution is then separated from the water in a gas-liquid separator unit that is outside of the electrolyzer [13]. Even though these alkaline systems are the lowest in capital cost, they also have the lowest efficiency of 50–60 % for 100–300 mA/cm^2 currents. In this case, solid polymer–electrolyte (proton exchange) membrane electrolyzers are the second option for water splitting via electrolysis. PEM electrolyzers are more efficient (55–70 % with currents > 1600 mA/cm^2) than alkaline systems. A nafion membrane is used to separate electrodes and act as a gas separator. Water in this system is introduced at the anode and split into H^+ and O_2. Protons then travel through the membrane to the cathode, where they are recombined into H_2 [13]. O_2 gas remains behind with the unreacted water. While alkaline and PEM electrolyzers operate at the low temperature range (typically below 100 °C), the SOE cell operates at temperatures up to 1000 °C, with water in the form of steam [34]. It works similar to the alkaline system in that an oxygen ion O^{2-} travels through the solid electrolyte, leaving the hydrogen in an unreacted steam stream [13]. The conventional solid electrolyte is ZrO_2 doped with Y_2O_3 (yttria-stabilized zirconia), which possesses great conductivity and stability [36]. The use of a solid electrolyte in the SOE device is advantageous to KOH for alkaline systems, as it is a non-corrosive agent and does not experience liquid / flow distribution problems. Also, high temperature electrolysis decreases overpotentials with the increase in efficiency [10, 34]. However, the high

temperature operation is also the source of degradation and a lack of the electrodes stability, which have to be solved in parallel with safety issues of improper sealing before solid oxide electrolysis can be commercialized on a large scale [34].

1.2.2. Processes in the electrolysis cell

The processes in the electrolysis cell can be described according to electrochemical and thermodynamic principles [11].

Electrochemically, water splitting is best viewed as the combination of a cathodic hydrogen evolution reaction (HER) and anodic oxygen evolution reaction (OER). Characteristic *I – E* curve (Fig. 1.3 a) typically represents the electrochemical behaviour of the electrolytic cell. According to Nernst's equation and well-defined Pourbaix diagram for water under standard temperature and pressure conditions (25 ^{o}C, 1 atm), the Nernst potential referenced to a normal hydrogen electrode (NHE) decreases linearly by 59 mV for each pH unit increase. The standard potential of overall the electrolysis cell (i.e. theoretical decomposition voltage) is based on thermodynamically determined standard reaction potentials ($E^{o}_{cell} = E^{o}_{anode} - E^{o}_{cathode}$). This is calculated to be 1.23 V for pH 0 water electrolysis and theoretically remains unchanged for other pHs. In practical measurements, water decomposition potentials are higly dependent on pH. In this case, a reversible hydrogen electrode (RHE) is often used as a practical hydrogen electrode, whose potential depends on the pH of the solution. For example, using Ag/AgCl as a practical reference electrode, the potentials can be compared in any pH [37]:

$$E_{RHE} = E_{Ag/AgCl} + 0.059 \cdot pH + E^{o}_{Ag/AgCl} \quad (1.11)$$

where $E_{Ag/AgCl}$ is a working potential, $E^{o}_{Ag/AgCl}$ = 0.197 V at 25 ^{o}C.

According to the fundamentals of thermodynamics, the overall energy required for the water electrolysis reaction is determined by the enthalpy change (ΔH). One part of this energy is electric energy and corresponds to Gibbs' free energy change (ΔG). Another part is thermal energy related to the entropy change and process temperature (Q = T·ΔS). The relation can be simply expressed by the following equation [11]:

$$\Delta G = \Delta H - Q = \Delta H - T \cdot \Delta S \quad (1.12)$$

Typically, water electrolysis is an endothermic (ΔH > 0) and nonspontaneous (ΔG < 0) reaction, in contrast to exothermic (ΔH < 0) and spontaneous (ΔG > 0) processes in fuel cells [11]. The energy consumption of the electrolysis highly depends on temperature. It can be observed from Figure 1.3b that electric energy ΔG consumption is significantly lower at high temperatures for both, liquid and gaseous electrolysis. However, a sufficient heat source is required in order to cover the thermal demand T·ΔS. With the increased temperature in a liquid state, the total energy consumption ΔH decreases slightly, while in the gaseous state it increases a little.

Therefore, theoretical energy concumption for 1 m^3 H_2 production is calculated to be 2.94 kWh/m^3 H_2 for ideal water decomposition voltage 1.23 V. However, practical cell voltages in industrial cells are about 1.8 – 2.6 V. In this case, if the cell voltage is 2.0 V, practical energy consumption is 4.78 kWh/m^3 H_2 with energy efficiency of water electrolysis for H_2 production being 61.5% ((2.94/4.76) · 100%) instead of 100% [38].

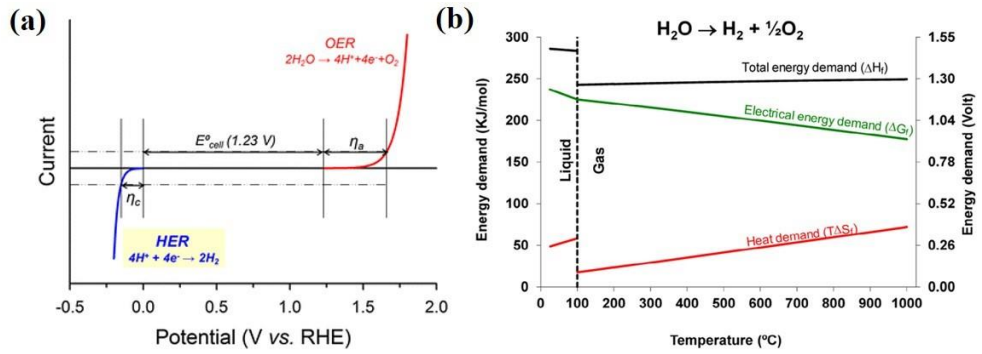

Fig. 1.3. Characteristic *I* – *V* curve (a) and thermodynamics (b) for water electrolysis at atmospheric pressure (Adapted from References a – [39], b – [34])

Practical water electrolysis requires to apply higher potentials than is expected in the *I* – *V* curve simulated for the ideal electrolysis process (Fig. 1.3 a). Sluggish kinetics and poor energy efficiency are linked to some unfavorable factors of electrode materials, such as activation energy, ion and gas diffusion, and some factors related to the cell device, such as solution concentration, wire and electrodes resistances, electrolyte diffusion blockage, bubble formation and heat release [37, 40]. These factors result in additional potential over the standard one, which is called overpotential (η). Taking this into consideration, the applied potential for HER can be expressed as the sum of the theoretical decomposition voltage (E^0_{HER}), reaction overpotential (η) and ohmic voltage drop (iR):

$$E = E^0_{HER} + iR + \eta \quad (1.13)$$

From the practical point of view, the overpotential η is the most remarkable characteristic to compare and evaluate the performances of electrodes and electrolyzers.

The iR in the equation (1.13) is the other important electrochemical characteristic named Ohmic potential drop (or overpotential caused by the ohmic losses) [2, 37]. iR is typically caused by the resistance (R) to current density (i) of cell elements and can be expressed as the sum of resistances [38]:

$$iR = R_e + R_b + R_m + R_c \quad (1.14)$$

where R_e, R_b, R_m, R_c are electrolyte, bubble, membrane and circuit resistances, respectively. R_e is related to the solution composition and electrode distance. R_e increases with an increase of conductive salts, such as KOH, NaOH, $NaClO_4$, etc. For instance, there is about 20% – 30% of NaOH or KOH in alkaline electrolyte. Further addition of salt would result in the corrosion of the cell and destruction of the membrane. The conductivity of electrolyte can also be reduced with the dispersion of gas bubbles in the electrolyte. In addition, bubbles are identified to cause bubble resistance R_b, acting as a shield cover of bubbles on the electrode surface. R_m and R_c are constants for the particular electrolytic cell and typically should be minimized by optimization of the membrane use and wire connections [38].

Consequently, the technologies for process enhancement of water electrolysis must be focused on the reduction of E^0, iR and η. As most studies are focused on

electrode materials, several process intensification technologies have been disscused recently [38]. One of the most interesting intensification effects were related to external forces and bubble effect [38].

During water electrolysis, bubble coverage on the electrode surface and bubble dispersion in the electrolyte, named as bubble effect, result in a high ohmic drop, large reaction overpotential and therefore high energy consumption. In practical electrolysis cases, it is favourable for nonconducting bubbles to appear in minimal volumes and be removed from the cell rapidly. However, bubbles coverage increases with current density and temperature, it disturbs current distribution, isolates active sites and even induces microconvection to push away electrolyte in a radial direction [38]. Additionally, the detached bubbles reduce the conductivity of the electrolyte. The combined negative bubble effect can be minimized by applying external magnetic, ultrasonic or super gravity fields to the working cell [41-43]. External forces promote the disengagement of gas bubbles from both the electrode surface and the volume of electrolyte, whilst even minimising the volume of bubbles.

1.2.3. Mechanistic insight into the HER

The hydrogen evolution reaction is conventionally described by the sequence of three elementary steps: Volmer (electrochemical hydrogen ion adsorption – proton discharge), Heyrovsky (electrochemical desorption) and Tafel (chemical desorption – proton recombination) [44, 45]. These steps fundamentally indicate the hydrogen conversion path from H^+ to H_2 during HER. Originally, the trio of Volmer-Heyrovsky-Tafel elementary steps were identified for hydrogen evolution in acidic media on Pt. Practically, however, HER is known to be initiated within the Volmer adsorption step, but the subsequent hydrogen desorption step may proceed via two possible pathways. In this point of view, HER is frequently based on either the Volmer-Heyrovsky or Volmer-Tafel adsorption-desorption mechanisms. Datta and colleagues [46] studied and portrayed the kinetics of HOR/HER (i.e. hydrogen oxidation/evolution reactions) over a broad range of potentials, including their asymmetric potential dependence. Simulated possible mechanisms in terms of elementary steps are presented in Figure 1.4. This grafical data is very close to the typical Tafel plot (η = f (log j)) obtained from the experimental polarization curve. The corresponding HER mechanism steps can be expressed as follows [37]:

(1) combination of a proton and an electron on a catalyst surface site A which results in an adsorbed hydrogen atom AH_{ads}:

$$A + H^+ + e^- \rightarrow AH_{ads} \quad \text{[Volmer reaction]} \quad (1.15)$$

(2) the adsorbed hydrogen atom combines with a proton and an electron to produce a hydrogen molecule:

$$AH_{ads} + H^+ + e^- \rightarrow H_2 + A \quad \text{[Heyrovsky reaction]} \quad (1.16)$$

(3) coupling of two adsorbed hydrogen atoms to produce a hydrogen molecule:

$$AH_{ads} + AH_{ads} \rightarrow H_2 + 2A \quad \text{[Tafel reaction]} \quad (1.17)$$

The mechanism of HER can be discussed in terms of kinetics and the Tafel plot. Primarily, if hydrogen binds to the surface too weakly, the adsorption (Volmer) step will limit the overall reaction rate, whereas if the binding is too strong, the desorption (Heyrovski/Tafel) step will be rate limiting [47]. Reaction rate and its limiting step

can be experimentally determined by the values of the Tafel slope. The modern Tafel equation is used to evaluate the relationship between overpotential η and current density j:

$$\eta = a + b \cdot \log(j) \quad (1.18)$$

where both a and b are Tafel constants, η and i are variables.

Constant a represents the overpotential at 1 A/cm^2 and is related to characteristic properties and surface structure of the electrode material. According to the value of a, metal materials as cathodes for HER are divided into three categories [38]:

(a) Metals with high overpotential: Cd, Ti, Hg Pb, Zn, Sn, etc;

(b) Metals with middle overpotential: Fe, Co, Ni, Cu, Au, Ag, W, etc;

(c) Metals with low overpotential: Pt, Pd;

Constant b is a Tafel slope. From the equation (1.18) it is evident that overpotential η and log(i) should exhibit linear dependence. In this case, constant b corresponds to the slopes of a linear regions within the Tafel plot. The value of b gives information on the rate determining step in an electrochemical reaction. As a benchmark for the HER, platinum in acidic solutions operates under three reaction steps with rate determining Tafel slope values: 120 mV for the Volmer step, 40 mV for the Heyrovsky step and 30 mV for the Tafel step [44, 45, 48]. However, the interpretation and simulation of these values are sometimes controversial.

In particular, two scenarios can be detected based on the aforementioned elementary steps [45]: (a) H^+ adsorption rate determining step and (b) H_{ads} desorption rate determining steps. In the case where the H_{ads} desorption steps (Heyrovsky or Tafel) are rate determining, the surface coverage of H_{ads} may be significantly high. The Tafel slopes for rate determining Heyrovsky and Tafel desorption steps have b values of 40 mV and 30 mV, respectively. The experimental measurements show that these values can be detected only at the very beginning of HER. The interpretation of b∼40mV and b∼30mV are usually uncertain and disputed. It should also be noted, that these values were calculated to be minimal limits of b values for each of the desorption steps [45]. In the case where the H^+ adsorption (Volmer) step is slower than the other steps, the concentration of H_{ads} can be considered to be negligibly small, as a result of its consumption in the faster succeeding steps. This scenario corresponds to a calculated Tafel slope of ∼120 mV and has a reaction order of 1 [45]. In other words, the slope of ≥120 mV typically indicates the domination of „other than H adsorption processes“.

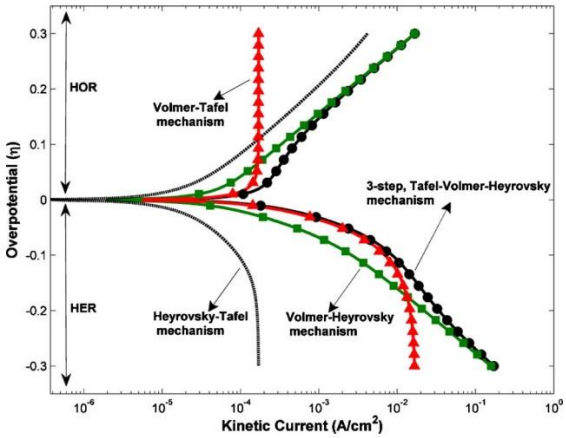

Fig. 1.4. Three-step and two-step HER mechanisms in semilog plot of overpotential vs absolute value of kinetic current [46]

Practically, a small value for the Tafel slope is expected; as this is a property of a good electrocatalyst [49]: a smaller Tafel slope means a slower increase in overpotential with increasing current density. In other words, it is an indication of high H adsorption and HER initiation ability under low overpotentials. It should be mentioned that the Tafel slope should be determined and evaluated in particular limits of, for example, selected overpotential range or decade of current density. For instance, it can be seen in Figure 1.4 that mechanisms are individually applicable only in limited potential ranges [46].

1.2.4. Electrocatalysts for the HER

For over 50 years, it has been well established that if the exchange current density of the HER is plotted against some experimental measure (descriptor) of the metal–hydrogen bond energy, a volcano-shaped curve is obtained. Recently, Norskov and co-workers used a density functional theory and calculated the Gibbs free energy for hydrogen adsorption on metals (ΔG_H) and proposed it to be a good descriptor of the intrinsic activity of a metal for HER [50-52]. In general, the volcano plot reflects the so-called Sabatier principle. Pt group metals are at the summit of the volcano, having the highest activity and close to zero hydrogen adsorption energy (Fig. 1.5). Metals to the left of Pt bind hydrogen atoms too strongly, blocking the active site and failing to evolve hydrogen. On the other hand, metals to the right of Pt binds hydrogen too weakly, failing to stabilize the intermediate state and preventing any reaction from taking place. Thus, an ideal electrocatalysts for the HER should have well-balanced hydrogen bonding and releasing properties with ΔG_H close to zero [40, 53]. ΔG_H is a useful descriptor in the selection, representation and comparison of new electrocatalysts (not only pure metals, but also alloys and transition metal compounds) for hydrogen evolution. Understanding how to control binding energies of reactive intermediates on a surface is a key to designing materials with improved HER performance.

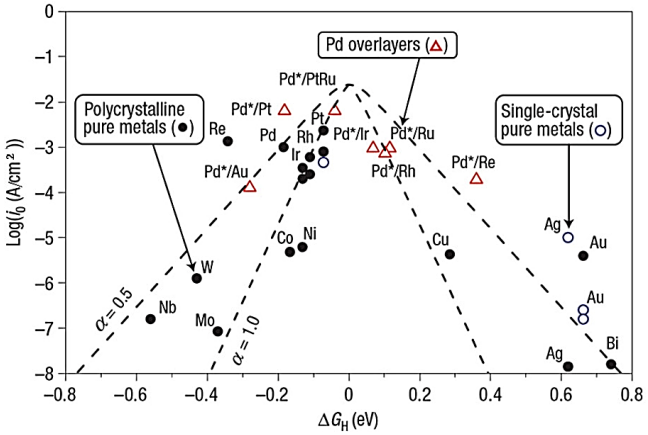

Fig. 1.5. Volcano plot for the Hydrogen Evolution Reaction for various pure metals and metal overlayers (denoted as metal*/substrate) [50]

The activity of the HER catalyst is collectively influenced by many other factors, such as conductivity, crystallinity, roughness and catalyst supports. In general, there are two strategies to improve the activity of an electrocatalyst system: (a) increasing the number of active sites on a given electrode (e.g. through increased loading or improved catalyst structuring to expose more active sites per gram) or (b) increasing the intrinsic activity (turnover frequency) of each active site [47, 54]. These strategies are presented in Figure 1.6 and are illustrated via structural and compositional catalysts engineering solutions.

Nanostructured electrocatalysts for the HER in a variety of forms (such as nanoparticles, thin films, nanowires, 3D gyroid structures, etc.) and dimensions have been made with greatly improved electrochemical performance compared to their bulk counterparts [40]. Dispersion of nanoparticles on supports with a high surface area (for example, carbon black, graphite papers, reduced graphene oxide (RGO) nanosheets) and different regular or amorphous shapes of, for instance, cubic, spherical, octahedral morphologies can also result in an increased number of accessible active sites per geometric electrode area [54, 55].

However, there are physical limits to how much catalyst material can be loaded onto an electrode without starting to limit charge and mass transport. Thus, a plateau effect can be observed in practice at high catalyst loadings (Fig. 1.6). In these cases, increasing intrinsic activity of each active site can lead to reduced transport issues and decreased catalyst loading with savings on catalyst cost [54]. Novel approaches in improving the intrinsic activity of MoS_2 are identified as activating the S-edge by doping (i.e. adding small amounts of transition metal dopants including Co and Ni), modifying the H-binding energy through substrate interactions, tuning electronic properties through Li^+ ion intercalation into the van der Waals gaps, and utilizing the conductive 1T polymorph of MoS_2 [54].

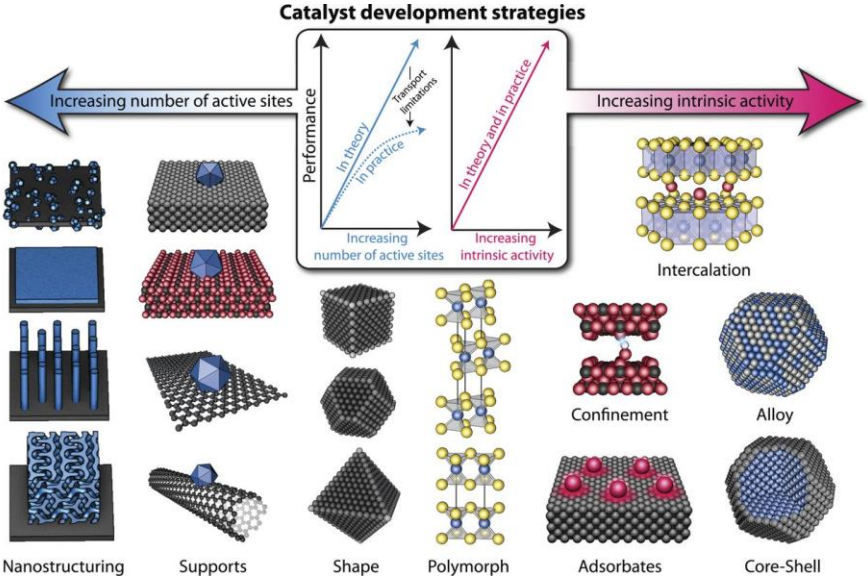

Fig. 1.6. Schematic of various electrocatalyst development strategies based on increasing the number of active sites and/or intrinsic activity of each active site [47]

As can be seen in the Volcano plot (Fig. 1.5), the noble platinum group metals (Pt, Ru, Rh, Ir and Pd) are the best known HER electrocatalysts in terms of overpotentials. Among them, Pt is the most efficient and stable cathode to catalyse HER in acidic or alkaline electrolytes and is frequently used to benchmark the activity of other HER electrocatalysts. However, the practical developments require cheaper and earth-abundant electrocatalysts. Three major strategies are still under consideration for more reasonable Pt utilization: (a) fabrication of Pt nanostructures with a surface architecture of an increased number of reactive sites, i.e. more porous [110] surfaces; (b) depositing a monolayer of Pt on low-cost alternative materials (for instance, metal carbides) to obtain Pt-like catalysts with a reduced amount of Pt loading (c) alloying with other metals to increase the site-specific activity [37, 56]. It is probably impossible to provide a comprehensive list of all reports dedicated for non-noble metals based HER electrocatalyst. Although, three categories of HER electrocatalytic materials are under intense investigations: (i) alloys, (ii) transition metal compounds, and (iii) metal free carbonaceous nanomaterials [57], the HER activities of these electrocatalysts were compared in terms of overpotential needed to reach 10 mA/cm^2 in acidic or alkaline electrolytes and reported by Li *et al.* [40] (Fig. 1.7).

Due to the lowest overpotentials, metallic alloys are a potential electrocatalysts for HER in alkaline media, where many other materials fail to perform. According to the theory of the Volcano plot, only noble metals have a fortune to efficiently electrocatalyze the HER. Thus, the option to employ inexpensive metals was to alloy metals with weaker and stronger M–H bonds [57]. Ni-based alloys (*e.g.* Ni–Mo, Ni–Al) are probably the most efficient HER electrocatalysts in alkaline electrolytes. However Ni usually suffers from

insufficient electrocatalytic activity and more importantly, progressive deactivation toward the HER upon continuous alkaline electrolysis due to the reversible formation of nickel hydride species [58]. In addition, nonprecious metal alloys are not suited for the HER in acids due to their rapid corrosion [40].

The second category of interest is a group of transition metal compounds TMX (where TM is Mo, W, Ni, Co, etc. and X is S, Se, P, C, B, N, etc). Majority of them are semiconductors and suffer from low electrical conductivities [57]. Transition metal chalcogenides, carbides, nitrides, borides and phosphides are all prone to gradual oxidation when exposed to air or aerated solution, forming inert surface oxide layers. This is even more severe in an alkaline media [40]. From this point of view, a few successful TM oxides / hydroxides performances were also reviewed [59, 60]. However, transition metal compounds possess the most practical activity and stability options to operate in HER.

In spite of a relatively short history (~5 years) of intense research on metal phosphides, they are leaders in activity for the HER in acids [61]. Phosphides of Ni, Co, Fe, Mo, W and others demonstrate low overpotentials and even some metallic properties. TM phosphides reactivity is related to the charged P sites, but a passive layer can be easily formed on the surface and block the electrocatalytic reaction [57]. MoB, as representative of the borides group, was found to operate in HER at both 1 M H_2SO_4 and 1 M KOH electrolysis baths, however it became corroded after just one hour in the base solution [62]. It is widely accepted, that transition metal carbides often exhibit Pt-like electrocatalytic activity, particularly tungsten or molybdenum carbides (WC, Mo_2C) [63, 64]. They are not as vulnerable as Pt to poisoning and deactivation. However, oxygen species can block these HER electrocatalysts and interaction with water passivates the WC surface via the WO_3 layer [57]. Therefore, TM carbides are not practical candidates as stand-alone electrocatalysts and are more attractive as low-cost substrates for Pt. Even though transition metal nitrides operate under relatively high overpotentials, they can be employed in an alkaline media without stability issues: at least 32 h of operating was recently recorded for nickel nitride [65]. Eventually, since MoS_2 was broadly reported as a promising HER electrocatalyst [66, 67], the family of transition metal chalcogenides became the candidates of thorough investigations due to the low cost and ease of preparation. However, their structure should be carefully planned for the practical performances of HER. Typically, the class of chalcogenides suffer from limited activity by the number of active sites on edge. In a context of novel ΔG_H-based Volcano plot, sulfided Mo-edges were found to be active for the HER with $\Delta G_H \sim 0.1$ V, very close to the value of Pt as a benchmark [66]. With an impressive amount of studies on MoS_2, $MoSe_2$ materials and their structural architectures, the overpotentials for HER can be found to vary from 100 mV to 300 mV [40]. As amorphous MoS_x is one of the key subjects for investigations in this thesis, more detailed analysis will be presented in the following section.

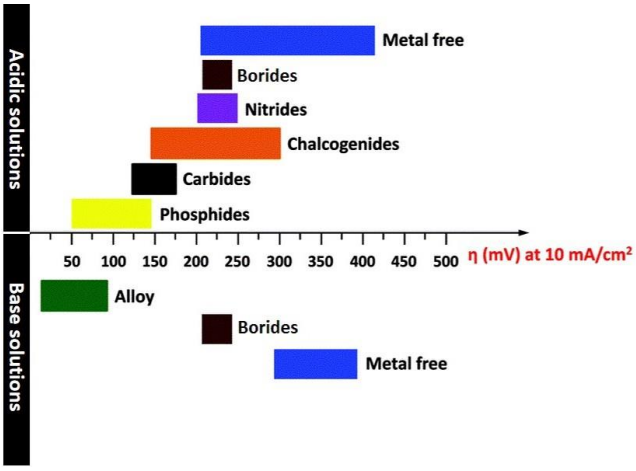

Fig. 1.7. Overpotentials required for different catalytic materials to achieve 10 mA/cm^2 in HER in basic and acidic solutions (Modified from Ref. [40])

Fabricating a metal-free carbon catalyst is still not very practical. Even though materials, such as graphene or graphitic carbon nitride, are advantageous via high electrochemical stability, lightweight and low cost, neither of these carbonaceous materials are suitable for the HER because of too high overpotentials. Hence, because of being electrochemically inert, many carbon-based current collectors such as glassy carbon, carbon paper and carbon cloth are typically used only as supports in electrochemical experiments [40, 57].

For earth-abundant inorganic electrocatalysts to become competitive with those containing noble metals, there are a number of specific challenges that must be overcome (electrocatalytic activity and stability, electrical conductivity and chemical compatibility). Even though they have to be active without strict requirements for long-term stability (they should be easily replaced or regenerated), earth-abundant inorganic electrocatalysts should ensure fast charge transport and low Ohmic losses in order to achieve maximum efficiency. They should also possess high chemical compatibility with their operating environment to compensate the inert nature of Pt [60].

1.3. Electrodeposition of S-containing Co–Mo oxide films

1.3.1. Thiourea as S-source

Thiourea (thiocarbamide) is an organosulfur compound with the formula $(NH_2)_2CS$. Structurally; thiourea is related to urea (carbamide; $(NH_2)_2CO$) with the oxygen atom replaced by an atom of sulfur. Even though thiourea is mainly used in organic synthesis, $(NH_2)_2CS$ is one of the preferred sulfur sources (together with the Na_2S and H_2S) for the synthesis of inorganic metal sulfides. Commonly, thiourea can be employed as a sulfur donor in the chemical or electrochemical synthesis methods to prepare thin films of metal sulfides. While it is difficult to monitor the behaviour of S species in both cases, possible *S donoring mechanisms* are under discussion.

Consideration of the chemistry that implements non-electrochemical solution growth processes may be useful to enhance the understanding of electrochemical

deposition in similar baths. Chemical solution-based synthesis methods include two possible reaction mechanisms. Firstly, the thiourea hydrolysis mediated mechanism was considered in several discussions [68, 69]. Here the formation of free S^{2-} ions from the hydrolysis of thiourea by action of the hydroxide ions proceeds as the first step, and the reaction between the produced S^{2-} and the metal ions M^{2+} as the second step. Typically, this mechanism is attributed to the metal sulfide film deposition from the alkaline solution and/or the substitution reaction between the free sulfide ions and formed metal hydroxide. The reactions involved can be outlined by the following equations [69]:

$$SC(NH_2)_2 + OH^- \rightarrow NCNH_2 + HS^- + H_2O \quad (1.19)$$

$$HS^- + OH^- \leftrightarrow S^{2-} + H_2O \quad (1.20)$$

$$M^{2+} + S^{2-} \rightarrow MS \quad (1.21)$$

$$M(OH)_2 + S^{2-} \rightarrow MS + 2OH^- \quad (1.22)$$

However, the thiourea hydrolysis mechanism was criticized experimentally. It was revealed that $(NH_2)_2CS$ does not desulfurize in aqueous solutions containing only metals salt or hydroxide. These studies concluded that metal sulfides are synthesised via an intermediate complex formation/decomposition mediated mechanism. This mechanism is based on the stable complex formation between $(NH_2)_2CS$ and M^{2+} in aqueous media, transition to metastable intermediate complex after interaction with OH^- ions and the immediate decomposition to the relevant metal sulfide. No sulfur ions are individually released during the whole process and this alternative complex mechanism can be summarized as follows [69]:

$$M^{2+} + (NH_2)_2CS + 2OH^- \leftrightarrow [M(OH)_2((NH_2)_2CS)] \rightarrow \rightarrow MS + H_2NCN + 2H_2O \quad (1.23)$$

From the electrochemical standpoint, thiourea can act differently. Typically, thiourea is used as an additive in electrodeposition for metals or metal sulfides. In addition, TU is often employed as a corrosion inhibitor of metal films in acid media by blocking surface sites through adsorption. It is widely accepted that TU adsorbs on metals and donates/poisons the electrode with sulfur species after oxidation of the TU molecule. The following processes can take place depending on the electrochemical reaction conditions.

The electrochemical behavior of TU in an acidic media on an Au electrode was summarized according to different potential ranges [70] (Fig. 1.8). It was concluded that TU adsorbs on an Au surface in the 0.05–0.40 V_{RHE} potential range. At more positive potentials the electro-oxidation takes place and two parallel oxidation pathways are identified for adsorbed TU: *(1)* the formation of a surface-TU complex and the following multi-step oxidation to $NH_2CN + S^0$ with the N_2, CO_2 and HSO_4^- /SO_4^{2-} produced at the end of the sweep; *(2)* the formation of $(TU)_2^{2+}$ – TU dimmer formamidine disulfide (FD).

Prior to the TU electrochemical behavior on Au, the thiourea response on Pt in acidic media was under thorough investigation [71]. Similarly to the previously described mechanism, two electro-oxidation stages of TU were also observed on Pt. It is interesting to note that these two stages were identified to occur one after the other (i.e. *(2)* before *(1)*), rather than in parallel.

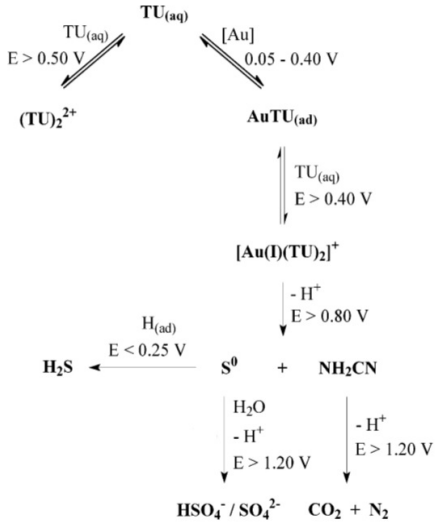

Fig. 1.8. Scheme of the electrochemical behavior of thiourea in an acidic medium on Au electrode [70]

Subsequently, electrochemical reactivity of thiourea on the Au surface was investigated in a non-acidic media where the electrochemical reaction was observed to perform at more negative potentials [72]. The investigations were based on a combination of atomic level images of Scanning Tunneling Microscopy (STM) and a cyclic voltammetry in aqueous (pH 6) TU + $NaClO_4$ solution. Figure 1.9 illustrates the thiourea electrochemical path at potentials E < 0.4 V_{SCE} on an Au electrode and corresponding adsorbates modeled in each potential region. According to the general mechanism proposed by researches [72], thiourea overcomes the path of electro-adsorption/desorption, electro-oxidation/reduction processess overall cyclic electrode polarization and specific peaks were justified for each process.

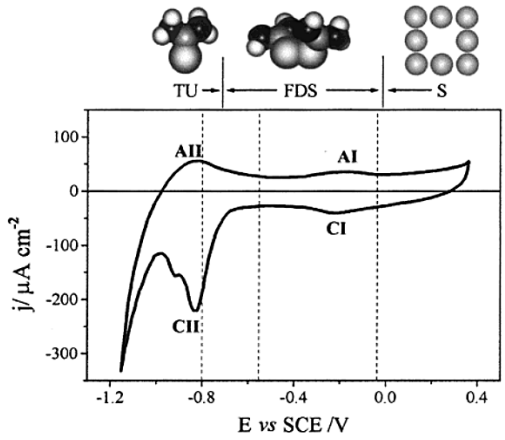

Fig. 1.9. Cyclic voltammogram of Au (111) in 0.05 M $NaClO_4$ + 0.05 M TU run at 100 mV/s (T=298 K). Dynamically preponderant adsorbate in each potential region is drawn schematically above [72]

It is apparent in Fig. 1.9 that two conjugated pairs of broad current peaks at E = –0.20 V_{SCE} (peaks AI/CI) and E = –0.80 V_{SCE} (peaks AII/CII) appeared during Au electrode polarization in aqueous TU solution. For E < –1.10 V_{SCE} the hydrogen-evolution-reaction cathodic current was observed. According to a fairly detailed discussion, the upper sweep started with the voltammetric peak AII, which was identified as perpendicular S-head TU molecules electro-adsorption. A packing effect of the adsorbed TU molecules was noticed by changing E from –0.55 V_{SCE} to –0.05 V_{SCE} and the hydrogen bonding was indicated to play an important role in stabilizing this structure. As closely packed molecules shifted spontaneously into ladder-like, striped array structures, peak AI appeared in the voltammogram. Peak AI then was assigned to the one-electron surface electrooxidation of TU, to its dimmer formamidine disulfide (FD). FD structures left alone can slowly be oxidized to polymeric sulfur and this could be accelerated electrochemically as the anodic current increases at the end of the upper sweep. On the way back of the sweep, two corresponding cathodic peaks CI and CII appeared in the cyclic voltammogram. Accordingly, electro-reduction of sulfur species (such as FD and sulfur) to produce TU could be the origin of peak CI and following peak CII, which could be attributed to the electro-desorption of TU/FD lattice from the electrode [72]. It should be noted that the surface of Au is inert to these reaction conditions and the possibility to adopt sulfur during the whole cycle was not under consideration in this case.

In the context of Au and TU electro-interaction in a non-acidic media, following studies [73] were dedicated to TU electrochemical behavior on the less "sterile" surface of Ag and inevitable formed Ag oxide electrode. It was found that only a slight shift of electro-adsorption/desorption peak potentials to the negative direction occurred as the pH was changed from 6 (in 0.05 M $NaClO_4$) to 13 (0.1 M NaOH) for the Ag electrode. The overall electrochemical path of TU remained similar when the substrates were changed from Au to Ag. A shift of ~0.3 V to the negative direction was noticed, however this effect was justified by the differences in substrates work functions.

Above all, [73] publication paid significant attention to the TU adsorption stage. Generally, adsorption of S-containing molecules on Au or Ag was justified as a model system for the self-assembly (SA) processes (Fig. 1.10). The main feature of SA films is a self-assembled monolayer film that spontaneously forms by chemisorption of molecules from solution. These films have unique properties of ordered orientation, densely packed structure periodicity and, especially, its stability to a chemical environment, heat and external pressure. SA films exhibit good electronic and photonic activities and have applications in molecular electronics, nonlinear optics, photonics, nanofabrication, electrocatalysis, corrosion protection, etc. Adsorption and SA monolayer formation of organosulfur compounds on metals such as gold, silver and copper have shown the greatest promise of controlling the chemical structure of organic surfaces. In aqueous media of an electrochemical bath, intermolecular forces and hydrophobicity of the molecules play key roles in the electro-adsorption/desorption behavior of alkanethiols on the substrate: they bond strongly to these metals by the S-head upon adsorption. Recently, Su and Hatton reviewed electrosorption as electrochemically driven adsorption at charged interfaces for water

purification, chemical separations, biological and environmental processes [74]. Despite the various physico-chemical mechanisms, general principles of electrosorption include fundamentals of electrical double layer formation and electrostatic forces between electrolyte ions and charged interfaces. Electrolyte ions are adsorbed to oppositely charged surfaces while external stimuli (light, pH, magnetical or electrical fields, i.e. negative or positive electrode polarization) can be applied to release (desorb) the attached (adsorbed) fragments [74].

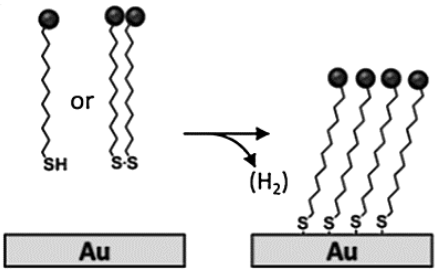

Fig. 1.10. Formation of functional thiol/gold SA monolayer [75]

TU electro-adsorption on metals is known as a complex process, because of TU high chemical reactivity both in the electrolyte and in the adsorbed state. In fact, intermediate products can be adsorbed on the surface. For instance, the most common TU related compounds are listed in Table 1.3 [73]. Thiourea (TU), as a short S- and N-containing molecule with unstable C=S thiocarbonyl bond and, therefore, with exposed SA features, is known to be electro-adsorbed by S-head. In contrast, TU related tetra methyl thiourea (TMTU) presents its adsorption through both S and N. The canonical form of TU is found to be adsorbed on Ag and Cu surfaces, possibly, by a cleaved S–H thiol bond. The following electro-oxidation of these species on the electrode surface leads to the most commonly described TU intermediate formamidine disulfide (FD).

Table 1.3. Chemical formulas for thiourea and related compounds [73]

Molecule	TU (normal)	TMTU	TU (canonical)	FD
Formula	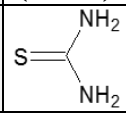	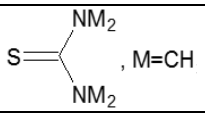	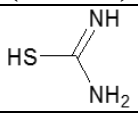	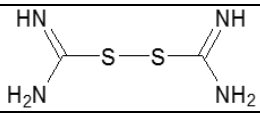

It is modeled that dissociation of these SA oriented organosulfur molecules on metals leave sulfur and carbon atoms on the surface, whereas hydrogen molecules and hydrocarbon species are typically desorbed. Unfortunately, the electro-desorption processes can cause disorder of the preferred SA layers. Prolonged exposure of aqueous S-containing compounds can produce extensive sulfidation of metal surfaces and produce a thin interfacial layer of metal sulfide. It should however be noted that S donoring through electro-adsorption/desorption of SA molecules can be complicated, as the coverage of sulfur can appear 10 times lower than that of oxygen

and carbon [73]. Additionally, the growth of the metal sulfide films was suggested to be limited by the supply of sulfur-containing species, especially in cases where TU is not allowed to adsorb and completely cover the electrode [74].

1.3.2. Co–S films

As semiconductor compounds, cobalt sulfides are important materials due to their unique catalytic, electrical, magnetic properties and potential applications. Cobalt sulfides can exist in several stoichiometric and non-stoichiometric phases, such as Co_4S_3, Co_9S_8, CoS, $Co_{1-x}S$, Co_3S_4, Co_2S_3, and CoS_2 [76, 77]. Stoichiometry of cobalt sulfides is more complicated than that of cobalt oxides, because of the coexistences of strongly reducible cobalt ion and oxidizable sulfide ion. In addition, cobalt ion has a very strong affinity to oxygen. During synthesis, it is difficult to avoid cobalt oxide or cobalt hydroxide impurities in the resultant materials [76, 78].

When compared to other semiconducting transition metal sulfides (such as sulfides of nickel, molybdenum or copper) only a few works have been done on electrodeposition of cobalt sulfides. Recently, Gratzel et al. [79] have proposed a one-step electrochemical deposition method of Co–S in an alkaline cobalt-based deposition bath and employed it as a counter electrode in dye-sensitized solar cells (DSSC). Successful attempts were subsequently reported for several cobalt sulfides as effective electrocatalysts for the HER [68, 80]. Typically, CoS-based catalysts were prepared by electrochemical, electrophoretic (EPD) and ion exchange (IED) depositions techniques, solvothermal, chemical bath and SILAR methods [81-84]. Among others, electrochemical deposition of cobalt sulfide is advantageous, as it is easy to perform, scalable, does not require expensive equipment and can be undertaken under ambient conditions. In addition, it has various freedom parameters (such as deposition potential, time, current density) and adaptable methods in order to coordinate the so important composition, morphology and density of active sites [68].

Table 1.4 lists a brief review and comparison of general reported electrochemical deposition techniques, synthesis conditions and applications of CoS electrodes. As can be seen, a cobalt sulfide electrodeposition bath is usually filled with aqueous solutions of cobalt salt and thiourea, as Co and S precursors, respectively. Deposition baths are neutral or near neutral and a small amount of ammonia can be used in some cases for the adjustment of the pH value. In order to optimize the composition of the synthesis solution and to investigate the influence of precursors, several studies were also dedicated to adjust and test variations of the concentrations of cobalt salt, thiourea and ammonia. Some Co–S films were successfully produced via the potentiostatic deposition method, however, the potentiodynamic technique showed opportunities for more efficient synthesis and became dominant in the majority of the reports. In addition, there are studies dedicated for successful step-by-step preparation of Co–S electrodes via a combination of an electrochemical technique accompanied with chemical deposition. As can be seen, majority of the electrochemically prepared Co–S electrodes were tested as electrocatalysts for iodide / triiodide (I^- /I_3^-) redox reaction in dye-sensitized solar cells. However, several comprehensive studies were dedicated to investigate Co–S catalytic activity in water splitting and opened disscusions for further research in this field.

Table 1.4. The comparison of cobalt sulfide electrodeposition techniques and applications

Electrode	Preparation method	Deposition bath	Application	Ref.
CoS loaded ITO/PEN films	Potentiostatic (-0.8 V, 30 min, 22 °C)	5 mM $CoCl_2 \cdot 6H_2O$ 0.150 M Thiourea (pH=10)	DSSCs	[79]
Highly porous CoS films on FTO	a) Potentiostatic (-0.8 V, 30 min) b) Cyclic voltammetry (up to 10 CVs)	5 mM $CoCl_2 \cdot 6H_2O$ 0.5 M Thiourea ($NH_3 \cdot H_2O$ for pH=6)	DSSCs	[85]
CoS/T-NT composite	a) Potentiostatic (-0.5 V, -1.5 V, 30 min) b) Cyclic voltammetry (10 CVs)	10 mM $CoCl_2 \cdot 6H_2O$ 0.5 M Thiourea	Supercapacitor	[86]
Amorphous CoS_x on RGO or ITO	a) Potentiostatic (-0.72 V, -0.57, 10 min) b) Cyclic voltammetry (up to 15 CVs)	0.005–1.0 M $Co(NO_3)_2$ 0.005–1.0 M Thiourea (pH=2–7)	HER and OER	[68]
Co–S/Ti mesh	Cyclic voltammetry (15 CVs)	5 mM $CoCl_2 \cdot 6H_2O$ 0.75 M Thiourea	OER	[87]
Co–S/FTO	Cyclic voltammetry (15 CVs)	5 mM $CoCl_2 \cdot 6H_2O$ 0.5 M Thiourea	(Photo)-electrochemical HER	[80]
Amorphous CoS_x on FTO	Cyclic voltammetry (up to 50 CVs)	5 mM $CoCl_2 \cdot 6H_2O$ 0.5 M Thiourea (in 0.5 M, pH 7 phosphate buffer)	HER	[88]
Co–S/FTO	Cyclic voltammetry (1, 3, and 5 CVs)	5 mM $CoCl_2 \cdot 6H_2O$ 0.5 M Thiourea ($NH_3 \cdot H_2O$ for pH=7)	DSSCs	[89]
Mesoporous CoS on FTO	Cyclic voltammetry (5 CVs)	5 mM $CoCl_2 \cdot 6H_2O$ 0–1.5 M Thiourea ($NH_3 \cdot H_2O$ for pH=6)	DSSCs	[90]
Co–S/FTO	Cyclic voltammetry (up to 5 CVs)	2 mM $CoCl_2 \cdot 6H_2O$ 0.2 M Thiourea 0–3.0 mL $NH_3 \cdot H_2O$	DSSCs	[91]
Honeycomb-like Co–S/FTO	1. Electrophoretic deposition (3 V for 5sec in 0.1 M $Co(NO_3)_2 \cdot 6H_2O$) → 2. Ion exchange deposition (2 min in 0.05 M Na_2S in methanol) → 3. CE treatment (1 h in $NaBH_4$ and/or 10 sec in H_2SO_4)		DSSCs	[81]
CoS/FTO	1. Potentiostatic deposition (-0.8 V, 5–15 min in 5 mM $CoCl_2 \cdot 6H_2O$) → 2. Ion exchange deposition (2 min, 60 °C in 0.1 M Na_2S)		DSSCs	[92]

1.3.3. Mo–S films

Molybdenum sulfides prepared either as nanoparticles or as films are very attractive noble-metal-free electrocatalysts for the hydrogen evolution reaction (HER) from water. Crystalline molybdenum disulfide (*c*-MoS_2), amorphous molybdenum sulfide (*a*-MoS_x), and molybdenum sulfide molecular clusters have gained attention for their scalable preparation methods, attractive catalytic activities and robustness, especially in harsh H_2-evolving conditions [93]. Various Mo–S film structures can be obtained, as the molybdenum has oxidation states ranging from +2 to +6 and coordination numbers from 0 to 8 [94]. Amorphous molybdenum sulfide is known to exhibit significantly higher HER activity compared to its crystalline counterpart. For *c*-MoS_2 (Fig. 1.11 A), Mo sites are stabilized by disulfide ligands in the edge planes. Particularly, these edge planes are suggested to be responsible for HER activity, whereas basal planes are inactive. In the case of *a*-MoS_2, molecular-based coordination polymer structures were suggested to be composed of discrete $[Mo_3S_{13}]^{2-}$ building blocks (Fig. 1.11 B) with apical S^{2-} and three types of disulfides acting as shared, terminal and bridging ligands within the whole proposed *a*-MoS_2 structure [93]. Typically, amorphous materials are prepared at milder temperatures and with faster solidification processes than crystalline materials. Although amorphous molybdenum sulfides lack long-range order, they contain short-range atomic arrangements that are electrocatalytically active [95].

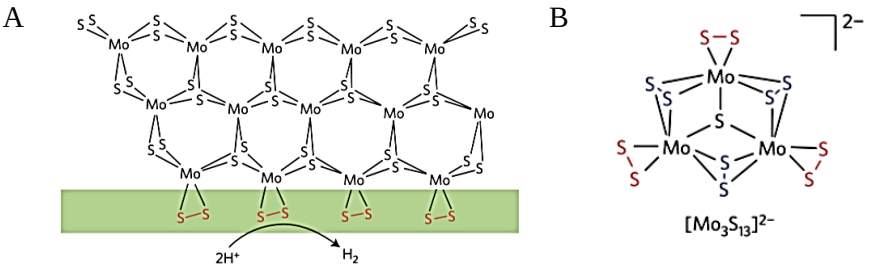

Fig. 1.11. Structures of molybdenum sulfide materials: (A) - crystalline molybdenum disulfide *c*-MoS_2 and (B) - $[Mo_3S_{13}]^{2-}$ cluster in amorphous *a*-MoS_x structure [93]

Molybdenum sulfides have aquired a formula of MoS_x (x ≈ from 2 to 3) while they were applied and operated as a stable HER catalyst in a wide pH range (e.g., 0–13). Compared with many other MoS_2 nanoparticles, amorphous MoS_x catalyst show a higher HER activity, likely due to a higher amount of unsaturated Mo and S sites. MoS_2 semiconductors have been investigated as dry lubricant for high-temperature coatings application, co-catalyst for desulfurization in petrochemistry, and a component for photoelectrochemistry and microelectronics [96].

While usual thin films preparation techniques are cost intensive and operate under harsh conditions (i.e. solvothermal synthesis, sulfidization, etc.), electrodeposition of MoS_2 films became attractive and amenable for large scale applications. Generally, the electrodeposition of Mo–S films can be classified according to the precursors of Mo and S in the deposition bath.

(1) Ammonium tetrathiomolybdate (ATTM)–based electrodeposition

ATTM, with a chemical formula $(NH_4)_2MoS_4$, has become a dominant precursor, as it can hypothetically donor both Mo and S through MoS_4^{2-} anion. The scenario of electrodeposition historically was estimated to be similar to the case of MoO_4^{2-}. The electrolytic reduction of tetrathiomolybdate (MoS_4^{2-}) to give MoS_2 may proceed in a similar manner to the well-known reduction of molybdate (MoO_4^{2-}) to MoO_2. The corresponding reduction schemes were considered as follows [97]:

$$MoO_4^{2-} + 2e^- + 2H_2O \rightarrow MoO_2 + 4OH^- \quad (1.23)$$

$$MoS_4^{2-} + 2e^- + 2H_2O \rightarrow MoS_2 + 2SH^- + 2OH^- \quad (1.24)$$

Currently, a typical electrochemical MoS_2 deposition bath can be filled with aqueous ATTM solution in excess of supporting electrolyte or ATTM solution in ethylene glycol [96]. A number of publications have reported the electrodeposition of Mo–S films from ATTM by cyclic voltammetry and potentiostatic electrolysis techniques.

Cyclic voltammetry (CV) in an aqueous solution of ATTM was initially studied and optimized for Mo–S film formation. Potential was cycled from 0.3 V to –0.8 V vs. SHE at a scan rate of 50 mV/s. One reduction and one oxidation peak grew concomitant with film formation. The thickness of the electrodeposited films increased with the number of scanning cycles and the 25 scans were optimized to form a brownish film on the electrode. The deposition has been successful for various conductive substrates, such as fluorine-doped tin oxide (FTO), indium tin oxide (ITO), and glassy carbon electrodes. A mixture of amorphous MoS_3, MoS_2, and other sulfur species were found to be deposited. Three processes, including oxidative deposition, reductive corrosion and reductive deposition, were identified in the cyclic MoS_x films deposition mechanism [95, 98, 99]. Recently, cyclic voltammetry was also employed to deposit $[MoS_4]^{2-}$ from an ionic liquid electrolyte for an alternative nonaqueous electrodeposition technique [100].

Constant anodic (at 0.7 V vs. RHE) and cathodic (at –0.3 V vs. RHE) potential electrolysis were employed for 1h to deposit films on FTO substrate from an aqueous ammonium tetrathiomolybdate solution. The two potentiostatic methods yielded films with different proportions of amorphous MoS_3 and MoS_2 phases: films produced by anodic electrolysis contained mainly amorphous MoS_3, while the deposition at the constant cathodic potential gave an amorphous composition, with Mo:S ratio close to 1:2 but a different chemical environment than crystalline MoS_2 (i.e. was named MoS_{2+x}). The amorphous MoS_3 film was not stable in 1 M KOH and quickly dissolved in the electrolyte, while the MoS_{2+x} composition was stable in alkaline solutions [99, 101]. However, Hu's group concluded that reductive activation occurs during HER and different amorphous phases of prepared films transforms to the active catalytic species of MoS_{2+x}.

(2) ATTM–free electrodeposition

To the best of our knowledge, reports of the electrodeposition of Mo–S without using ATTM are limited. After a review of related studies, the ressearch noted that ionic liquids, particularly, were employed for nonaqueous electrodeposition of Mo–S, while MoO_4^{2-} was generally found to occur in the majority of aqueous electrolytes.

Stevenson and co-workers reported the electrodeposition of nonaqueous-based flower-shaped molybdenum sulfide on glassy carbon from room temperature ionic liquids. Molybdenum glycolate and 1,4-butanedithiol served as the Mo and S precursors in the RTIL, and potentiostatic regime (–2.7 V) worked for two hours deposition at 100 °C [100]. The electrodeposition of MoS_2 from high-temperature molten salts is known to produce large, well-defined crystals; unfortunately, use of this method is seldom justified, as drastic electrolysis conditions must be employed, and temperatures of greater than 800 °C are required to melt the salts [96].

The fact that the electrodeposition potential of Mo is more negative than the discharge potential of hydrogen creates difficulties in the cathodic electrodeposition of Mo–S films from aqueous solutions. Furthermore, molybdenum compounds are known to be easily oxidized, and oxides form inevitably on their surface (Fig. 1.12) [94]. In terms of redox chemistry, MoO_4^{2-} is believed to be the dominant Mo species in an aqueous solution. Protonated species are typically important only at pH < 6, but may play a role in Mo adsorption on cationic surfaces. Polynuclear species of Mo (such as $Mo_7O_{24}^{6-}$ and $Mo_8O_{26}^{4-}$) are observed rather than MoO_4^{2-} at pH < 8. It should be noted that the redox behaviour, charge, coordination, and ionic radii of MoO_4^{2-} are similar to those of SO_4^{2-} [102].

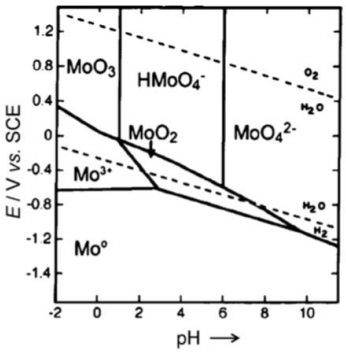

Fig. 1.12. Potential–pH diagram of a Mo–H_2O system [94]

In the context of the chalcogenides family, MoO_4^{2-} is used as a Mo source for the preparation of films of molybdenum selenides. Chandra and Sahu [103] performed electrodeposition from an ammoniacal solution of H_2MoO_4 and SeO_2 (pH 9.7) under galvanostatic electrolysis conditions. It was suggested that the presence of selenium leads to an „induced co-deposition" mechanism (i.e. Mo deposition follows Se deposition) with the possibility for $MoSe_2$ to be formed at some intermediate layers. In addition, a sulfamatic solution containing Na_2MoO_4 and H_2SeO_3 (pH 6.5) was also used to deposit Mo–Se thin films on SnO_2 coated glass substrates under potentiostatic conditions [104]. XRD analysis of the films indicated that they were composed of crystalline $MoSe_2$ with MoO_2 impurities. However, today it is widely accepted that cathodic processes yield oxo-compounds of Mo [97].

Only a few successful attempts of the electrodeposition of MoS_2 in a similar manner to that of $MoSe_2$, i.e., using MoO_4^{2-} as a simple, stable, and widely available Mo precursor, have been reported [97, 105]. In these reports, an aqueous solution of

Na_2MoO_4 and Na_2S was used and hydrochloric acid was added to the solution to adjust the pH to 8.0. The mixture of precursors resulted in the formation of tetrathiomolybdate via a chemical reaction in the deposition bath. Potentiostatic deposition was performed, and amorphous films containing Mo, S, and appreciable amounts of oxygen were obtained as a result of the aqueous room temperature electrodeposition. Annealing of these films in an inert atmosphere resulted in the formation of highly-textured films of MoS_2 with van der Waals planes parallel to the substrate. As oxygen was an inevitable component of the deposits, the electrodeposited material was later identified as molybdenum oxosulfides [97, 105].

Na_2MoO_4 and Na_2S were again used as the Mo and S precursors with sulfuric acid as the pH regulator. Various substrates were found to be suitable for the deposition. The electrochemical reduction of thiomolybdate, which was chemically derived from the precursors, was detected at a potential of about –0.3 V vs. Ag/AgCl, and the deposited material was identified as MoS_x [106].

A two-step electrochemical/chemical method was employed to synthesize molybdenum disulfide nanostructures according to the following equations:

$$MoO_4^{2-} + (4-x)H_2O + (6-2x)e^- \rightarrow MoO_x + (8-2x)OH^- \quad (1.25)$$

$$MoO_2 + 2H_2S \rightarrow MoS_2 + 2H_2O \quad (1.26)$$

First, amorphous MoO_x (a mixture of MoO_2 and MoO_3) was potentiostatically electrodeposited (E varied from –0.75 to –0.85V vs SCE; deposition time varied from 25s to 200s) by an electrochemical step-edge decoration technique from a basic aqueous solution of Na_2MoO_4 (pH 8.5). Subsequently, the MoO_x precursors were chemically converted to MoS_2 by heating in a tube furnace at 500–1000 °C under flowing H_2S for 5–84 h [107].

Clearly, a great deal of further investigation into the use of alternative Mo and S precursors (i.e. other than ATTM) in the electrochemical synthesis of amorphous molybdenum sulfides remains to be done. From a practical standpoint, in order to produce a MoS_x-like stable HER catalyst with enhanced activity when combined with other metals, it is necessary to find other suitable Mo sources, replacing a hard-to-control aqueous complexes, like ATTM.

1.3.4. Co–Mo–S films

Traditionally, interest in a mixed cobalt-molybdenum catalyst (oxides and sulfides) has appeared from an environmentally and technologically important hydrodesulfurization (HDS) process, where nanocrystalline binary chalcogenides were successfully employed to remove S from natural gas and refined petroleum products. The effects of synergy (cooperation between two phases) and promotion (increase of activity induced by the presence of a second metal) were developed in order to explain the enhanced reactivity of the Co–Mo–S materials [108].

The binary metal sulfide is generally interpreted as Mo–S-based Co promoted material and it is more and more often adapted to catalyze HER. Chemical solution-based, deposition-precipitation, photochemical, hydrothermal, and sulfurization methods can be found to be studied with the result of various Co–Mo–S compositions [109-115]. To the best of the researchers' knowledge, only a few successful attempts have been reported for electrodeposition of Co–Mo–S structures.

Being a first violin in this field, the work of Hu's group must be discussed more thoroughly [116]. Hu's group reported that transition-metal ions such as Fe, Co, Ni, Mn, Cu ans Zn could promote the catalytic activity of amorphous molybdenum sulfide (MoS_x) films that were prepared by cyclic voltammetry in an aqueous precursor solution. Among other transition-metal promoters, cobalt exhibited the best promotional effect on MoS_x catalysts for HER [116]. The Co–Mo–S films were prepared on ITO or glassy carbon electrodes, when an aqueous solution of $(NH_4)_2MoS_4$ and $CoCl_2$ precursors was the subject of 25 consecutive cyclic voltammetric scans in a potential window between +0.1 and –1.0 V vs. $Ag/AgCl_{sat}$. The concentration ratios of Co^{2+} and MoS_4^{2-} precursors were varied between 1:200 and 1:2. It was observed that when the ratio exceeded 1:2, a precipitation occurred upon mixing precursors; however, the Co–Mo–S films prepared with Co to Mo ratio being 1:3 exhibited the highest activity. A hyphothesis on the origin of Co promotional effect was proposed. Firstly, it was indicated that Co ions promote the growth of the MoS_3 structures, increasing its surface area and catalyst loading. Additionally, the incorporation of Co ions changes both the morphology of theoretical MoS_2 crystals and the instrinsic activity of them. Particularly, the Mo-edges, partially covered by adsorbed sulfur atoms, are known to be catalytically active sites and, in constrast, bare sulfur edges in these strucutures that are not catalytically active. As a result of promotion, the Co ions are located at the inactive sites and the Co-binding S-edges become catalytically active. As prepared Co–MoS_3 films showed amorphous structure and the "defect sites" in these materials were related to unsaturated Mo and Co-binded S-edges where HER may take place. Finally, the Co–Mo–S films showed enhanced HER activity in pH 7 phosphate buffer solution (at η=200 mV, the current density of Co-promoted film was five times of that of the unpromoted film) and less pronounced promotion effect in pH 0 solution (three times, respectively) [116].

The successful studies of Hu's group was recently repeated by Wang and co-workers. Hexagram-like CoS–MoS_2 composites were prepared on different substrates via a similar electrodeposition procedure of cyclic voltammetry by using $Co(NO_3)_2$ and ATTM as Co and Mo–S precursors with the ratio of 1:2. The prepared electrocatalysts were examined by various electrochemical techniques and showed improved catalytic activity and stability properties in an acidic media when compared with unpromoted analogue [117].

A potentiostatic electrodeposition technique was employed to prepare a 3D cathode of $CoMoS_x$ on a carbon cloth substrate (CC). The electrodeposition was optimized to operate at –0.5 V for 2h in the solution of $Co(NO_3)_2$ and ATTM in pH 7 phosphate buffer solution. Co ions were reported to be incorporated into the 3D structure of $CoMoS_x$ and thus enhance the catalytic activity of HER in an acidic solution. Similarly to the work of Hu's group, the current density of $CoMoS_x$/CC was more than 5 times larger than of MoS_x/CC at η=180 mV [118].

The electrodeposition bath was very recently changed by Al-Mayouf and co-workers where $CoCl_2 \cdot 6H_2O$, $Na_2MoO_4 \cdot 2H_2O$, and thiourea were reported to be used as Co, Mo and S precursors, respectively. Deposition of $Co_{1-x}Mo_xS$ film on FTO glass substrate was performed by cyclic voltammetry with 25 cycles. However, a very poor description of synthesis conditions without precise deposition bath composition is

provided in this work. These CoMoS/FTO catalysts were compared with CoS/FTO analogues in acidic HER performance and, at η=250 mV, the current density was almost 1.5 times larger for CoMoS/FTO electrodes [119].

The electrodeposition-based strategies for Co–Mo–S films are still on a small-scale, which is why it is essentially useful to familiarize with more developed perceptions in this field. Markovic and co-workers [109] established activity and stability trends for commercially available crystalline and chemically prepared amorphous molybdenum sulfides, cobalt sulfides and cobalt-molybdenum sulfide materials. These relationships were expressed in a background of a reaction overpotential (η) required for a constant current density of 5 mA/cm^2 (Fig. 1.13). When compared between trends in activities for the HER (Fig. 1.13 a), both crystalline and amorphous CoS_2 and CoS_x are always more active than MoS_2 and MoS_x, respectively. The activity of $CoMoS_x$ is shown to be almost independent of pH and is in the average values among both the Co and Mo candidates. On the other hand, the most active amorphous CoS_x is the least stable material (Fig. 1.13 b) in acidic and alkaline solutions. It was determined that MoS_x is less active but ~35–40 times more stable than CoS_x analogues. In addition, Mo^{4+} was established to be almost as equally stable in both chemically prepared $CoMoS_x$ and MoS_x, indicating that the Co-based building blocks can be stabilized in the $CoMoS_x$ structures [109].

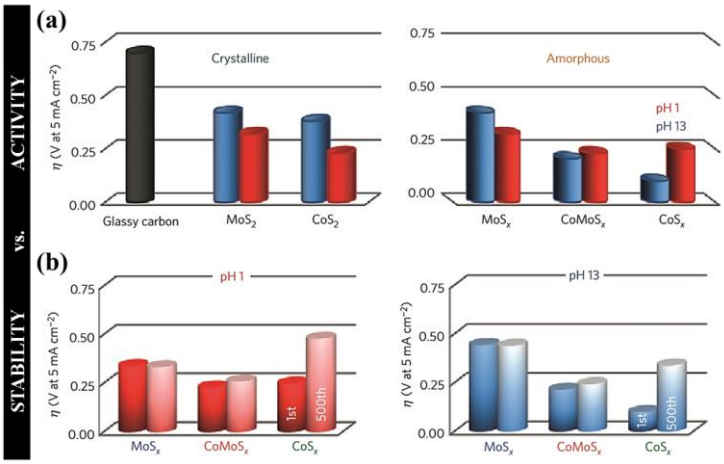

Fig. 1.13. Activity–stability relationships in transition metal sulfides for the HER (Modified from Ref. [109])

Beyond doubt, it is reasonable to combine the active cobalt sulfide building blocks with the more stable molybdenum sulfide units into one composition of Co–Mo–S catalytic material suitable for the HER. In this regard, an electrochemical deposition method can be suggested to be employed, as it is proved to be a convenient method for amorphous Co or Mo sulfide films formation.

2. METHODOLOGY

2.1. Materials

Thiourea ($(NH_2)_2CS$, ≥ 99%, Sigma Aldrich), cobalt (II) chloride hexahydrate ($CoCl_2 \cdot 6H_2O$, ≥ 99%, Sigma Aldrich), ammonium molybdate tetrahydrate ($(NH_4)_6Mo_7O_{24} \cdot 4H_2O$, ≥ 99%, Reachem, Slovakia), ammonium tetrathiomolybdate (ATTM) ($(NH_4)_2MoS_4$, 99.97%, Sigma Aldrich) and sodium perchlorate monohydrate ($NaClO_4 \cdot H_2O$, Reachim, Russia) were used as chemicals for the catalysts preparation. Hydrochloric acid (HCl, ≥ 37%, Reachem, Slovakia) was employed to control the pH of aqueous synthesis solutions. Dipotassium phosphate (K_2HPO_4, ≥ 99 %, Reachem, Slovakia) and potassium dihydrogen phosphate (KH_2PO_4, ≥ 99.5 %, Reachem, Slovakia) were used to prepare the phosphate buffer solution of pH 7. Sulfuric acid (H_2SO_4, ≥ 96.7%, Reachem, Slovakia) solution of pH 0 was prepared for additional electrochemical measurements. All reagents used in the experiments were purchased from commercial sources and used without further purification.

2.2. Films formation

Cyclic voltammetry (CV) was employed for the electrodeposition of the films on the FTO substrate. The potential was cycled from –1.2 V to 0.2 V vs. Ag/AgCl and maintained for all types of films. Prior to deposition, the fluorine-doped tin oxide (FTO) glass substrates (TEC15, 3.5 × 1 cm, 13 Ω/sq) were cleaned successively using a soap solution, deionized water and acetone in an ultrasonic bath. The thus-prepared FTO plates were used as working electrodes in a thermostated three electrode cell with Ag, $AgCl|KCl_{(sat)}$ as a reference electrode and platinum wire (geometric area about 15 cm^2) as a counter electrode. The working and counter compartments of the cell were separated by the frit. All three electrodes were placed in a 100 mL deposition bath. Initial aqueous solutions of 1 M $(NH_2)_2CS$, 0.05 M $CoCl_2$, 0.05 M $(NH_4)_6Mo_7O_{24}$, and 0.05 M $(NH_4)_2MoS_4$ were used to prepare various deposition solutions with the required concentration of each precursor. The as-synthesized samples were thoroughly washed with distilled water and dried at room temperature. Some thiourea-derived samples were additionally annealed at 300 °C for 3 h under a flow of nitrogen.

Synthesis of Co–O–S films. The synthesis of Co–O–S thin films at room temperature was adapted from Sun et al. [80]. Following this procedure, the Co–O–S films on the FTO substrate were deposited using an electrosynthesis bath (100 mL) containing 0.005 M $CoCl_2$ and 0.5 M thiourea (initial pH 7), as cobalt and sulfur precursors, respectively. A various number of sweep cycles were used to form Co–O–S films and the deposition at temperatures from 20 to 50 °C were examined in this work. During all the experimental runs, intense black appearance films were obtained after electrodeposition.

Synthesis of Mo–O–S films. The electrodeposition of Mo–O–S films films was performed at room temperature using two different Mo and S precursor baths: (a)

ammonium tetrathiomolybdate (ATTM; $(NH_4)_2MoS_4$), and (b) a solution of thiourea (TU; $(NH_2)_2CS$) and ammonium molybdate ($(NH_4)_6Mo_7O_{24}$).

a) The ATTM-derived films were prepared by using a one-step electrodeposition method developed recently [98]. On the basis of this work, the deposition bath (100 mL) containing 0.005 M ATTM and 0.1 M $NaClO_4$ (initial pH 5.7) was prepared. These films were deposited by 20 sweep-cycles at a scan rate of 50 mV/s and used as a benchmark of molybdenum sulfide film.

b) The Mo–O–S samples were deposited from an electrolysis bath (100 mL) containing 0.5 M thiourea and 0.005 M ammonium molybdate (initial pH 8.3). Three sweep-cycles were applied for films formation while potential was cycled at a scan rate of 5 mV/s. These experimental conditions were adapted following the Co–O–S synthesis procedure described above.

During all the experimental runs, intense brownish films were obtained as a result of electrodeposition.

Synthesis of Co–Mo–O–S films. Co–Mo–O–S films deposition on FTO substrate was performed at room temperature by using two different deposition baths.

a) The amount of cobalt salt added to the ATTM solution was based on the optimal Co(II)-salt:ATTM ratio of 1:3 reported earlier [116]. The synthesis solution (100 mL) containing 0.0017 M $CoCl_2$, 0.005 M ATTM and 0.1 M $NaClO_4$ (initial pH 5.3) was used to deposit ATTM-derived Co–Mo–O–S films by 20 sweep-cycles at a scan rate of 50 mV/s. The brownish films were obtained as a result of electrodeposition.

b) Following the methodologies of Co–O–S and Mo–O–S (b) films formation, the electrolysis bath (100 mL) containing 0.005 M $CoCl_2$, 0.005 M ammonium molybdate and 0.5 M thiourea (initial pH 8) was composed to deposit molybdate-thiourea-based Co–Mo–O–S films by 3 sweep-cycles at a scan rate of 5 mV/s. To further analyze these Co–Mo–O–S samples, a number of synthesis parameters were changed and evaluated experimentally, i.e. the concentration of Co and Mo precursors, pH of the deposition bath and the number of deposition sweep cycles.

2.3. Analytical techniques

X-ray diffraction (XRD) patterns were recorded on a D8 Advance diffractometer (Bruker AXS, Karlsruhe, Germany) with CuKα radiation. The film specimens were scanned over the range $2\theta = 5–70°$ at a scanning speed of $6°\ min^{-1}$ using a coupled two theta/theta scan type.

Scanning electron microscopy (SEM) was employed for the examination of the surface morphology and elemental composition of the samples. Images were obtained using a Quanta FEG 200 (FEI) high resolution scanning electron microscope equipped with a detector (Bruker AXS) for high resolution *energy dispersive X-ray spectroscopy (EDX)*.

Fourier transform infrared (FT–IR) spectra of the samples were recorded on a Perkin Elmer FT–IR Spectrum X System. KBr was used to pellet the samples, and the scans were conducted over a 400–4000 cm^{-1} scanning range.

Raman spectroscopy measurements were performed using an *inVia* Raman microscope (Renishaw). The excitation beam from a diode laser with a wavelength of

532 nm was focused on the sample. The laser power on the sample surface was varied from 0.35 mW to 3.5 mW. The integration time was 5–10 s, and the signal was accumulated 1–5 times and then averaged. The Raman Stokes signal was dispersed using a diffraction grating (2400 grooves/mm), and data was recorded using a Peltier-cooled charge-coupled device (CCD) detector (1024 × 256 pixels). This system yields a spectral resolution of about 1 cm^{-1}. Silicon was used to calibrate both the wavenumber and spectral intensity of the Raman setup.

UV–Vis diffuse reflectance (UV–Vis DR) spectra were recorded using a Lambda 35 UV–Vis spectrometer (Perkin Elmer Instruments Co. Ltd., USA) equipped with a 50 mm machined Spectralon® integrating sphere. A $BaSO_4$ disc was employed as a reference. The scan ranged from 200 to 800 nm.

Atomic force microscopy (AFM) topographic images were obtained using NT–206 (Micro-test machines Co., Ltd., Belarus) atomic force microscope with stationary mode probe in air at ambient conditions. 9x9 μm was selected as the maximum scanning area and a scan rate of 10 μm/s was used in the X–Y plane.

X–ray photoelectron spectroscopy (XPS) was performed for chemical analysis of the samples by using a PHI 5000 VersaProbe (ULVAC–PHI, Inc., Japan) spectrometer. The samples were analyzed using monochromated 1486.6 eV Al radiation; 25 W beam power; 100 μm beam size; and 45° measurement angle. Sample charging was compensated using a dual neutralization system consisting of a low energy electron beam and an ion beam and fixing adventitious carbon C 1s peak at 284.8 eV. Survey spectra were acquired using 180 eV pass energy, 1 eV step size and 0-1350 eV analysis range, whereas individual high resolution core electron spectra were measured using 180 eV pass energy, 0.1 step size and 20-30 eV spectral ranges.

Atomic absorption spectroscopy (AAS) analysis was performed with a Perkin Elmer 403 spectrometer. The radiation source was a hollow cathode lamp. The atomization was carried out in a flame by using the acetylene-air mixture. While determination of atomic cobalt by AAS was not successful because of low solubility of Co–O–S-based structures, the content of molybdenum in the Co–Mo–O–S coatings was determined by dissolving samples in 1 M NaOH and measuring the absorption at 313.26 nm.

The thickness of the as-deposited films was measured using an Ambios XP–200 *profilometer*.

The pH of solutions was measured by using a Knick 766 Laboratory *pH-meter*.

The electrochemical measurements of the potentiodynamically deposited Co–O–S, Mo–O–S and Co–Mo–O–S samples were evaluated using a computer–controlled potentiostat/galvanostat BioLogic SP–150 (Science Instruments, France) connected to a three-electrode cell. Linear sweep voltammetry, chronopotentiommetry and chronoamperommetry methods were typically applied to evaluate the electrocatalytic behavior of the prepared films. EC–Lab V10.39 software was used for the collection and treatment of experimental data. The FTO/sample plate was used as the working electrode, a platinum wire as the counter electrode, and Ag, AgCl| $KCl_{(sat)}$ as the reference electrode. The electrochemical tests were performed in a 1 M potassium phosphate buffer solution (pH 7) and 1 M sulfuric acid solution (pH 0). A polycrystalline platinum plate (geometrical surface area 2 cm^2) was

also polarized in the phosphate buffer and sulfuric acid solutions and used as a benchmark for comparison with the prepared Co–O–S, Mo–O–S and Co–Mo–O–S samples.

The experimental data analysis was performed by OriginLab Corporation® OriginPro 2015 and Microsoft® Excel 2013.

3. RESULTS AND DISCUSSION

3.1. Synthesis and electrocatalytic behaviour of Co–Mo–O–S films

3.1.1. Synthesis of Co–O–S films

In earlier studies it was repeatedly suggested to form cobalt sulfide thin films by cyclic voltammetry (CV) [85, 86, 89]. As reported, thiourea (TU) and cobalt (II) chloride hexahydrate were commonly used as sulfur and cobalt donors. This experience was captured for the synthesis of S-containing cobalt oxide films (denoted as Co–O–S) by potentiodynamic deposition according to the procedure described in Methodology. The primary experimental part of the thesis was dedicated to investigate the influence of some typical electrochemical deposition factors, such as number of sweep cycles and electrolysis bath temperature. Generally, these are the factors that affect composition, thickness and density of the films. In order to establish the electrodeposition mechanism for Co–O–S compounds, repetitive potential cycling was under deeper investigation.

The obtained experimental results confirmed the possibility to form buildable Co–O–S films by varying the number of CV sweep cycles in a precursor electrolyte solution. 1, 3 and 5 continuous sweep cycles were applied to form homogeneous, intensive black appearance films. Figure 3.1 presents the cyclic voltammetric response recorded at FTO substrate by cycling the electrode potential from –1.2 V to 0.2 V. For clarity, the CV profiles of different sweep cycles are presented in separate graphs.

When sweeping negatively from the initial potential of 0.02 V, the cathodic process of cobalt compounds deposition was observed on the forward sweep with the following current loop in the reverse sweep (Fig. 3.1. A). This current loop is presumed to demonstrate the nucleation and the electrodeposition of metallic Co on the substrate surface [85]. Specifically, this current loop can be observed when the deposition of metals onto its own phase, in this case cobalt on cobalt phase, occurs at lower overpotentials than the deposition of metal onto the different nature substrates, in this case on FTO [120].

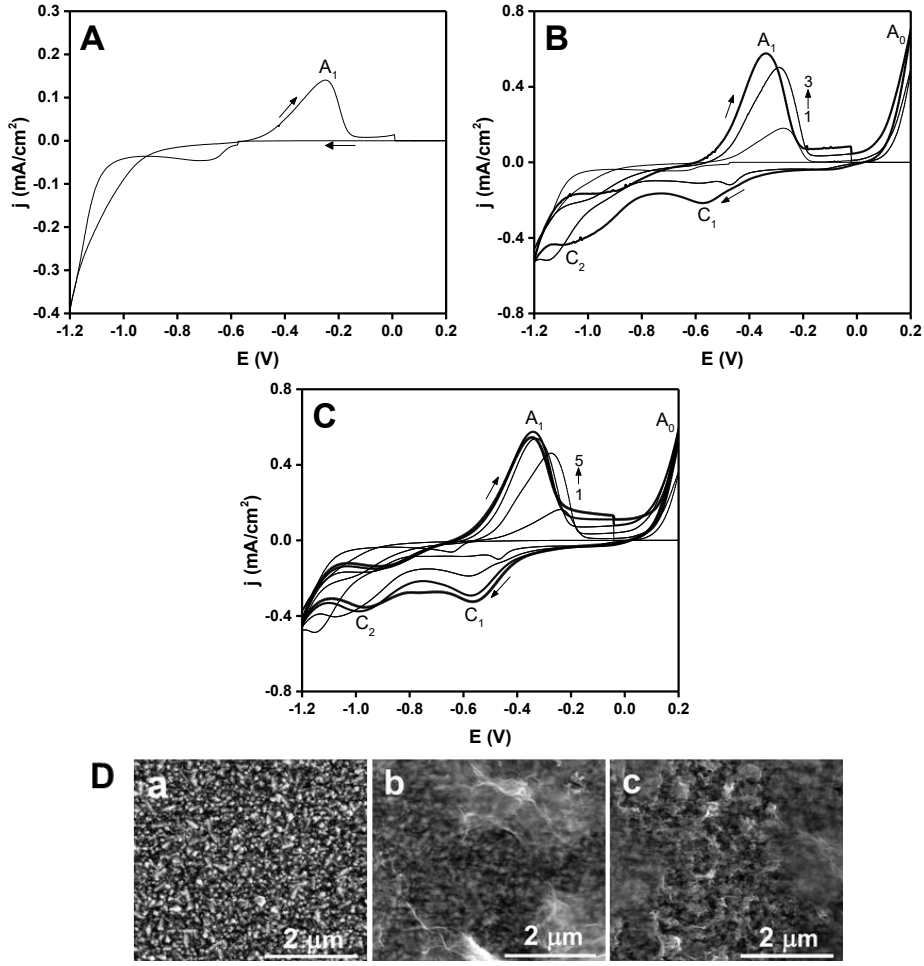

Fig. 3.1. Characteristic cyclic voltammograms of Co–O–S films on FTO substrate deposited by 1 (A), 3 (B) and 5 (C) sweep-cycles in electrolysis bath containing 0.5 M thiourea and 0.005 M $CoCl_2$ at a scan rate of 5mV/s. (D) SEM images of Co–O–S at × 50 000 magnification

It is known that the cobalt reduction takes place before water decomposition, since the standard overpotential of water decomposition is more negative than that of Co reduction [121]. The increase in cathodic current at potentials more negative than –0.8 V can be attributed to the prevailing hydrogen evolution reaction (HER) and this process can additionally be accelerated, even with a small quantity of cobalt-based deposits. The reactions involved can be outlined by the following equations [122]:

$$2H_2O + 2e^- \rightarrow H_2 + 2OH^- \quad (3.1)$$

$$Co^{2+}_{(aq)} + 2OH^- \rightarrow Co(OH)_{2(ads)} \quad (3.2)$$

$$Co(OH)_{2(ads)} + 2e^- \rightarrow Co_{(s)} + 2OH^- \quad (3.3)$$

Equations (3.1)–(3.3) and the following Co nucleation may increase the deposition rate on the bare FTO surface and the current loop did not appear during the repetitive potential cycling (Fig. 3.1 B and C), indicating the changes in the mechanism of film formation.

The following mechanism of the film formation can be related to the presence of repetitive peaks *A* and *C*. An anodic profile of cyclic voltammogram recorded on the reverse sweep (A_1) can be considered as a result of various overlapping effects. In particular, it can be attributed to the reverse of (3.3) equation or can be partly related to the formation of a duplex passive film of cobalt. The passivation of the Co electrode in neutral solutions involves water molecules adsorption on the electrode surface according to the equations [123]:

$$Co + H_2O \rightarrow Co(H_2O)_{(ads)} \quad (3.4)$$

$$Co(H_2O)_{(ads)} \rightarrow Co(OH)^+ + H^+ + 2e^- \quad (3.5)$$

$$Co(OH)^+ + H_2O \rightarrow Co(OH)_2 + H^+ \quad (3.6)$$

$$Co(OH)_2 \rightarrow CoO + H_2O \quad (3.7)$$

Further behavior is pH-dependent. Cobalt species are known to remain stable on the electrode surface in neutral media. Increased stability of the passive film and the transition to Co(III) compounds can be reached in basic solutions while the high rates of corrosion are typically recorded in acidic solutions [123]:

$$Co(OH)^+ + H^+ \rightarrow Co^{2+} + H_2O \quad (3.8)$$

However, it should be clearly emphasized that a large anodic peak A_1 cannot be entirely related only to the processes described by equations (3.4)–(3.7). As the electrolysis bath contains thiourea, its influence on the overall behaviour of the system needs to be elucidated. First of all, the electrochemical oxidation of the thiourea to formamidine disulfide (FD) takes place in this potential region [91]:

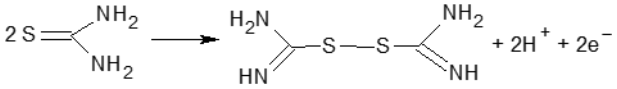

(3.9)

This thiourea oxidation is supposed to be a dominant process. A detailed CV analysis revealed that in the absence of thiourea, the significantly smaller anodic peak is recorded [68]. In addition, the current associated with this anodic peak increased upon the increase in thiourea concentration. It is important to note that the initial anodic peak is significantly increased and shifted to the more negative potentials during the repetitive potential cycling (Fig. 3.1 B and C). At more positive potentials, partial electrochemical oxidation of formamidine disulfide to other sulfur species can lead to the appearance of a peak A_0 occurring at the end of the upper sweep.

When the potential was reversed for the second scan, two corresponding cathodic peaks C_1 and C_2 appeared in the cyclic voltammogram. Accordingly, electro-reduction of sulfur species (such as FD and sulfur) to produce TU can be the origin of peak C_1 and the following peak C_2 can be attributed to the electro-desorption of TU/FD lattice from the electrode surface [72]. Therefore, a hypothesis can be made that this path of thiourea might source sulfur to Co-O-based electrode structures. A reduction of formed cobalt and thiourea (TU) complexes can be simply expressed by equations (3.10)-(3.11), which represent the most prominent path for electrochemical CoS film formation [85]:

$$Co^{2+} + 2TU \rightarrow Co(TU)_2^{2+} \quad (3.10)$$

$$Co(TU)_2^{2+} \rightarrow CoS \quad (3.11)$$

The emphasis and discussion according to equations (3.1)-(3.11) are beneficial and lead to a better perception of Co–O–S films formation. In parallel, morphological studies were employed to complement the fundamental data. The correlation between number of applied sweep cycles and morphology of Co–O–S films is illustrated in Figure 3.1 D. The dense layer of particles was detected after one-sweep-cycle deposition (Fig. 3.1 D-a). The multi-layer porous surfaces were formed during progression of the deposition process (Fig. 3 D-b, c). Part b of Figure 3.1 D illustrates a honeycomb-like structure with holes and folds generally associated with higher surface roughness. The layer of folds became more uniform and the deep network-like structure was observed when the deposition was performed under five-sweep-cycles conditions (Fig. 3.1 D-c). It is known that the high surface roughness and specific surface area with holes and deep-spaced formation are favourable factors in order to enhance the access of active sites and, therefore, the electrocatalytic activity of the electrode [81, 82]. On the other hand, a high porosity level can also be linked to unfavourable corrosion processes during electrolysis.

An acceleration of the deposition process was observed when the temperature of the deposition bath was raised from 20 °C to 50 °C (Fig. 3.2). 3 CV electrodeposition was selected as an adequate procedure to test the regularities and hence Figure 3.2 demonstrates the third sweep-cycles of Co–O–S electrodeposition at various temperatures. Independently of the electrolysis temperature, characteristic peaks, discussed earlier, remained the same. The current density of the characteristic peaks significantly increased as the temperature of the electrolysis bath was raised. It was observed that relatively thicker films can be obtained at higher temperatures. However, it should be emphasized that the quality of Co–O–S films deposited at > 20 °C was poorer, as they became cracked, less adhesive to the FTO surface, and had a tendency to peel off in the solution.

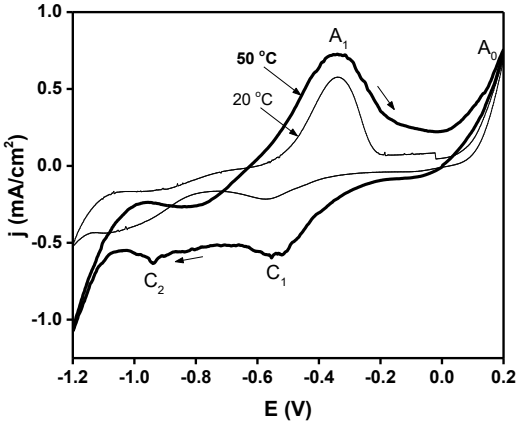

Fig. 3.2. Characteristic cyclic voltammograms of FTO/Co–O–S electrodes formation under 20 °C and 50 °C deposition temperatures. Synthesis was carried out at various temperatures electrolysis bath containing 0.5 M thiourea and 0.005 M $CoCl_2$ at a scan rate 5mV/s. Graph contains only the last sweep-cycles of 3 CV Co–O–S deposition

Even though only Co–O–S films prepared at room temperature showed potential for further studies, a brief insight into the XRD patterns of Co–O–S films electrodeposited by 3 CV at various temperatures is additionally presented in Figure 3.3. It can be highlighted that an amorphous nature was identified for all samples independently of the electrodeposition temperature. The weak broad peak located around $2\Theta = 10^{o}$ represented X-ray scattering in many directions and the lack of long range order in amorphous Co–O–S materials. To sum up, the subsequent research has been focused on the films electrodeposition only at room temperature conditions.

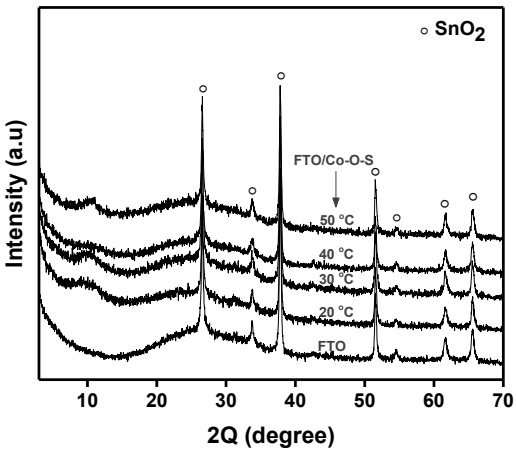

Fig. 3.3. X-ray diffraction patterns of bare FTO substrate and FTO/Co–O–S films prepared by 3 sweep-cycles under various temperatures

Linear sweep voltammetry was employed to evaluate the catalytic behaviour of the prepared Co–O–S films in a pH 7 phosphate buffer solution. Platinum plate, as the best known HER catalyst, and bare FTO substrate, as HER inactive material, were polarized as benchmarks. It is well known that platinum exhibits the highest HER catalytic performance with a near zero overpotential. Theoretically, HER on platinum performs at –0.6 V vs. sat. Ag/AgCl in pH 7. However, phosphate ions are known to affect the behaviour of working electrodes. This effect was noticed in the research case, as the overpotentials of Pt electrode in 1M phosphate buffer solution slightly shifted when HER was performed at the higher currents.

Polarization curves of bare FTO substrate and 1, 3 and 5-sweep-cycled Co–O–S samples are presented in Figure 3.4. A relatively low scan rate was used to utilize the layered honeycomb-like structure for charge migration on the whole surface areas [86]. It can be observed that the presence of Co–O–S significantly improves the catalytic behaviour of bare FTO substrate under HER conditions and current density tends to increase with the increase in the number of deposition sweep-cycles. While sweeping potential from 0 to –1.0 V, the recorded voltammograms exhibited an intense peak at –0.7 V and currents of HER, which started to occur from –0.8 V. It is assumed that the current grow with the peak at –0.7 V is related to the overlapping processes. On the one hand, these currents are in some cases associated with the hydrogen evolution initiated under significantly low overpotentials. This is generally

an indicator for high HER activity of amorphous cobalt sulfide compounds [68, 80]. On the other hand, it was noticed that this behaviour is probably also related to the Co(II) redox process that is responsible for film degradation inevitably observed after electrode polarization under HER conditions.

To sum up, the signs for enhanced activity of Co–O–S films are clear. However, the mechanism for catalytic behaviour is still under interpretations. The results of *operando* spectroscopic analysis of amorphous Co–S catalyst in electrochemical hydrogen evolution reaction suggested that the Co–S is spontaneously transforming into CoS_2-like molecular clusters under cathodic polarization [88]. Also, it has been estimated that Co–S electrocatalyst can contain roughly 60% of CoO and 40% of CoS in the dry state and 26% of CoO and 74% of CoS under HER conditions.

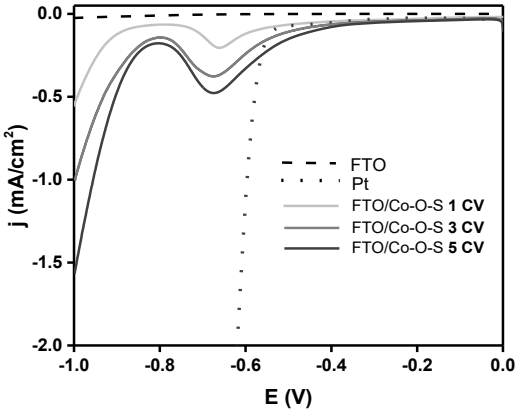

Fig. 3.4. Polarization curves of freshly prepared FTO/Co–O–S electrodes in phosphate buffer solution (pH 7) at a scan rate of 5 mV/s

3.1.2. Synthesis of Mo–O–S films

Ammonium tetrathiomolybdate (ATTM) is known as the most prominent source for both Mo and S through MoS_4^{2-} anion. However, in this work, research suggests for the first time an alternative electrodeposition bath containing thiourea (TU) and ammonium molybdate as the S and Mo sources, respectively. Based on the successful use of thiourea in the aqueous electrodeposition of cobalt–sulfide films, TU was chosen as the sulfur donor for the molybdenum-containing bath. Accordingly, the electrodeposition of S-containing molybdenum oxide films (denoted as Mo–O–S) was performed using two different Mo and S precursors: (A) ammonium tetrathiomolybdate and (B) a solution of mixed thiourea and ammonium molybdate.

Initially, the optimized cyclic voltammetry (CV) was used to prepare ATTM-based Mo–O–S films on the FTO substrates (Fig. 3.5 A). Therefore, the potential was cycled from 0.2 V to –1.2 V and one reduction and one oxidation peak were observed at –0.8 and –0.2 V, respectively. A homogeneous brownish film layer was deposited on the glass substrate after 20 continuous sweep cycles. The obtained experimental results were in good agreement with the proposed mechanism of film formation (eqs. (3.12)–(3.14)) [95, 98].

$$MoS_4^{-2} \rightarrow MoS_3 + \frac{1}{8}S_8 + 2e^- \quad (3.12)$$

$$MoS_3 + \frac{1}{8}S_8 + 2e^- \rightarrow MoS_4^{-2} \quad (3.13)$$

$$MoS_4^{-2} + 2H_2O + 2e^- \rightarrow MoS_2 + 2HS^- + 2HO^- \quad (3.14)$$

The anodic peak at –0.2 V can be assigned to the oxidation of aqueous MoS_4^{2-} followed by MoS_3 deposition, as described in equation (3.12). When the potential was cycled in reverse from 0.2 V in the negative direction, reductive corrosion was reported to consume about 70% of the previous deposits via the reaction in equation (3.13) [95]. Finally, the cathodic peak at –0.8 V may indicate the further reduction of MoS_4^{2-} to form amorphous MoS_2, HS^-, and HO^- (eq. 3.14). According to this mechanism, potential cycling of a MoS_4^{2-} solution would always produce a molybdenum sulfide film that is a mixture of amorphous MoS_3, MoS_2, other sulfur species, and the inevitably formed oxo compounds.

However, it has been observed experimentally that ATTM, as a precursor, has some limitations. Before electrolysis, its stability is problematic due to the oxidation of Mo and S species in aqueous solutions under an air atmosphere. Furthermore, it was noticed that during electrolysis the surfaces of electrochemical cells were covered with a thin layer of unidentified and very difficult to remove residues. Thus, the development of an alternative electrolysis bath is highlighted here in order to make the synthesis more economical and environmental friendly.

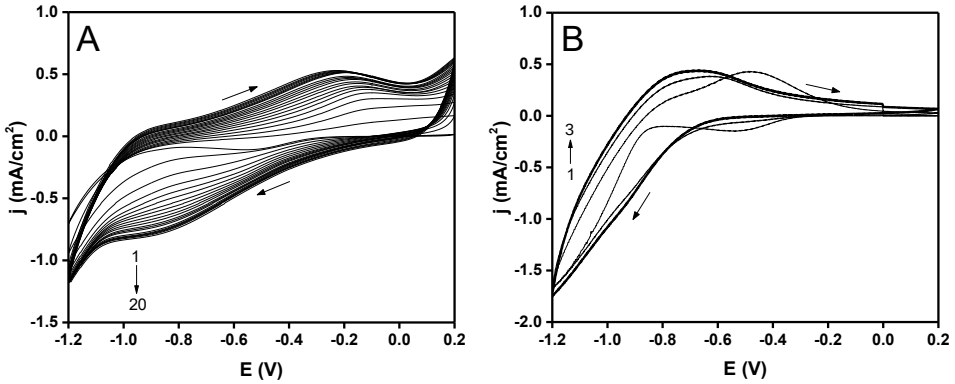

Fig. 3.5. Characteristic cyclic voltammograms of Mo–O–S deposition on FTO. (A) 20 sweep-cycles in an electrolysis bath containing 0.005 M ATTM and 0.1 M $NaClO_4$ and (B) 3 sweep-cycles in an electrolysis bath containing 0.5 M thiourea and 0.005 M ammonium molybdate

In parallel with methodology of the sucessful Co–O–S deposition from thiourea and cobalt salt, 0.5 M thiourea and 0.005 M ammonium molybdate were used to fill the deposition bath for ATTM-free synthesis of Mo–O–S. In the thiourea–molybdate electrolysis bath, the FTO electrode was cycled continuously from 0.2 V to –1.2 V until a thin layer of brownish film was observed to deposit on the working electrode after three sweep cycles. Profilometry measurements revealed that the thickness of the deposited films after three sweep cycles using the thiourea–molybdate bath was 245 nm; this value was more than 100 nm greater than that of the ATTM-derived films

deposited after 20 cycles. It should also be noted that the synthesis from an ATTM-based electrolysis bath was previously reported to have an upper film thickness limit of less than 200 nm, even after 35 scan cycles [98].

The cyclic voltammograms corresponding to the thiourea–molybdate-based film are presented in Figure 3.5 B. The first of the three CV deposition cycles exhibited two redox peaks (at –0.45 V and –0.5 V), which were very likely related to the formation of a molybdenum oxide layer on the bare electrode surface [94]. This behaviour was not observed during the later scans. Starting from the second sweep, the CVs do not exhibit the redox peaks that are typically observed during Mo–O–S film formation from an aqueous MoS_4^{2-} solution (Fig. 3.5. A). This can be considered the first indicator that this precursor mix $(NH_4)_6Mo_7O_{24}$ + $(NH_2)_2CS$ does not complex to form aqueous MoS_4^{2-} prior to electrodeposition and film formation, probably, it proceeds via different a mechanism than that described in equations (3.12) – (3.14). This result may also be consistent with other studies [124–126], reporting the possibility of forming flower-like molybdenum sulfide nanostructures from thiourea and ammonium molybdate via a hydrothermal synthesis procedure without thiomolybdate ion intermediates. In particular, the group of Geng showed [124] that thiourea successfully supplied S to MoO_3 formed beforehand from $(NH_4)_6Mo_7O_{24}$. The following chemical reactions were suggested to be involved during the hydrothermal process [126]:

$$CSN_2H_4 + 2H_2O \rightarrow 2NH_3 + CO_2 + H_2S \quad (3.15)$$

$$(NH_4)_6Mo_7O_{24} \rightarrow 6NH_3 + 7MoO_3 + 3H_2O \quad (3.16)$$

$$MoO_3 + 3H_2S + H_2O \rightarrow MoO_2 + SO_4^{2-} + 2H^+ \quad (3.17)$$

$$MoO_2 + 2H_2S \rightarrow MoS_2 + 2H_2O \quad (3.18)$$

In this stage of work, an alternative film formation mechanism can be suggested based on the obtained results. The film formation likely occurs via the deposition of Mo–O species followed by electro-adsorption of the S ligand on the Mo–O covered FTO surface. This mechanism can be justified by the following arguments. Firstly, the possibility of the precursors chemically complexing to form aqueous MoS_4^{2-} can be preliminary rejected, as none of the characteristic visible solution features of MoS_4^{2-} were observed after mixing the thiourea and molybdate solutions. Secondly, it is assumed that the increase in the cathodic current at potentials more negative than –0.6 V can be attributed to the deposition of molybdenum oxide compounds. This step is predominantly associated with the electrodeposition of metals from the aqueous solution at negative potentials accompanied by the parallel electrolysis of water, rather than the reduction and deposition of aqueous S species which were detected in this potential region when ATTM was used (Fig. 3.4 A) or in the cases for Co–O–S prepared by 3–5 CVs (Fig. 3.1). Taking into account the complex solution chemistry of Mo(VI), the cathodic electrodeposition is known to lead to nonstoichiometric and mixed valence molybdenum oxides, making the formulation of precise deposition mechanism impossible [94]. However, the electroreduction of molybdates can be expressed in a general way as follows [127]:

$$MoO_4^{-2} + 2H_2O + 2e^- \rightarrow MoO_2 + 4OH^- \quad (3.19)$$

It is presumed that this behaviour results in the FTO electrode being predominantly covered with Mo–O species. This type of surface should be negatively charged, according to the zeta potential data for Mo-oxo compounds [128]. It is well-established that thiourea can be electro-adsorbed on metals by S-head [70, 72, 73]. This process is electrochemically driven by the electrostatic forces between the electrolyte ions and the charged interfaces. Thus, the anodic peak at –0.7 V can be attributed to the electro-adsorption of TU on the negatively charged Mo–O surface. As aqueous thiourea is known to be positively charged (i.e. protonated) at the S atom (eq. 3.20) [129], its electro-adsorption could be the dominant process occurring on the negatively charged Mo–O surface, producing a final layer of Mo–O–S structures on the FTO substrate.

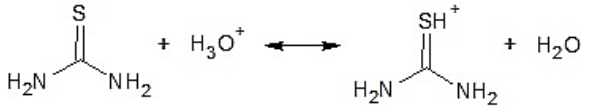

(3.20)

This thiourea behaviour slightly deviates from the mechanism that would be expected, based on the electrodeposition of an amorphous cobalt sulfide film using thiourea and cobalt salt, as discussed in previous parts of results and related to studies [68, 80, 88]; on the other hand, it corresponds well with the fundamentals of the formation of self-assembled (SA) monolayers of alkanethiols and S-donation through the electro-adsorption of the cleaved S-H thiol bond [72, 73, 75].

Finally, a homogeneous, brownish film, visually identical to that produced from ATTM was formed on the FTO substrate as a result of the three continuous sweep cycles. The presence of Mo, O, and S was later confirmed by compositional analysis, while the electrocatalytic properties of the film in the HER were compared with two benchmarks: the ATTM-based film and a polycrystalline Pt electrode.

The catalytic performance of the Mo–O–S films in the HER at pH 7 in a phosphate buffer solution was studied using a combination of chronopotentiometry and linear sweep voltammetry techniques. The galvanostatic method is known to be attractive for short-term electrochemical stability measurements when electrodes are tested under harsh current conditions [130], and 10 mA/cm^2 is known to be the current density required to produce industrial amounts of H_2 at low overpotentials. The research tested the catalysts at half the industrial value of 10 mA/cm^2 in order to simulate constant and intense H_2 evolution conditions, which are difficult to achieve in neutral solutions in typical *E-j* or *time-j* measurements. A current density of 5 mA/cm^2 has also been reported to be convenient to establish activity in the form of the reaction overpotential at a constant current density [109].

Figure 3.6 shows characteristic chronopotentiograms of the deposited Mo–O–S films at a constant cathodic current density of 5 mA/cm^2. As expected, the Mo–O–S film prepared from the ATTM precursor remained mechanically stable, despite the harsh electrolysis conditions with intense H_2 bubbling. However, the overpotential required to produce a cathodic current density of 5 mA/cm^2 using this film was relatively high, and the reaction potential showed a tendency to increase due to the gradual dissolution of the ATTM-derived Mo–O–S film (Fig. 3.6 A). The film prepared from molybdate and thiourea was also tested under the same HER conditions of 5 mA/cm^2 (Fig. 3.6 B). In contrast to the ATTM-derived film, the ATTM-free catalyst reached similar catalytic activity without noticeable film degradation. The

potential did not change more than 20 mV during the whole electrolysis. These results showed the possibility for the catalyst prepared using thiourea and molybdate as Mo and S precursors to operate at the same rate as the reference ATTM-derived Mo–O–S film.

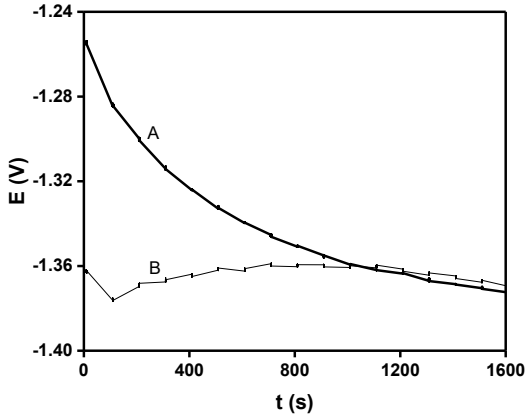

Fig. 3.6. Characteristic chronopotentiograms recorded in a pH 7 phosphate buffer solution at a constant applied current density of 5 mA/cm^2 for the Mo–O–S films prepared from (A) ATTM in $NaClO_4$ and (B) thiourea and ammonium molybdate solutions

Figure 3.7 represents the polarization curves of the ATTM-derived (Fig. 3.7 A) and thiourea-molybdate-based (Fig. 3.7 B) catalysts in a pH 7 phosphate buffer solution. These catalysts were polarized from 0 V to –1 V before and after being used for electrolysis at 5 mA/cm^2 for 1600 s. This methodology allowed the changes to the films caused by the HER to be detected and compared, and therefore, for their stability in long-term operation under harsh HER conditions to be predicted. As can be seen, the HER started to occur at –0.8 V on the ATTM-derived Mo–O–S film (Fig. 3.7 A), while the thiourea-molybdate-based film demonstrated slow but constant current growth starting from less negative potentials (Fig. 3.7 B).

A Tafel analysis of the polarization curves of the Mo–O–S films prepared from the thiourea-molybdate precursors was carried out. The Tafel slopes in the range of $\eta = 0.1$ V were found to be 91 mV and 85 mV for the films polarized before and after electrolysis at 5 mA/cm^2, respectively. These values corresponded well to those obtained for ATTM-based MoS_3 samples, which exhibited a Tafel slope of 86 mV at pH 7 polarization conditions [116]. In addition, it was noticed that the Tafel slope of the film was lower after 5 mA/cm^2 HER operation. This result might not be a coincidence. Hu's group concluded that ATTM-based films undergo reductive activation during the HER, and all the different amorphous phases of the prepared films are transformed to the active catalytic species, MoS_{2+x} [99].

In general, when evaluating the data of films polarization (Figure 3.7), both catalysts showed relatively low HER catalytic activity in a pH 7 solution, as a current density of 1 mA/cm^2 was reached at overpotentials ≥ 300 mV. Furthermore, both the Mo–O–S films had a tendency to lose activity after electrolysis at 5 mA/cm^2, indicating the need for further modification of the films.

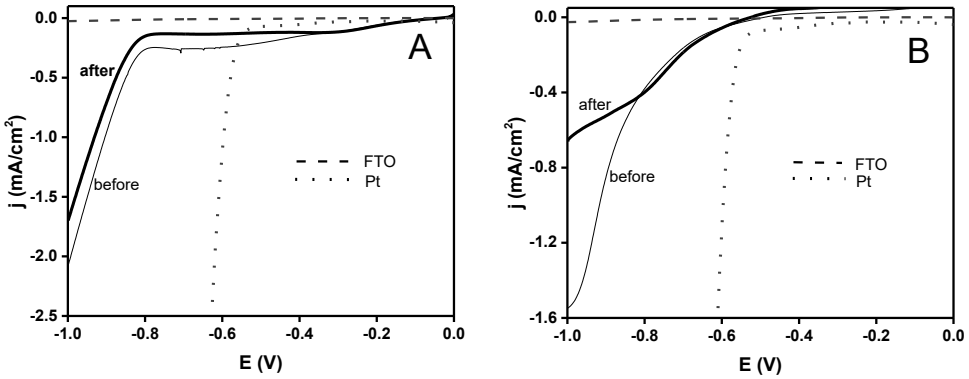

Fig. 3.7. Polarization curves of the FTO/Mo–O–S electrodes in a 1.0 M phosphate buffer solution (pH 7) at a scan rate of 5 mV/s before and after 5 mA/cm^2 cathodic electrolysis. The Mo–O–S films were prepared from (A) ATTM in $NaClO_4$ and (B) thiourea and ammonium molybdate solutions

3.1.3. Synthesis of Co–Mo–O–S films

When the methodology proved to be successful for both Co–O–S and Mo–O–S films deposition, precursors were combined to design S-containing Co–Mo–O films. The trio of Co, Mo and S, as combined together, should create a link between reactivity and stability desired for HER [109]. The properties control for this set of precursors may be the greatest challenge.

Thus, deposition on FTO substrate was initially performed from $CoCl_2$ and ATTM, as Co, Mo and S donors, respectivelly. In a typical procedure, the solution of 0.0017 M $CoCl_2$, 0.005 M ATTM and 0.1 M $NaClO_4$ was prepared to fill the deposition bath. 20 CV deposition was adapted for the synthesis of Co–Mo–O–S film according to Mo–O–S film preparation from ATTM (Fig. 3.5 A). The potential was cycled between 0.2 V and –1.2 V, identically to both the Co–O–S and Mo–O–S films depositions. As can be seen in Figure 3.8 A, CVs of film electrodeposition fit better to the FTO behavior in the ATTM bath (Figure 3.5 A) rather than in $CoCl_2$ + TU bath (Figure 3.1). These results correspond well with the studies of electrochemical Co promotion effect on amorphous MoS_3 films [116]. The solution chemistry can be followed from these studies. It can be suggested, that aqueous $(NH_4)_2[Co(MoS_4)_2]$ complex is formed *in situ* upon mixing $(NH_4)_2[MoS_4]$ and $CoCl_2$. This complex serves as a molecular precursor for Co–Mo–O–S film, as described in the electropolymerization procedure [116]. In particular, two peaks occurred at –0.1 V and –0.9 V, which correlate with the previously described mechanism of molybdenum sulfide film formation from MoS_4^{2-} via equations (3.12) – (3.14). It can be seen that the process is additionally accelerated, as deposition currents are higher for the Co–Mo–O–S rather than Mo–O–S. This can be explained by the effect of Co promotion on Mo–O–S formed beforehand. The hypothesis is that cobalt might bind to unsaturated S sites of amorphous Mo-S and, therefore, increase the conductivity of the deposits.

However, one of the major drawbacks was identified when Co–Mo–O–S was synthesized from Co^{2+} and an ATTM mixture. Even though intense dark and homogenous film on FTO substrate was obtained as a result of 20 CV deposition, the precipitation of intermediates from the volume of solution was more than obvious during the entire synthesis. This effect was also detected by Hu and coworkers [116]. It was identified that precipitation is inevitable when the concentrations ratio of $CoCl_2$ to $(NH_4)_2[MoS_4]$ exceed 1 : 2, respectively. However, the optimal ratio (for operating in HER) of Co to Mo in the deposition bath is supposed to be 1:3. This ratio was used for the Co–Mo–O–S film synthesis in this work, but precipitation still occured. It clearly leads to the outcome that the precise starting point of precipitation is hardly controlable for aqueous solutions. This finally confirmed an assumption to find alternative precursors to source Mo and S in aqueous electrodeposition.

Amonium molybdate was then combined with thiourea and $CoCl_2$, as separate Mo, S and Co precursors, respectively. Synthesis of Co–Mo–O–S was based on thiourea-molybdate-based Mo–O–S film deposition during 3 CV potential cycling procedure. Typical deposition voltammograms are presented in figure 3.8 B.

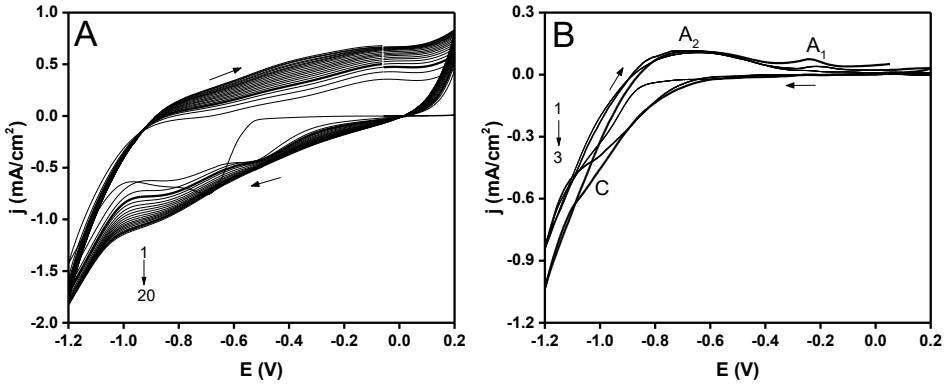

Fig. 3.8. Characteristic cyclic voltammograms of Co–Mo–O–S deposition on FTO. (A) 20 sweep-cycles in electrolysis bath containing 0.0017 M $CoCl_2$, 0.005 M ATTM and 0.1 M $NaClO_4$ and (B) 3 sweep-cycles in an electrolysis bath containing 0.005 M $CoCl_2$, 0.005 M ammonium molybdate and 0.5 M thiourea

Similarly to the Mo–O–S film deposition previously presented in figure 3.5 B, CVs plotted in figure 3.8 B do not have characteristic redox peaks that are related to film formation from an aqueous MoS_4^{2-} solution. It is therefore suggested that the mechanism for this Co–Mo–O–S film deposition initially includes Co–O and Mo–O species (co)deposition during the increase in cathodic current at potentials more negative than –0.6 V. The hysteresis loop, occurred from –1.1 V, is likely related to the nucleation and growth of insoluble deposits, as was identified in the case of the Co-based system. When the potential was reversed towards the positive E direction, anodic peak (A_2) of TU electro-adsorption on negativelly charged Mo-O surface occurred at –0.7 V. One more anodic peak (A_1) was identified at –0.2V. Consequently, a hypothesis was made that A_1 is induced by TU electro-oxidation to FD, as TU was beforehand attracted by Co-TU complex on Co–O species. These observations suggest that Co-O-S and Mo-O-S, when deposited in tandem, may overcome the full

anodic path of TU electro-adsorption (A_2) and oxidation (A_1) with the enhanced possibility of S incorporation into the Co-Mo-O-S film. Additionally, it was identified that the appearance of small cathodic shoulder (C) at –1.0 V, which can potentially be identified as the film's ability to desorb TU/FD lattice residues from the electrode after donoring S to Co–Mo–O–S.

Figure 3.9 shows the characteristic chronopotentiograms of Co–Mo–O–S films catalyzing HER in a pH 7 buffer solution. In comparison to Mo–O–S films (Fig. 3.6), Co–Mo–O–S electrodes are able to sustain the same 5 mA/cm^2 conditions but with lower overpotentials. In contrast, Co–O–S samples degraded immediately after the first moments of H_2 bubbling in a neutral buffer solution without adequate comparison to other samples. In this case, polarization curves of Co–O–S films (Fig. 3.4) can not represent the stable catalytic materials. Enhanced catalytic behaviour was observed for Co–Mo–O–S film (A in Fig. 3.9) prepared from a Co–ATTM based solution: relatively low overpotential with only 40mV shift was sustained after 1h of intense electrolysis. Activation-induced development was observed for the ATTM-free alternative Co–Mo–O–S electrode (B in Fig. 3.9), as the potential moved from –1.46 V until it became stable at –1.24 V after 20 min of electrolysis. This value was maintained and only 40 mV was detected as a difference in overpotentials between A and B electrodes.

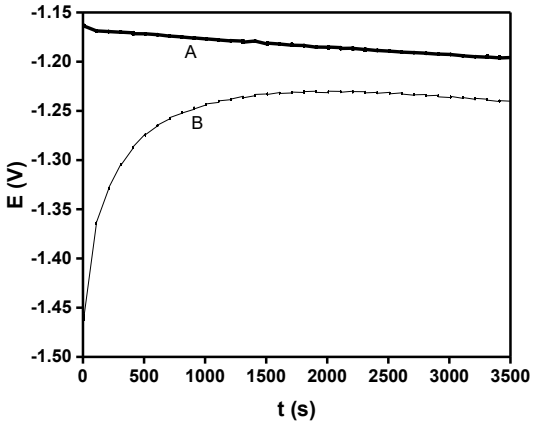

Fig. 3.9. Characteristic chronopotentiograms recorded in a pH 7 phosphate buffer solution at a constant applied cathodic current density of 5 mA/cm^2 for the Co–Mo–O–S films prepared from (A) $CoCl_2$, ATTM and $NaClO_4$ and (B) $CoCl_2$, ammonium molybdate and thiourea solutions

Linear sweep voltammetry was employed to evaluate the catalytic behaviour of the prepared Co–Mo–O–S films before and after being used for electrolysis at 5 mA/cm^2 for 1h. It can be seen that the Co–ATTM based catalyst (Fig. 3.10 A) has a similar profile to the ATTM-based Mo–O–S film, as HER currents started to occur from –0.8 V in both cases and 1 mA/cm^2 was reached at 300 mV overpotential. In addition, ATTM-derived film had a tendency to lose activity after operating in HER. Contrary results were obtained for our alternative Co–Mo–O–S catalyst. Even though low-rate HER was performed before 5 mA/cm^2 electrolysis, the catalyst showed

enhanced activity after the chronopotentiometry test without any signs of film degradation. This encouraged to further explore this novel Co–Mo–O–S film as a HER catalyst in pH 7 solution with the intention to reduce overpotential, increase stability and eliminate film degradation processes.

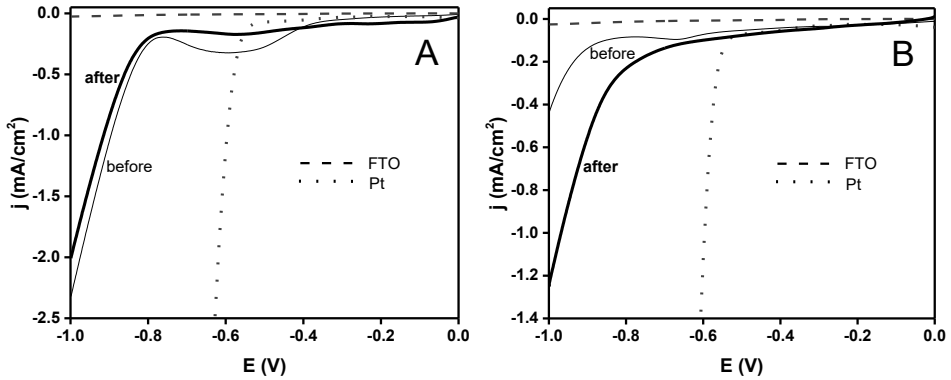

Fig. 3.10. Polarization curves of FTO/Co–Mo–O–S electrodes in phosphate buffer solution (pH 7) at a scan rate of 5 mV/s before and after 5 mA/cm^2 electrolysis. The Co–Mo–O–S films prepared from (A) $CoCl_2$, ATTM and $NaClO_4$ solutions and (B) $CoCl_2$, ammonium molybdate and thiourea

3.2. Structural characterization of Co–O–S, Mo–O–S, Co–Mo–O–S films

After extensive discussions, ATTM-derived films were dropped and only the films based on alternative Mo and S precursors were studied further. The structure of Co–O–S films were investigated in parallel in order to compare the influence of cobalt behaviour in the samples. In addition, Co–O–S films and molybdate-thiourea based Mo–O–S and Co–Mo–O–S samples were annealed, and subsequently evaluated by structural analysis techniques. It is known that thermal treatment can reduce "defects" in film composition, and may affect their overall catalytic activity.

Figure 3.11 illustrates the X-ray diffraction patterns recorded for the as-prepared (Fig. 3.11 A) and annealed (Fig. 3.11 B) Co–O–S, Mo–O–S and Co–Mo–O–S films that were electrodeposited on an FTO substrate by the three sweep cycles. The absence of characteristic diffraction peaks for crystalline cobalt or molybdenum oxides or sulfides suggested the existence of the amorphous phase or the lack of long-range crystalline order in the as-deposited films. Due to the poor crystallinity, only clearly defined SnO_2 (PDF 46–1088) peaks originating from the FTO substrate were detected (Fig. 3.11 A). In contrast, additional peaks were observed in the XRD pattern of the annealed Mo–O–S films, indicating a higher crystallinity than the as-deposited Mo–O–S samples. Analysis of the diffraction pattern led to the conclusion that the annealed film was composed predominantly of the α-MoO_3 phase (PDF 47-1320). In this regard, a variety of Mo oxide species are known to be present in the molybdenum oxides films, exhibiting diverse molecular structures such as Mo_8O_{26}, Mo_7O_{24}, or MoO_4 [131]. In addition to the peaks attributed to the Mo oxide species, diffraction signals, characteristic to the small amount of the molybdenum sulfide phase, are also present in the XRD pattern [124, 125]. It can be concluded, that annealing improved the crystallinity only for the as-deposited Mo–O–S samples. The halo around

2Θ = 10° was reduced for the Co–O–S sample, however the absence of characteristic diffraction peaks for crystalline cobalt phases corresponds to the *operando* studies [88] and suggests the existence of an amorphous nature of both as-prepared and annealed films. In the case of the novel Co–Mo–O–S films, amorphous structures were recorded before and after thermal treatment.

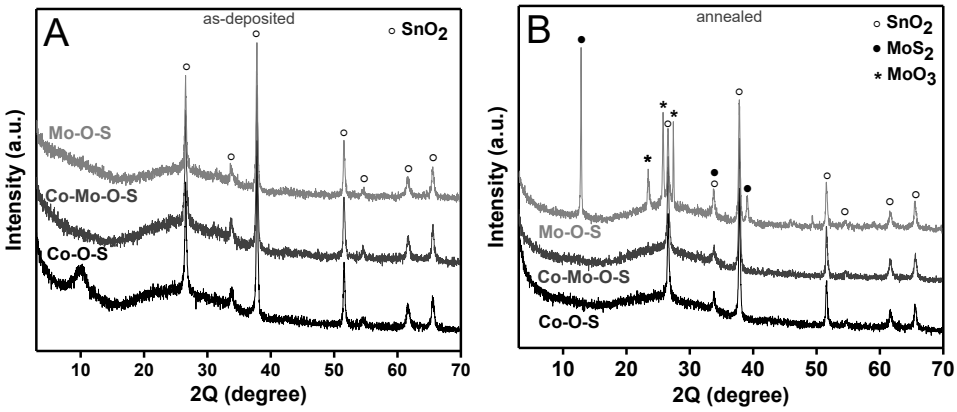

Fig. 3.11. X-ray diffraction patterns of the as-deposited (A) and annealed (B) films on FTO substrates

The FT–IR spectra of the as-prepared (Fig. 3.12 A) and annealed (Fig. 3.12 B) films are shown in Figure 3.12. Similar to the results of crystalographic analysis, the effect of thermal treatment was mostly noticeable for Mo–O–S samples. The absorption peaks at wavenumbers ca. 3400 cm^{-1} and 1630 cm^{-1} can be observed for all samples and correspond to O–H stretching and bending vibrations, respectively. Although sulfur was barely observed in the crystallographic analysis, the IR spectra confirmed the presence of S bonds in the samples. The vibrations of the S–O bond can be seen at ca. 1000 cm^{-1}. The precise characterization of data relating to cobalt-containing samples is not practical, since the characteristic peaks are not sufficiently distinct, even after annealing. Contrary, the effect of thermal treatment is more noticeable for Mo–O–S samples. Electrodeposition using aqueous electrolytes usually leads to the formation of various oxo-intermediates. In this case, a series of absorption peaks at 1400, 880, and 740 cm^{-1} in the as-deposited Mo–O–S films were assigned to various Mo–O bond vibrations [132]. The intensity of the latter peaks was significantly increased in the annealed sample. In addition, an absorption peak shoulder at around 480 cm^{-1} could be related to Mo–S stretching vibrations. The IR data suggested that the formation of the inorganic films was successful, as the characteristic peaks of the thiourea functional groups [133] were absent in all the prepared samples.

Raman spectroscopy can present additional information concerning the inorganic nature of films structure. Unfortunately, only annealed Mo–O–S film showed results worth discussing with the corresponding Raman spectra is presented in Figure 3.13 A. SEM micrograph of the annealed Mo–O–S sample is also presented (Fig. 3.13 B). It should be noted that after annealing, the relatively smooth surface of

the as-deposited Mo–O–S film (will be presented later) with hard to identify Raman vibrations turned into the more expressed morphology based on randomly oriented blocks (Fig. 3.13 B).

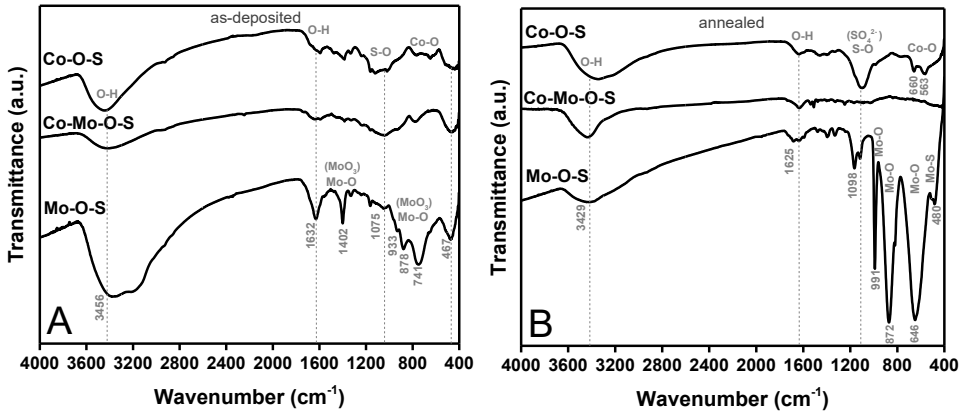

Fig. 3.12. Characteristic FT-IR spectra of the as-deposited (A) and annealed (B) samples

As can be observed in the Raman spectra of the annealed film, the appearance of strong bands in the 800–1000 cm^{-1} region reflected the presence of the MoO_3 phase [134]. The Raman band at 994 cm^{-1} was associated with the symmetric stretching of the Mo=O bond. The band at 820 cm^{-1} was attributed to the asymmetric vibrations of the bridging Mo–O–Mo bonds, and the associated Mo–O–Mo bending mode was observed at ca. 150 cm^{-1} [134]. In most Raman spectroscopic studies of bulk MoS_2 samples, the active S–Mo–S modes are usually observed at 286, 383, and 408 cm^{-1} [135]. In this research case, the observed Raman bands in the 250–400 cm^{-1} region could be partially related to the presence of Mo–S bonds. However, the applied analytical techniques did not unambiguously permit the identification of the exact structure and composition of the prepared films, as the signals associated with the Mo–O and Mo–S bonds can overlap.

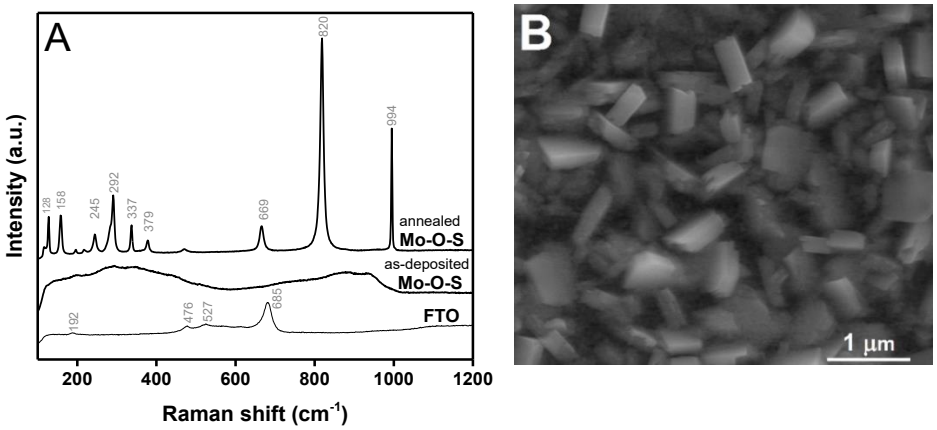

Fig. 3.13. Raman spectra (A) and SEM image at ×50 000 magnification (B) of the annealed Mo–O–S film on FTO substrate

Energy dispersive X-ray spectroscopy (EDX) was further employed to confirm the presence of Co, Mo and S in the prepared films. The EDX spectra of annealed samples is presented in Figure 3.14. The high surface heterogeneity of the obtained films was detected as, for example, atomic ratio of Mo:S varied between 0.35:2 depending on the point under EDX investigation. However, these variations can also be related to relatively small amounts of elements (S, Mo < 5 at. %, Co 10-20 at. %) detected in the films by EDX. A high oxygen content (70-80 at. %), detected in all the prepared samples, can be associated with the following sources: the presence of silica and tin oxides in the FTO substrate; the electrodeposition of cobalt and molybdenum oxide/hydroxide films according to the electrochemical deposition mechanism described earlier; and the inevitable films surface oxidation by air oxygen. According to these reasons and the inevitable presence of oxygen, all prepared samples were named S-containing oxide films and denoted as Co–O–S, Mo–O–S, and Co–Mo–O–S.

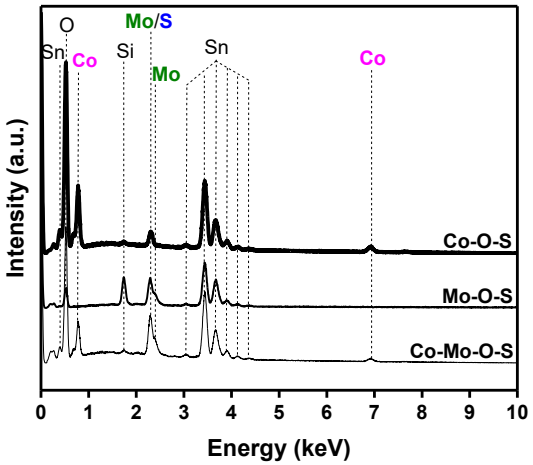

Fig. 3.14. EDX spectra of the annealed Co–O–S, Mo–O–S, Co–Mo–O–S films

It was reviewed that metal chalcogenides, such as cobalt sulfides, have potential applications in photoinduced systems (Table 1.4). The UV-Vis diffuse reflectance and absorbance spectroscopy confirmed that the optical behaviour of the films is dependent on the preparation conditions (Fig. 3.15). The most stable optical properties remained for the Co-Mo-O-S film. On the other hand, these films exhibited the lowest light absorption characteristics when compared to other samples. In the case of Co-O-S films, annealed samples showed improved absorption and reduced reflectance in the visible light range. However, the main changes in optical properties were induced by thermal treatment for Mo-O-S samples. As can be seen, the light absorption was reduced and reflectance was increased considerably in parallel with the visual changes in the films appearance: the as-deposited brownish film became white in colour after annealing. In contrast, Co-O-S and Co-Mo-O-S films did not undergo similar structural changes.

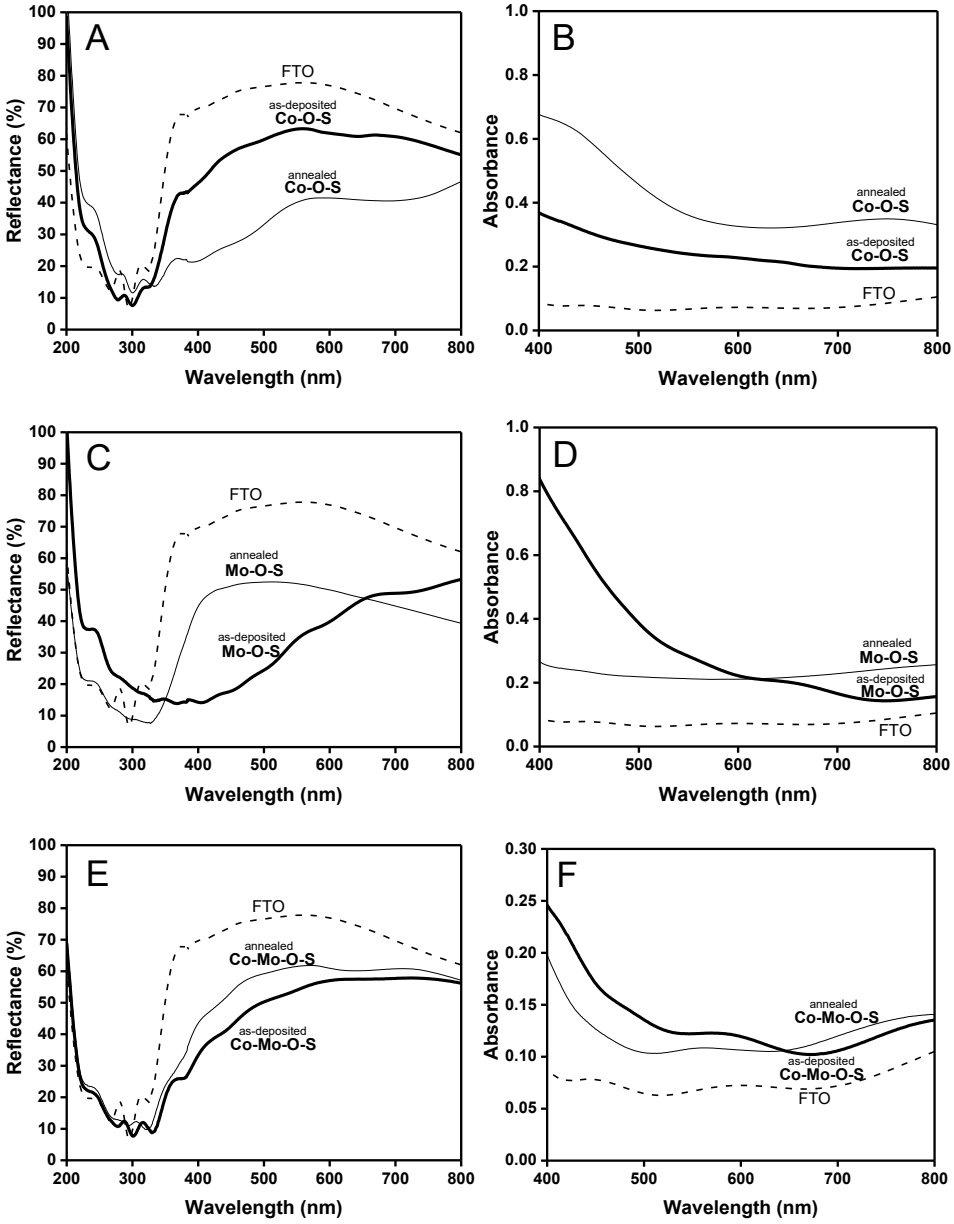

Fig. 3.15. UV-Vis reflection and absorbance spectra of the Co–O–S (A, B), Mo–O–S (C, D), Co–Mo–O–S (E, F) films on FTO substrate

As reported above, annealing improved the crystallinity of some as-deposited films. However, it had a detrimental effect on their electrocatalytic activity in the HER (Fig. 3.16). For this reason, only the experimental data for the as-deposited films is included in the following studies.

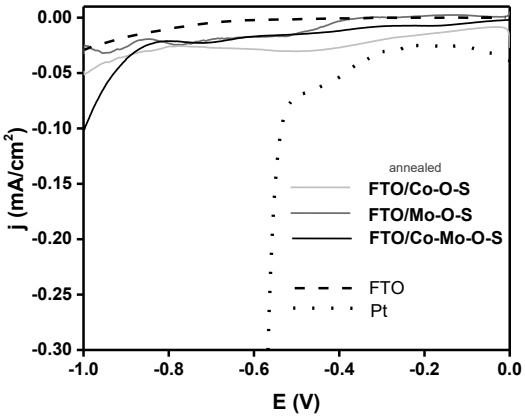

Fig. 3.16. Polarization curves of the annealed Co–O–S, Mo–O–S, Co–Mo–O–S films in phosphate buffer solution (pH 7) at a scan rate of 5 mV/s

SEM micrographs revealed the surface morphology of the as-prepared Co–O–S, Mo–O–S, and Co–Mo–O–S films (Fig. 3.17). As previously presented in Section 3.1.1, the multi-layer porous surfaces with folds and honeycomb-like structure can be identified for Co–O–S films (Fig. 3. 17 a-b). The surface of Mo–O–S is relatively smooth, with small nodules and cracks (Fig. 3. 17 c-d). In this case, the presence of the cracks can be attributed to the generation of high internal stress during the drying-induced shrinkage [136]. The hypothesis of correlation between morphology and catalytic behaviour of Co–O–S and Mo–O–S films can be considered according to the obtained results. The more porous structure of Co–O–S film may provide a larger surface area and, thus, increased activity properties in HER. In contrast, Mo–O–S do not contain holes and its structure is more compact; these can be the factors for increased stability characteristics of the film. The Co–Mo–O–S surface contains the combined properties of both Co and Mo films structures. It can be seen that the nodules-based layer of the film contains irregularly formed holes and individually raised spherical particles (Fig. 3. 17 e-f). It can be assumed that the Co–Mo–O–S structure, when coupled with the catalytic behaviour of these samples, is likely to demonstrate the synergetic effect for the HER. Next to the composite Co–Mo–O–S structure, H_2 can be more efficiently evolved via the combination of Co–O–S activity properties and Mo–O–S stability features.

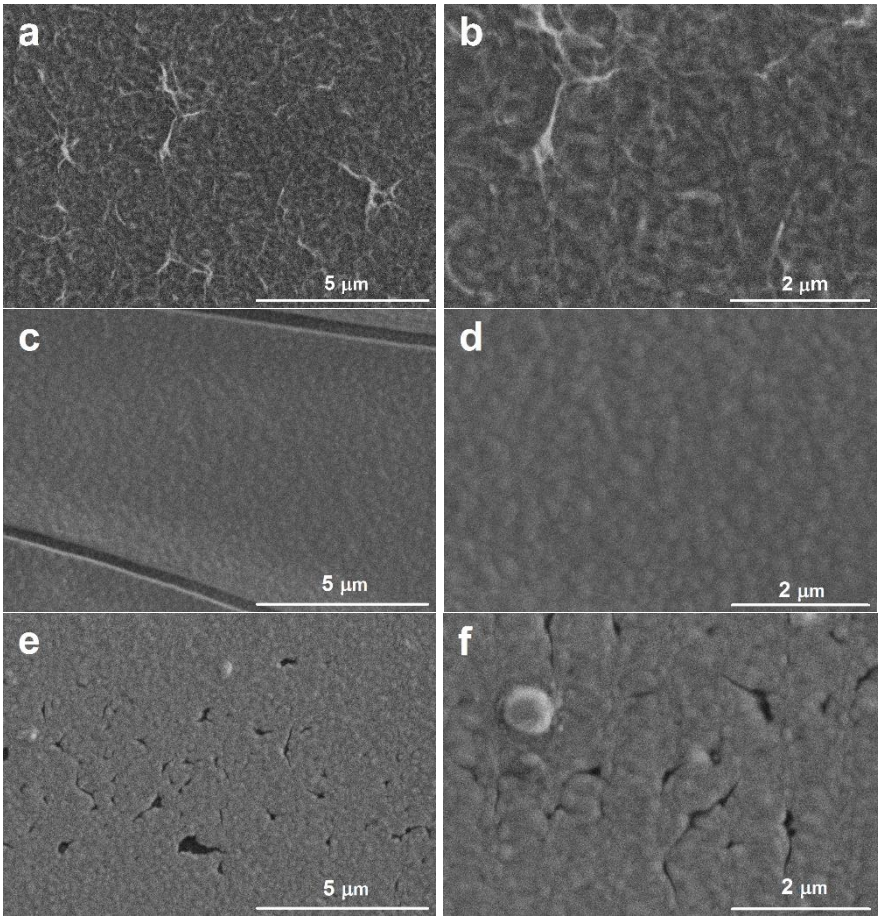

Fig. 3.17. SEM images of the Co–O–S (a–b), Mo–O–S (c–d) and Co–Mo–O–S (e–f) films on FTO prepared by 3 deposition CV cycles. Magnifications ×10 000 and ×20 000 for 5 μm and 2 μm, respectively

3.3. Optimization of Co–Mo–O–S synthesis conditions

Since the combination of individual Co, Mo and S precursors showed successful results for Co–Mo–O–S film formation, it became necessary to optimize the synthesis conditions. For this purpose the effects of the initial Co/Mo ratio, pH of the deposition bath, and catalysts loading were the subject of deeper investigation.

3.3.1. Effect of Co/Mo ratio

In order to identify the effect of the Co to Mo ratio and distinct precursors concentration for the resulted Co–Mo–O–S catalysts, the films were prepared using several compositions of precursors bath. Initially, the Co–Mo–O–S film was prepared from a 0.5 M thiourea solution containing 0.005 M $CoCl_2$ and 0.005 M $(NH_4)_6Mo_7O_{24}$ with Co:Mo ratio being 1:1, as described in Section 3.1.3. The concentration of $CoCl_2$ was decided to be greatly raised, as the cobalt-based component of the catalyst was previously associated with the activity of the film. Co:Mo ratio was changed to 4:1 with a purpose to provoke a noticeable changed concentration effect. The pH of the deposition bath slightly decreased from 8 (Co:Mo 1:1) to 7.8 (Co:Mo 4:1). In contrast, the $(NH_4)_6Mo_7O_{24}$ solution is alkaline in nature and might significantly increase the pH of the deposition bath. This effect is unfavourable for pH neutral deposition bath conditions and, thus, the concentration of Mo was not raised separately.

The characteristic voltammograms of 3 CV Co-Mo-O-S film deposition from a solution with Co:Mo ratio being 4:1 are presented in Figure 3.18 A. The behaviour of the electrode in a 4:1 ratio bath shows a relation with the primary mechanism identified for Co–Mo–O–S film deposition. Specifically, Co–O and Mo–O species (co)deposition (*C*) is followed by TU electro-adsorption on negativelly charged Mo-O surface (A_2) and TU electro-oxidation to FD from Co-TU complex (A_1), as discussed previously. It was observed that the increased concentration of $CoCl_2$ induced the growth of the peak A_1.

Linear sweep voltammetry, recorded for the electrode before and after being used for electrolysis at 5 mA/cm^2 for 1h, show a reduced catalytic activity in HER after an intense 1h electrolysis (Fig. 3.18 B). In addition, there are no signs of enhanced catalytic activity of Co:Mo 4:1 film when compared with the original Co:Mo 1:1 sample. It should also be noted, that an intense peak at –0.7 V was identified for the Co:Mo 4:1 sample during electrode polarization in the pH 7 buffer

solution. This peak was previously linked to the Co-O-S film behaviour in HER and is likely related to the film degradation process (Fig. 3.4).

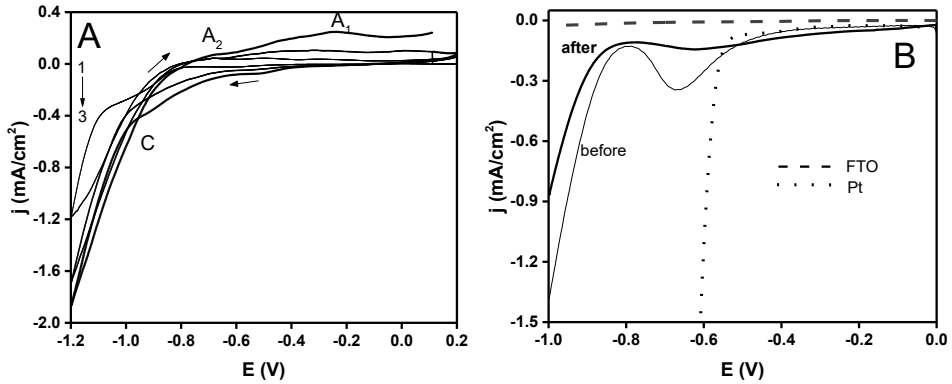

Fig. 3.18. Co–Mo–O–S deposition on FTO fabricated using 3 sweep-cycles in electrolysis bath containing 0.02 M $CoCl_2$, 0.005 M ammonium molybdate and 0.5 M thiourea (A) and electrode behaviour in 1.0 M phosphate buffer solution (pH 7) before and after 5 mA/cm^2 electrolysis (B)

When the ratio of Co:Mo was fixed to 1:1, the initial concentrations of 0.005 M were increased five times for both precursors. This change could induce an even more expressed influence of both Co and Mo metals and their amounts in the electrolysis bath. The deposition bath of 0.5 M thiourea solution containing 0.025 M $CoCl_2$ and 0.025 M $(NH_4)_6Mo_7O_{24}$ was prepared for 3 CV film deposition (Fig. 3.19 A). The mechanism of film formation is more or less identical to the original synthesis path from lower precursor's concentrations. Unfortunately, the catalytic activity in the pH 7 phosphate buffer solution was identified to be decreased with increasing the amount of precursors (Fig. 3.19 B).

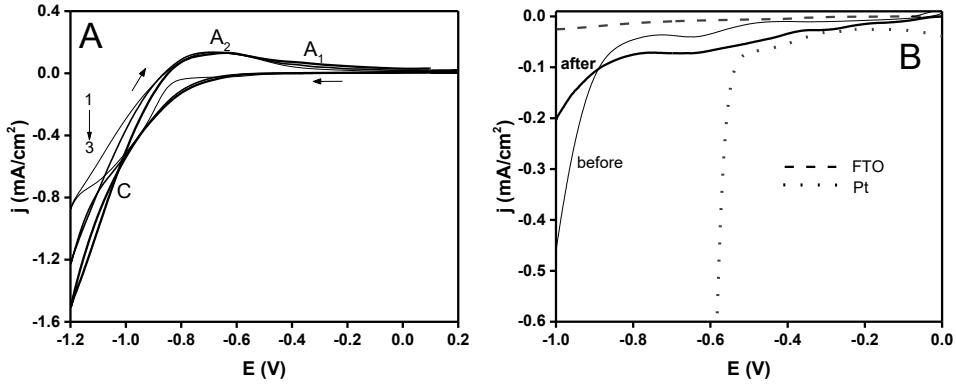

Fig. 3.19. Co–Mo–O–S deposition on FTO fabricated using 3 sweep-cycles in electrolysis bath containing 0.025 M $CoCl_2$, 0.025 M ammonium molybdate and 0.5 M thiourea (A) and electrode behaviour in 1.0 M phosphate buffer solution (pH 7) before and after 5 mA/cm^2 electrolysis (B)

It is interesting to note that the performance of the deposited films was observed to be highly dependent on the concentrations of precursors while keeping the same Co:Mo ratio (1:1). Figure 3.20 represents the catalytic performance of the prepared

Co–Mo–O–S films in a pH 7 intense hydrogen evolution reaction. It can be seen, that the films prepared from initial concentrations of 0.005 M $CoCl_2$ and 0.005M $(NH_4)_6Mo_7O_{24}$ demonstrate the best activity and stability characteristics when compared to other samples. The electrode activation and potential development was observed only for the films with Co:Mo ratio of 1:1 (Fig. 3.20 A and C), while the film with the raised Co concentration (Fig. 3.20 B) showed a slow but constant increase in overpotentials. The obtained results lead to the perception that it is not practical to change the initial Co/Mo ratio in order to improve catalytic performance of the Co–Mo–O–S films. Apparently, the lower deposition rate may lead to the more ordered film structure suitable for HER.

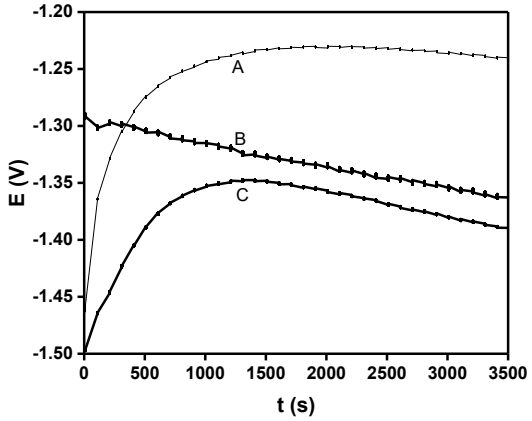

Fig. 3.20. Characteristic chronopotentiograms recorded in pH 7 phosphate buffer solution at constant applied cathodic current density of 5 mA/cm^2 on Co–Mo–O–S films prepared by adjusting Co/Mo concentrations in the depostion bath: 0.005 M/0.005 M (A), 0.02 M/0.005 M (B) and 0.025 M/ 0.025 M (C), respectively

3.3.2. Effect of pH

In order to determine the effect of pH for the deposition bath, hydrochloric acid was used to adjust the pH values starting from the initial up to pH 3. This range of pHs was experimentally identified to be convenient and suitable in order to detect the changes and regularities during films formation. Figure 3.21 shows the changes in the 3 CV deposition mechanisms in a context of characteristic peaks A_2, A_1, and C.

When sweeping negatively from the initial potential of about 0.1 V, the cathodic process, associated with Co–O and Mo–O species deposition, is accelerated in all first cycles during the decrease in pH. An opposite tendency was observed for the anodic peak (A_2) in the reverse sweep where the TU electro-adsorption related processes were suggested to be constant until a pH of 3 and the intense decrease in pH caused a current drop and A_2 reduction. The major effect of pH is recorded for anodic peak A_1, which is linked to thiourea electro-oxidation to FD compounds on the electrode surface. It can be observed, that every pH adjusting step induces the growth of peak A_1. The heights of A_2 and A_1 become equal at pH 5.8 and A_1 is further increased with the subsequent pH adjustment. It can be assumed that this behaviour might be related with the prevailing Co deposition and the enhanced formation of Co–TU complexes. Finally, small shifts of cathodic shoulders (C) were recorded during repetitive

potential cycling as identification of TU/FD lattice desorption from the electrode surface after donoring S to Co–Mo–O–S structures.

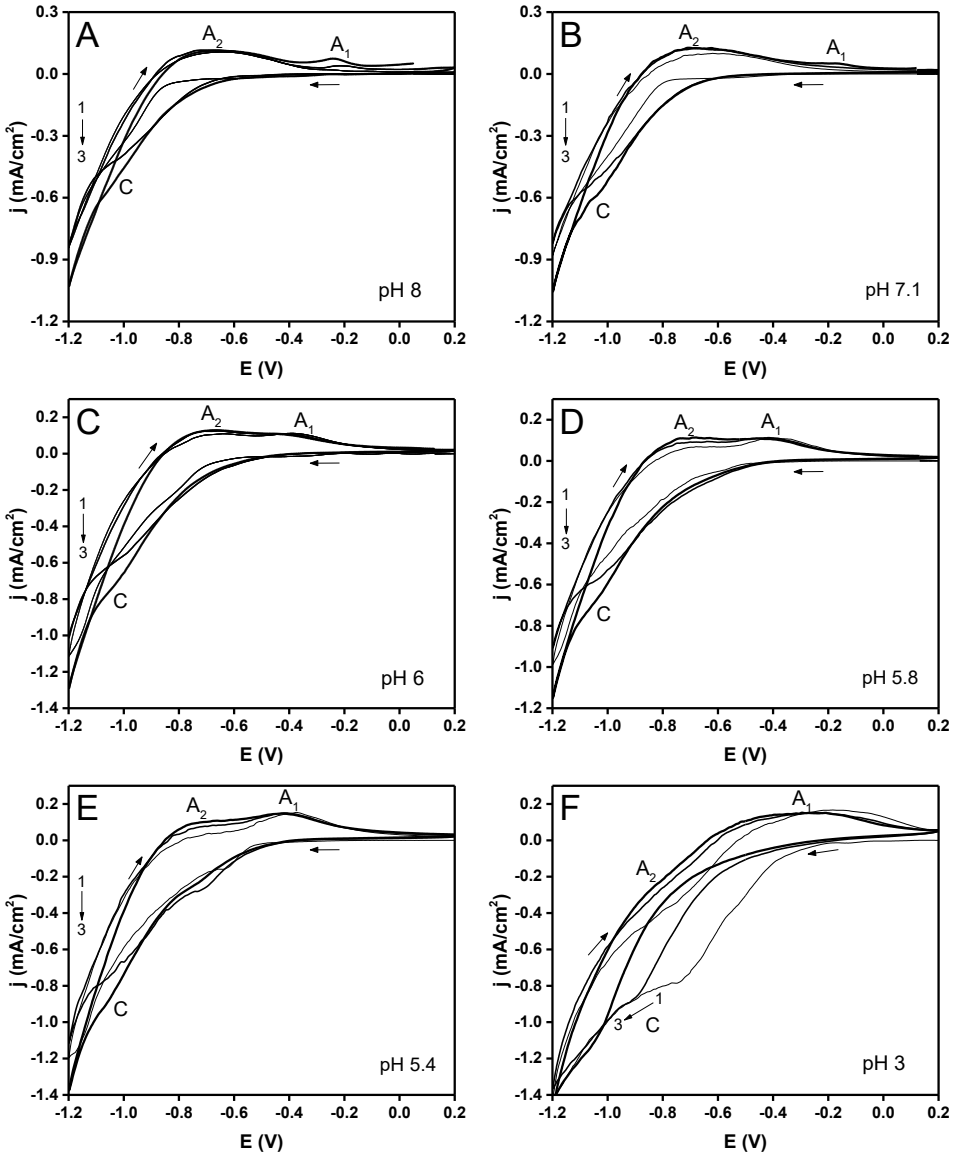

Fig. 3.21. Co–Mo–O–S deposition on FTO fabricated using 3 sweep-cycles in initial (A) and pH adjusted (B-F) electrolysis bath containing 0.005 M $CoCl_2$, 0.005 M ammonium molybdate and 0.5 M thiourea at a scan rate 5mV/s

The effect of pH was then evaluated in a context of surface morphology. A series of SEM images and corresponding AFM data is presented in Figure 3.22. It is observed that all pH adjusted films exhibit well-adhered surface morphology (Fig. 3.22. a-d). The fine adhesion of the electrodeposited films might be an essential aspect in defining the electrochemical stability towards the HER applications [119].

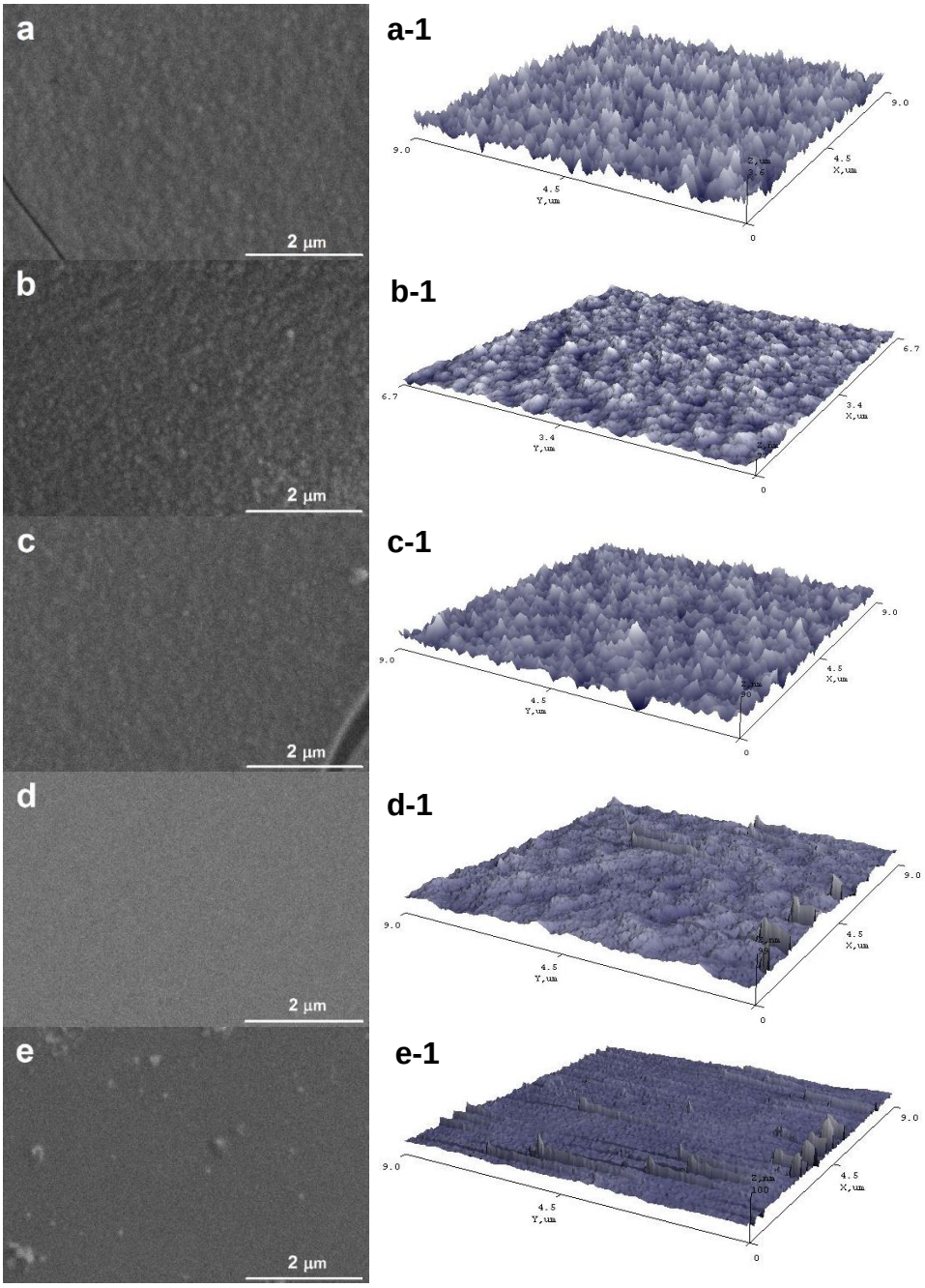

Fig. 3.22. SEM images (a–e) and AFM data (a-1–e-1) of Co–Mo–O–S on FTO deposited with 3 deposition CV cycles at various pHs: (a, a-1) – 7.1, (b, b-1) – 6, (c, c-1) – 5.8, (d, d-1) – 5.4, (e, e-1) – 3

A tightly packed layer of nodules can be observed for the films prepared at pHs 7.1–5.8 (Fig. 3.22. a-c). The well connected surface morphology with tightly packed nanocrystals is able to promote the effective electron transport from their surface to the redox electrolyte [137]. The samples deposited at higher pH values demonstrate more dense film architectures (Fig. 3.22. d-e). The surface topography 3D images complement the obtained results and are presented at Figure 3.22. a-1–e-1.

In relation with surface morphology, several physical characteristics were measured for Co–Mo–O–S films. The corresponding data of films thickness and surface roughness are presented in Table 3.1 and plotted as ordinates in graphical data of Figure 3.23 A and B. Additionally, the weight of the prepared and dried catalysts was used to determine the catalysts loading and the data was also ploted versus pH (Fig. 3.23 C). Finally, the freshly prepared films were subjected to AAS analysis. The Mo content was determined and used to plot as Mo loading in $1cm^2$ of the film (Fig. 3.23 D). Discounting the numbers, the breaking point is obvious in every pH-characteristic graph. It can be observed that Co–Mo–O–S samples prepared at pH 6 deposition bath demonstrate the limiting values of the corresponding characteristics.

An even more pronounced pH effect can be observed in a context of the Co:Mo ratio probed using EDX and XPS analysis. As shown in Table 3.1, the Co:Mo ratios determined from EDS data are only slightly different from those from the more precise XPS analysis technique, both indicating the successful incorporation of Co and Mo in the films. In tandem with the previously detected breaking point for pH 6 film, this sample showed a distinctive composition of a Co:Mo ratio of ~ 1:1. Above this, Co–Mo–O–S films prepared in the initial and pH 7.1 adjusted electrolysis baths showed the tendency of enhanced Co deposition and the Co:Mo ratios were calculated to be < 1. On the other hand, all the other Co–Mo–O–S films prepared in pH < 6 adjusted baths were detected to contain an increased amount of Mo with the Co:Mo ratios being >1. These observations correspond well with the results presented in Figure 3.23, thus pH 6 can also be identified as the breaking point of pHs for Co:Mo ratios.

Table 3.1. Characteristics of Co–Mo–O–S films prepared using 3 sweep-cycles in initial (pH 8) and pH adjusted (pH 3–7.1) electrolysis baths

Film No.	pH of deposition bath	Thickness (nm), ± *25 nm*	Surface roughness (nm), R_a	Co:Mo ratio (EDX)	Co:Mo ratio (XPS)
1	8.0	197	69	1 : 0.8	1 : 0.3
2	7.1	265	60	1 : 0.8	1 : 0.6
3	6.0	315	57	1 : 1.1	1 : 1
4	5.8	425	70	1 : 1.2	1 : 2.1
5	5.4	600	82	1 : 2.4	1 : 3
6	3.0	1300	112	1 : 3	1 : 4.8

The phenomenon of pH 6 can be adequately explained according to the study in a field of metallurgy [138]. pH-Controlled precipitation of cobalt and molybdenum was performed using Co–Mo aqueous solutions as industrial effluents. It was reported that pH had a substantial effect on the reaction between cobalt and molybdenum in the aqueous phase, thus affecting the amount of precipitated Co and/or Mo and the

stability of formed solid compounds. Firstly, it was experimentally observed that molybdenum had a more rapid precipitation for solution rate than cobalt. The behaviour of cobalt was reported to be based on the solid state formation and precipitation starting to occur slightly before pH 6. This rate of Co precipitation increased with increasing the pH of the solution. Meanwhile, most of Mo was precipitated from the solution into the solid phase at pH 5. With increasing pH greater than 7, the molybdenum redissolved in the solution. It became obvious that co-precipitation of Mo and Co must be performed in the pH window of 5–7. In addition, the pH value of 6 showed the balance and the possibility to form solids with the composition holding Co:Mo ratio of ~1:1. Moving away from pH 6 yields the composition with a lower amount of deposited Co or increases the risk to release Mo from the deposits. Finally, the analysis of the obtained solid phase revealed that molybdenum was chemically complexed with cobalt in the precipitate produced at the low pH, but physically adsorbed on the surface or entrapped as a liquid in the precipitates obtained at the high pH [138]. As a result, physical co-precipitation could lead to the less stable solid Co–Mo deposits.

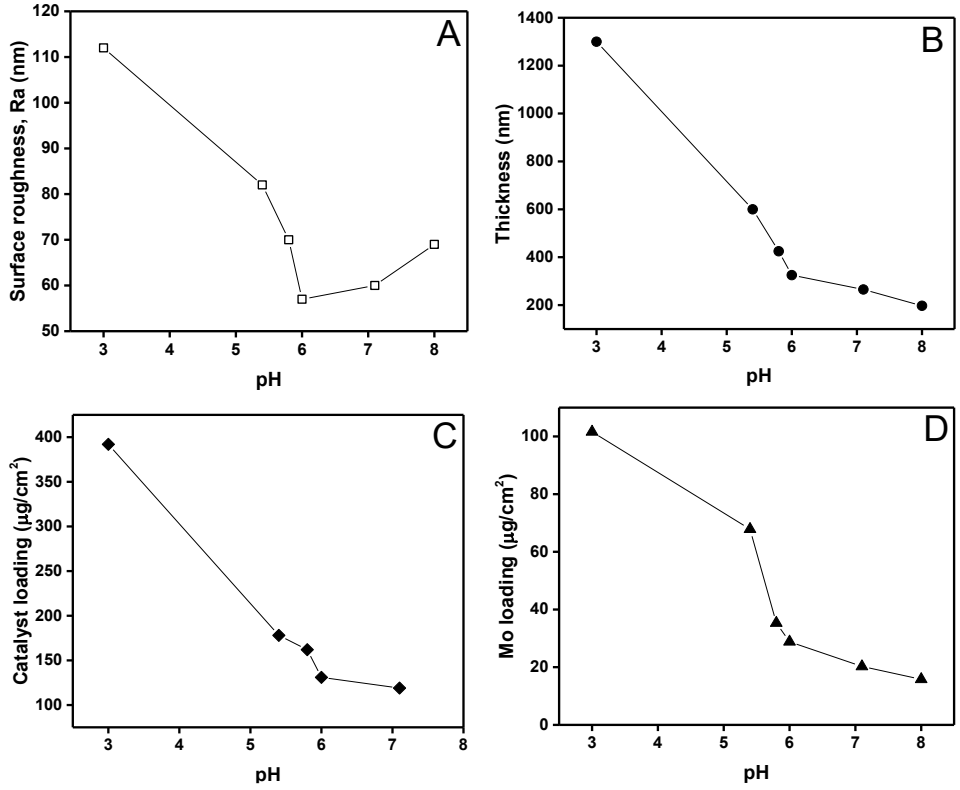

Fig. 3.23. pH influence on the surface roughness (A), film thickness (B), catalyst loading (C), and Mo atomic density in the deposited film (D). *Lines* are added for the eye guidance only

When taking into account the theoretical basis coming from the report [138] it can be concluded that the phenomenon of the breaking point identified for Co–Mo–

O–S films at pH 6 in this work is very closely related to the reported effect of balance between pH and Co:Mo co-precipitation.

Figure 3.24 shows characteristic chronopotentiograms of Co–Mo–O–S films catalyzing HER under 5 mA/cm^2 conditions. A similar E development behaviour was recorded for all samples during electrolysis. This behaviour can probably be related to the activation of the electrodes during HER. Among others, the Co–Mo–O–S film prepared at pH 5.8 deposition bath, demonstrate the stable catalytic behaviour with the lowest overpotentials. Contrary, the Co–Mo–O–S sample prepared at pH 7.1 deposition bath, exhibits relatively high potentials and catalytic activity losses under intense HER conditions. The remaining samples show a similar catalytic response when compared with the Co–Mo–O–S film prepared at initial pH 8 electrolysis bath. Exceptionally, the constant decrease of overpotentials was recorded for the pH 6 Co–Mo–O–S sample, therefore, less than 70 mV remained as a difference between pH 6 and pH 5.8 catalysts after 30 min of HER.

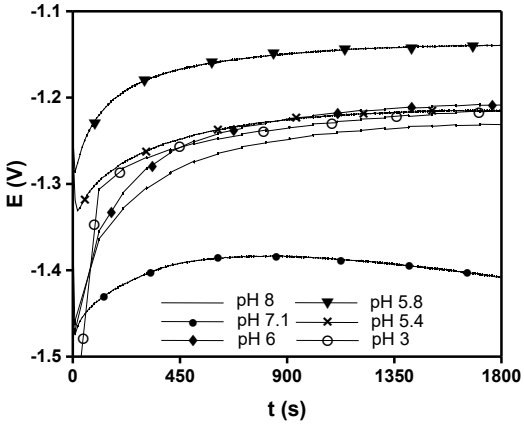

Fig. 3.24. Characteristic chronopotentiograms recorded in pH 7 phosphate buffer solution at cathodic current density of 5 mA/cm^2 on Co–Mo–O–S films prepared using 3 sweep-cycles in different pH electrolysis baths. *Custom symbols* are added for the eye guidance only

Linear sweep voltammetry was employed for Co–Mo–O–S films before and after being used for electrolysis at 5 mA/cm^2 for 1h. It can be seen in Figure 3.25 that pHs adjusting improved the catalytic performance of all samples when compared with the initial Co–Mo–O–S film before they were used at 5 mA/cm^2 electrolysis. Except for the pH 7.1 Co–Mo–O–S sample, all films showed enhanced activity properties after electrolysis. Even though 1 mA/cm^2 was reached at 280 mV or higher overpotentials, HER currents started to occur from the very beginning of the sweeps.

The development of the initial potentials during HER were presented in Figure 3.24 and the following catalytic enhancement was identified after HER in Figure 3.25. This phenomenon may be related to the electrodes activation via structure transformation during HER. It was previously disscussed in the Section 3.1.1. that amorphous Co–S structures spontaneously transform into CoS_2-like molecular clusters under cathodic polarization [88], and these CoS_x species may be the factor determining changes in the catalytic behaviour of the Co–O–S during HER. In addition, the reductive activation effects, related with a freshly prepared ATTM-based

Mo–O–S films, was also discussed in Section 3.1.2. According to the studies, all different Mo–S phases transform into the active species of MoS_{2+x} during HER [99]. This paper makes a hypothesis that similar structure activation processes might be responsible for the phenomenon of Co–Mo–O–S films catalytic activation behaviour during HER. This hypothesis can be supported by the report of Merki et al [116], where XPS analysis showed a significant change in the ATTM-based Co–MoS_3 structure after electrolysis. The resulted XPS spectrum could not be fitted undoubtedly by the researches and it was marked to have the manners of both CoS_x and MoS_{2+x} catalytically active species.

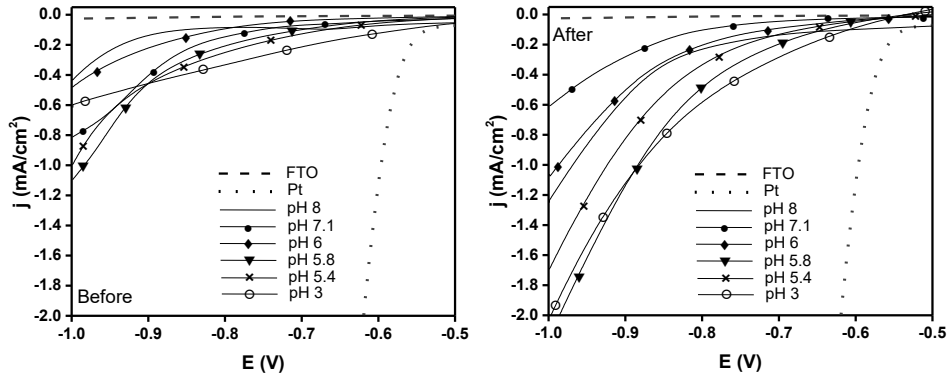

Fig. 3.25. Co–Mo–O–S film behaviour in phosphate buffer solution (pH 7) before and after 5 mA/cm^2 electrolysis. Films were fabricated using 3 sweep-cycles in initial (pH 8) and pH adjusted (pH 3–7.1) electrolysis baths. *Custom symbols* are added for the eye guidance only

The investigation of an activation process was further directed toward a set of experiments. For this purpose, the freshly prepared Co–Mo–O–S film deposited from pH 6 electrolysis bath was selected to be tested. First of all, the chronoamperometric analysis was employed to identify the potentials where the E development initially occurs (Fig. 3.26 A). The potentials from –0.7 V to –1.0 V were applied by steps to induce the corresponding current flow. The several minutes of electrolysis at constant potential showed the transition between passive and enhanced electrode behaviour. While the current responce to potentials of –0.7 V and –0.8 V was almost negligible, the potential of –0.9 V provoked an intense current growth and continuous release of H_2 bubbles. This effect was even more expressed when the potential was shifted to the value of –1.0 V. The experiment was then moved to the chronoamperometry at a constant applied potential of –0.9 V with the intent to be continued until the current density reached the steady–state value. It can be seen in Figure 3.26 B, that it took more than 1.5 h for the electrode to be stabilized under these conditions. The H_2 bubbles started to be released from about 0.6 mA/cm^2 and the cathodic current density increased more than 3 times until stabilization.

Morphological characterization was aimed at assessing Co–Mo–O–S film after 1.5 h performance at -0.9 V. The SEM analysis revealled the presence of holes formed through the nodule-based structure (Fig. 3.27 a). The AFM data confirmed that the surface roughness increased more than twice without any noticeable film degradation. In this case, the more opened pores and the rougher surface may increase the

accessibility to the active sites for HER. Finally, the EDX elemental composition data of the freshly prepared Co–Mo–O–S film and the film after electrolysis was compared and presented in Table 3.2. As the most important feature, phosphorus was detected to be inserted from the phosphate buffer into the Co–Mo–O–S film composition after working for 1.5 h under HER conditions (Fig. 3.27 b).

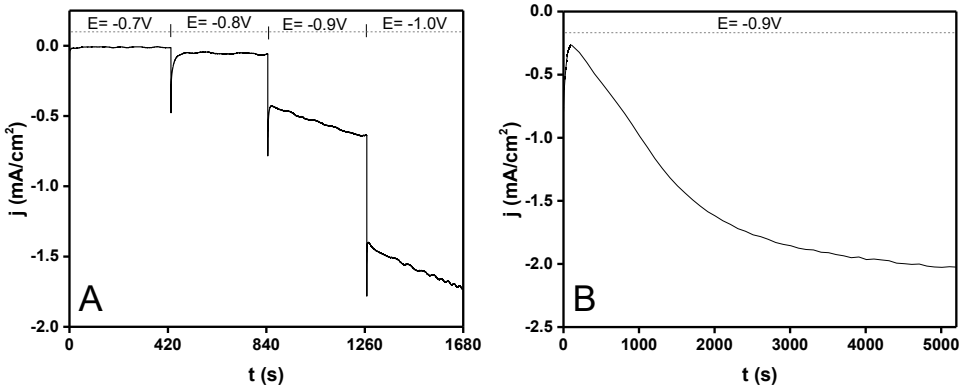

Fig. 3.26. Chronoamperometric responses of as-deposited Co–Mo–O–S film (3 sweep-cycles in pH 6 adjusted electrolysis bath) at various (A) and constant –0.9V potential (B) in 1 M phosphate buffer solution (pH 7)

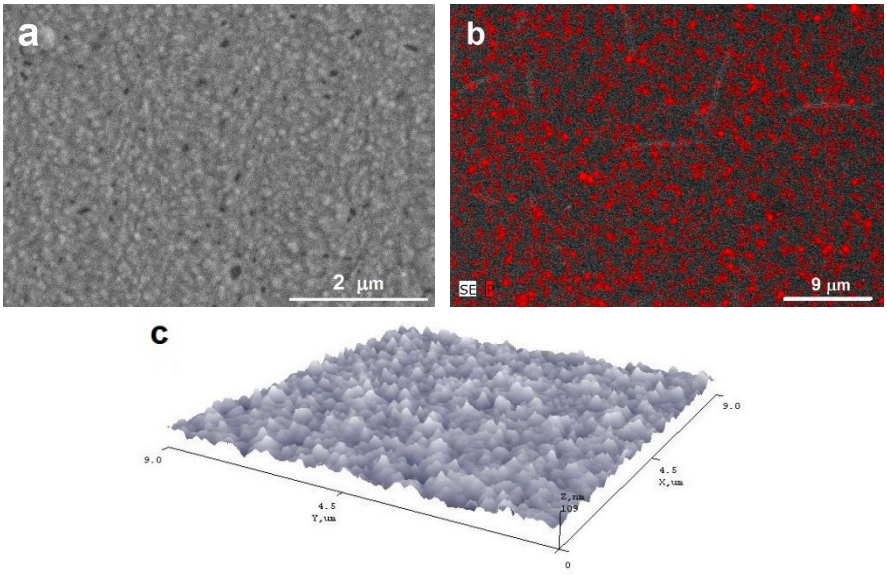

Fig. 3.27. SEM image (a), EDX map of phosphorus (b) and AFM data (c) of Co–Mo–O–S film after constant -0.9 V potential electrolysis in phosphate buffer solution (pH 7)

Table 3.2. Results of EDX analysis for Co–Mo–O–S films before and after being used for –0.9 V electrolysis

No.	Film	Amount in the catalyst (at. %)							
		Co	**Mo**	**S**	**O**	**C**	**Sn**	**Si**	**P**
1.	Co–Mo–O–S *as-deposited*	3.1	3.7	1.3	76.2	2.1	12.0	1.6	-
2.	Co–Mo–O–S *after –0.9 V electrolysis*	2.8	2.7	0.6	78.3	1.2	12.1	2.1	0.2

The results presented above show one of the most interesting experimentally observed features of Co–Mo–O–S films: it is in-situ electrochemical activation during a prolonged electrolysis in a phosphate buffer. This effect is reflected in the decrease of HER overpotentials over the time, as determined by chronoamperommetry and linear sweep voltammetry measurements. This phenomenon was found to be related with the following explanations.

Recent progress concerning in-situ electrochemical activation procedures for the formation of electrocatalyst films with enhanced performance has been summarized in Shang et al's work [139]. The mechanism of cathodic activation was associated with the in-situ changing chemical states of active metal-based species being electro-reduced or electro-converted from bounded to the more active species. Depending on experimental conditions (solutions composition, potential, temperature, etc.), the electrochemical activation was reported to generate various effects, such as the creation of a higher number of active sites and the enlargement of the electroactive surface area. For example, the significant enhancement of the HER catalytic activity of nickel sulfide films was claimed to be mainly caused by the roughened electrode surface with surface rearrangement during cathodic activation [140]. Pumera et al. [141] explored the effect of cathodic treatment on structural and electocatalytic behaviour of various transition metal chalcogenides. In the case of molybdenum sulfide, it has been found that the cathodic reduction results in a smaller sulfur-to-molybdenum ratio as compared to the untreated sample and the reduced films exhibited faster heterogeneous electron transfer rates. An efficient charge injection and the presence of sulfur vacancies were suggested to be responsible for the observed increase in HER activity [142].

On the other hand, the formation of some phosphides on the surface of Co–Mo–O–S films cannot be ruled out during electrolysis in a phosphate buffer [143]. The vast experimental results confirmed that even a low phosphorous amount of around 1% in the deposit has beneficial effects. The incorporation of phosphorous compounds efficiently improves anti-corrosive, mechanical and electrocatalytic properties of Co–Mo films [143]. In addition, the literature review (Section 1.2.4) revealed that metal phosphides are highly active HER electrocatalysts. This assumption is supported by EDX results (Table 3.2) showing the presence of phosphorous in Co–Mo–O–S films after electrolysis.

3.3.3. Effect of a number of deposition cycles

From a theoretical point of view, the higher the catalyst loading, the more effective is the catalyzed reaction. Practically, there are some limitations for electrochemical film

loading effect. As a routine, 3 continuous sweep cycles have already been applied in this work to form homogeneous Co–Mo–O–S films in order to evaluate the effects of the Co:Mo ratio and pH of the deposition bath. These 3 CV films showed good stability results and promising electrocatalytic activity. In this case, Co–Mo–O–S synthesis optimization was further directed to the studies of catalyst loading by varying the number of cyclic voltammetry deposition sweep cycles. First of all, an initial electrolysis bath of pH 8 was used to prepare Co–Mo–O–S film by 10 sweep cycles (Fig. 3.28 A).

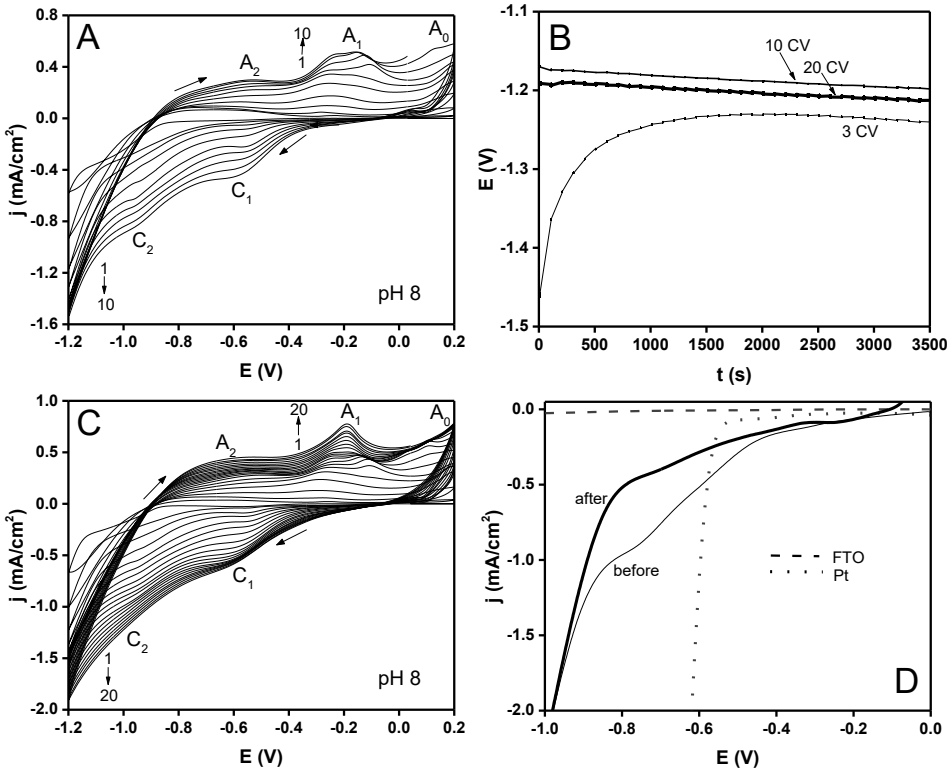

Fig. 3.28. Co–Mo–O–S deposition on FTO using 10 (A) and 20 (C) sweep-cycles in pH 8 electrolysis bath. (B) Chronopotentiograms of different films in phosphate buffer solution (pH 7) at constant applied current density of 5 mA/cm^2. (D) Polarization curves of 20 CV Co–Mo–O–S films in pH 7 buffer solution

Even though the 10 CV sample showed the enhancement in 1 h of intense HER performance (Fig. 3.28 B), the film was visually identified to be mechanically damaged. To be sure, 20 CV deposition was additionally employed using a pH 8 bath. Unfortunately, the 5 mA/cm^2 electrolysis of the corresponding film revealed a decrease in electrocatalytic activity. Furthermore, linear sweep voltammetry, performed before and after 1 h electrolysis (Fig. 3.28 D), confirmed that the film prepared from the pH 8 deposition bath, probably, has no potential to be further improved.

The identical experimental procedure was applied for the Co–Mo–O–S sample deriving from a pH 7.1 deposition bath. Both 10 CV (Fig. 3.29 A) and 20 CV (Fig.

3.29 C) synthesis were performed but the films showed the features of mechanical degradation after 5 mA/cm^2 electrolysis. Even though the chronopotentiometric response was recorded to show a decrease in overpotentials (Fig. 3.29 B), the samples of pH 7.1 were rejected for further investigations according to the visual observations and unfavourable linear sweep results of the film's stability (Fig. 3.29 D).

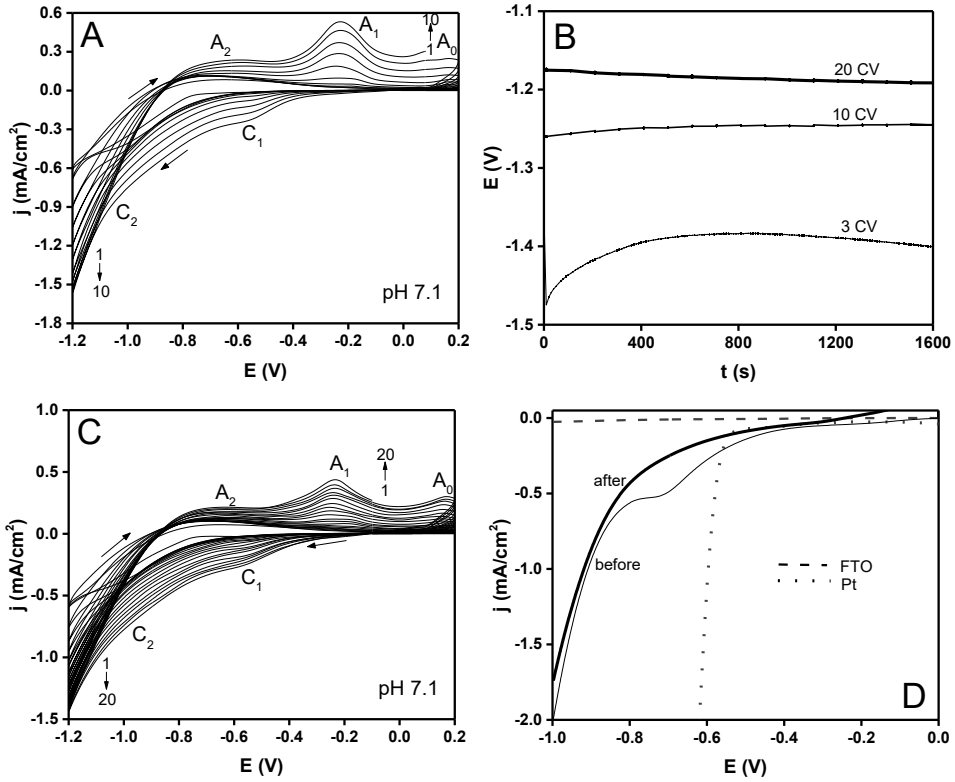

Fig. 3.29. Co–Mo–O–S deposition on FTO using 10 (A) and 20 (C) sweep-cycles in pH 7.1 electrolysis bath. (B) Chronopotentiograms of different films in phosphate buffer solution (pH 7) at constant applied current density of 5 mA/cm^2. (D) Polarization curves of 20 CV Co–Mo–O–S films in pH 7 buffer solution

The 10 CV deposition proved to be a sufficient and reliable loading to further identify the tendencies of Co–Mo–O–S films prepared from pH 6, pH 5.8, pH 5.4, and pH 3 deposition baths. The chronopotentiograms, presented in Figures 3.31 B, 3.32 B, 3.33 B, represent the extremelly reduced electrocatalytic activity in HER for the pH 5.8, pH 5.4, and pH 3 samples. The increased catalyst loading provoked the poorer adhesion of the films. However, special attention should be paid to the pH 6 sample (Fig. 3.30). The film prepared by 10 CVs in a pH 6 deposition bath showed a catalytic enhancement in HER performance when compared with the 3CV sample (Fig. 3.30 B) and had no signs of film degradation after harsh H_2 bubbling conditions.

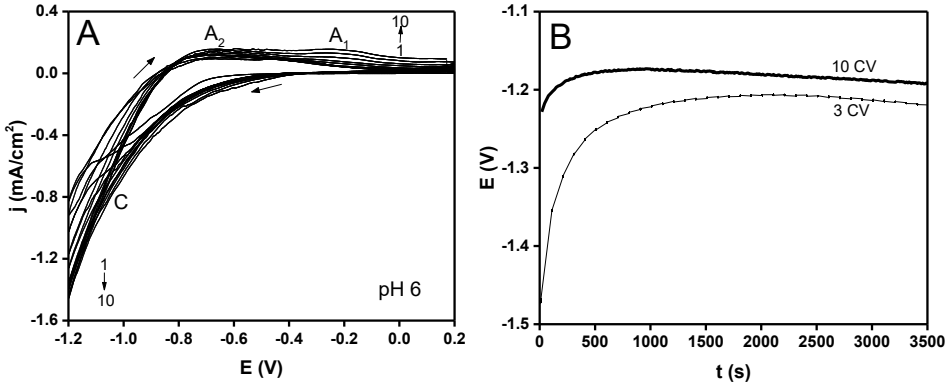

Fig. 3.30. Co–Mo–O–S deposition on FTO using 10 sweep-cycles in pH 6 electrolysis bath (A) and 10 CV vs. 3CV films comparison in phosphate buffer solution (pH 7) at constant applied current density of 5 mA/cm^2 (B)

The hypothesis can be suggested that the effect of catalyst loading is related to the changes in the deposition mechanism and film composition depending on the pH of the electrolysis bath. The particular tendencies in current peaks growth can be seen in the plotted cyclic voltammograms.

When compared with the data of Co–Mo–O–S 3 CV deposition (Fig. 3.21), characteristic cathodic peak C transformed into two intensive peaks C_1 and C_2 recorded for 10 and 20 CV films prepared at pH > 6 solutions. At the upper sweep, anodic peak A_2 increased a little while peaks A_1 and A_0 noticeably enlarged during 10 and 20 CV deposition. This electrode behaviour can be identified to be related to the Co–O–S film deposition mechanism with a predominant increase of characteristic peaks C_1, C_2, and A_1, A_0 (Section 3.1.1). To be more precise, as the number of deposition cycles increases, the part of the Co–O–S is enlarged in the pH > 6 Co–Mo–O–S films. This hypothesis is in a good agreement with the results of the films composition: at pHs > 6, Co phase is a dominant precipitate (Table 3.1). Unfortunatelly, Co–O–S films were previously identified to be unstable in pH 7 phosphate buffer solution and this behaviour more or less reflects in the pH 8 and pH 7.1 Co–Mo–O–S films.

When the pH of the deposition bath is lower than 6, the cyclic deposition voltammograms show the similarities to Mo–O–S film deposition mechanism (Fig. 3.5 B). The cathodic part of the deposition is expressed by one characteristic peak C while the anodic part shows the presence of peaks A_2 and A_1. It is interesting to note, that the peak A_1 does not show the tendency to grow while the peak A_2 increases in all cases during 10 CV deposition. The predominant amount of Mo phase was confirmed by compositional data for pH < 6 films (Table 3.1), thus these co-deposited structures may be unfavourable to catalyse HER in a phosphate buffer solution.

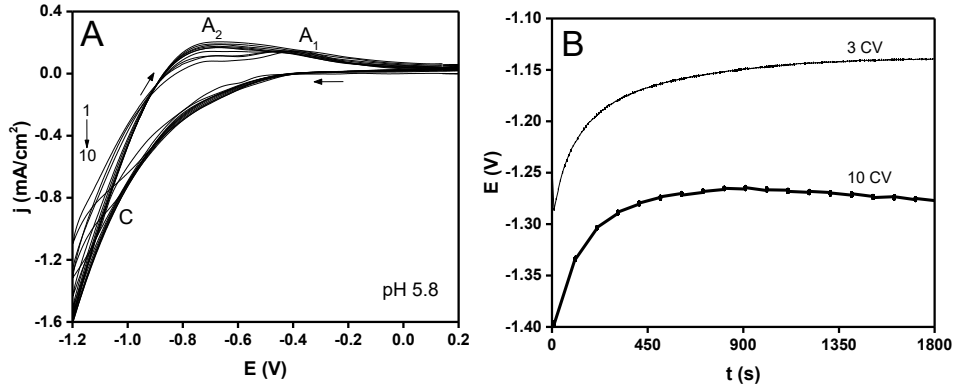

Fig. 3.31. Co–Mo–O–S deposition on FTO using 10 sweep-cycles in pH 5.8 electrolysis bath (A) and 10 CV vs. 3 CV films comparison in phosphate buffer solution (pH 7) at constant applied current density of 5 mA/cm^2 (B)

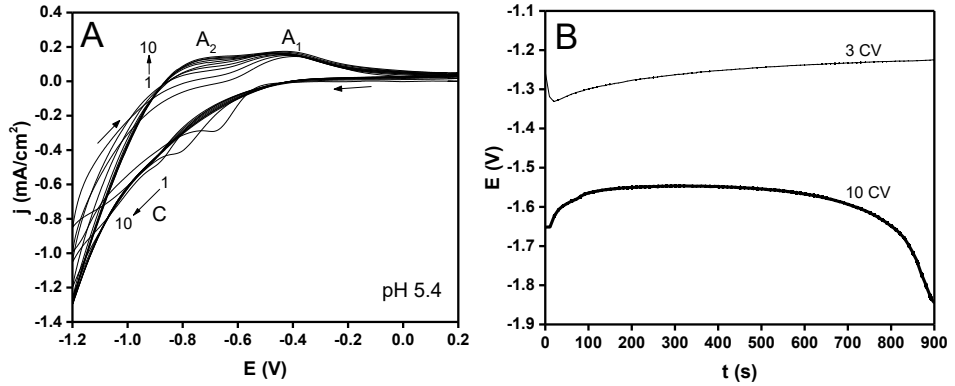

Fig. 3.32. Co–Mo–O–S deposition on FTO using 10 sweep-cycles in pH 5.4 electrolysis bath (A) and 10 CV vs. 3 CV films comparison in phosphate buffer solution (pH 7) at constant applied current density of 5 mA/cm^2 (B)

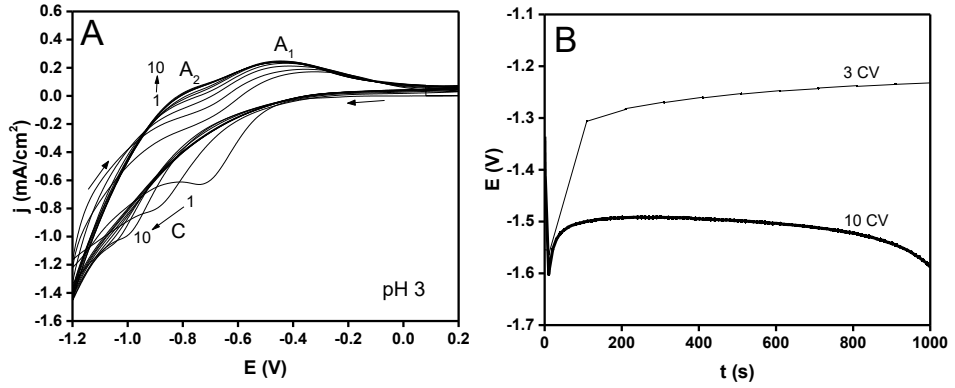

Fig. 3.33. Co–Mo–O–S deposition on FTO using 10 sweep-cycles in pH 3 electrolysis bath (A) and 10 CV vs. 3 CV films comparison in phosphate buffer solution (pH 7) at constant applied current density of 5 mA/cm^2 (B)

Above all, it can be seen in Figure 3.30 A that the mechanism of Co–Mo–O–S film formation at pH 6 is based on the equivalent heights of both anodic peaks A_2 and A_1 while the cathodic part is expressed by a constant growth of peak C. This mechanism can be related with the previously identified Co:Mo ratio being ~1:1 (Table 3.1). The hypothesis of synergy between favourable Co–O–S and Mo–O–S activity and stability features in pH 6 co-deposition conditions can be emphasized here.

3.4. Co–Mo–O–S films performance as HER catalyst

3.4.1. Co–Mo–O–S as HER catalyst in acidic media

In a majority of the related research, the catalytic activity of Co–Mo sulfides and their compounds were generally studied in H^+ rich acidic media electrolytes. For instance, Meng et al. receantly summarized more than fourty MoS_2-based materials performing HER in H_2SO_4 electrolyte [144]. In addition, the series of new Co–Mo–S structures were also examined, particularly in acidic media [88, 111, 112, 114, 116, 145]. In this regard, a brief experimental study in pH 0 media was dedicated for the several films that exhibited the best performance in a phosphate buffer.

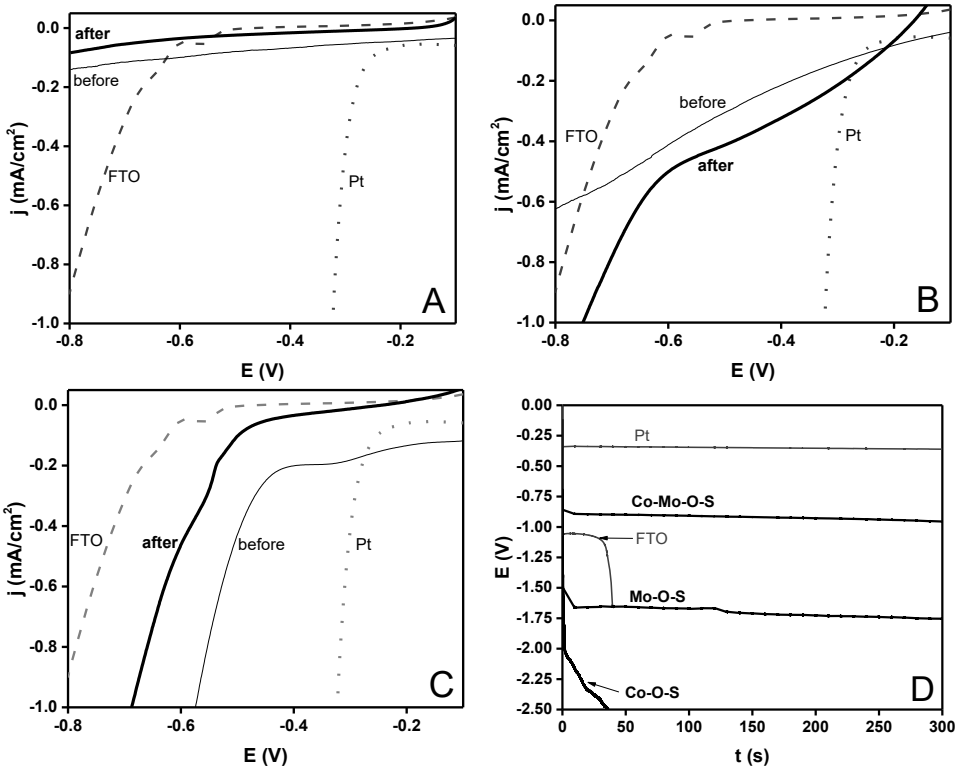

Fig. 3.34. Polarization curves of FTO/Co–O–S (A), FTO/Mo–O–S (B) and FTO/Co–Mo–O–S (prepared at pH 6) (C) electrodes in 1.0 M H_2SO_4 solution (pH 0) at a scan rate of 5 mV/ s before and after 5 mA/cm^2 electrolysis. (D) Chronopotentiograms recorded in pH 0 1.0 M H_2SO_4 solution at constant applied cathodic current density of 5 mA/cm^2

The Co–Mo–O–S film, prepared in a pH 6 deposition bath by 3 sweep-cycles, was employed to catalyse HER in a 1.0 M H_2SO_4 solution under intense 5 mA/cm^2 cathodic electrolysis conditions. The chronopotentiometric response was then compared with the behaviour of corresponding 3CV films of Co–O–S and Mo–O–S samples, bare FTO substrate, and the benchmark electrode of Pt (Fig. 3.34 D). In addition, the linear sweep voltammetry in the 1.0 M H_2SO_4 solution was employed for films before and after being used in pH 0 electrolysis (Fig. 3.34 A–C).

It can be seen that Co–O–S alone is not capable to operate in the acidic media. Despite the high overpotentials, the Mo–O–S film showed the manner of a relatively stable material. Even though the catalytic behaviour recorded before and after acidic electrolysis revealed the activity-induced performance, the tendency of film degradation was visually observed. Among others, the Co–Mo–O–S sample demonstrated the stable catalytic behaviour with the lowest overpotentials. Before electrolysis, the Co–Mo–O–S film initiated HER from about –0.4 V and 1 mA/cm^2 was reached at 250 mV overpotentials. However, the reduced catalytic activity was recorded and mechanical degradation was identified after the film being used for intense electrolysis.

3.4.2. Co–Mo–O–S prospect in HER

Through the efforts to combine the alternative precursors, to preliminary identify the structures obtained, to propose the deposition mechanism, and to optimize the synthesis conditions, there should finally be introduced the essential features of a novel Co–Mo–O–S material for pH neutral hydrogen generation.

The Co–Mo–O–S film prepared at the pH 6 adjusted electrolysis bath, containing 0.005 M $CoCl_2$, 0.005 M ammonium molybdate and 0.5 M thiourea, was established to be a buildable catalytic material. This can be defined as a property for catalyst to be improved via increased deposition sweep cycles. For instance, 50 CV potential cycling procedure yielded the homogeneous and intense black appearance film with a smooth and specular surface. It can be seen in Figure 3.35, that the mechanism of film formation is driven by the constant evolution of both anodic peaks A_2 and A_1 while the cathodic part showed the increase via sustained peak C.

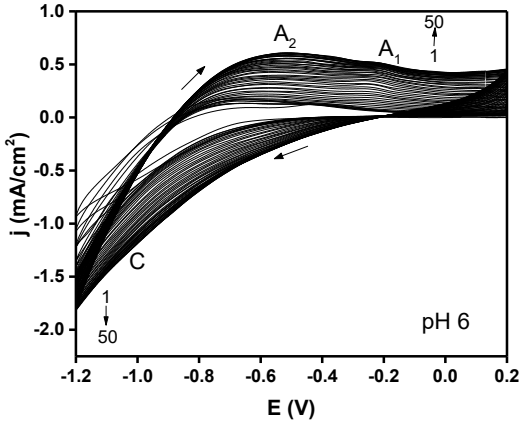

Fig. 3.35. Cyclic voltamperograms of Co–Mo–O–S on FTO fabricated using 50 sweep-cycles in pH 6 adjusted electrolysis bath

Based on the previous disscussions (Section 3.1), the hypothetical deposition mechanism includes the constant Co–O and Mo–O species formation with the following TU species electro-adsorption and electro-oxidation to FD via corresponding peaks A_2 and A_1. After S is incorporated into the structure, the TU-based lattice is desorbed from the surface cathodically.

The evolution of the catalyst morphology was confirmed by structural comparison of 3 CV, 10 CV, and 50 CV samples. A series of SEM images demonstrate that the tightly packed nodule-based structure remains for all Co–Mo–O–S films, while the nodules obviously grow in tandem with the increase of catalyst loading (Fig. 3.36). Additionally, the profilommetry was employed to detect the film thickness evolution. An average thickness was determined to be 315, 510, and 1950 nm for the films deposited after 3, 10, and 50 sweep cycles.

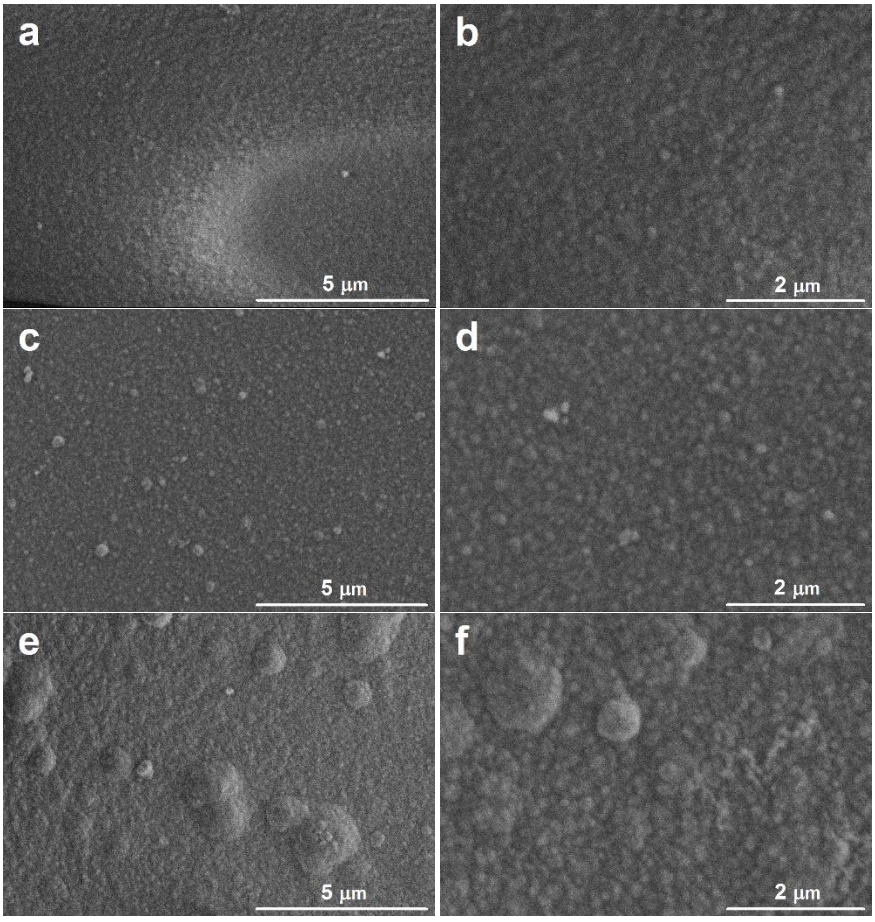

Fig. 3.36. SEM images of Co–Mo–O–S films deposited on FTO at pH 6 with different deposition CV cycles: 3 (a–b), 10 (c–d) and 50 (e–f) CVs

The XPS analysis showed interesting features of Co–Mo–O–S film evolution. The data of the Co, Mo, and S amount in the as-deposited films is plotted in Figure 3.37. It can be seen that the amount of cobalt had a tendency to decrease while both

Mo and S were detected to be increased for the samples prepared by 3, 10, and 50 cycles. This behaviour can be explained by the observations of slight pH change of the deposition solution during prolonged synthesis conditions. Particularly, the pH showed a tendency to decrease during potential cycling and this effect was detected via a prolonged 50 CV deposition. It was previously discussed that the pH < 6 deposition provoke predominant Mo precipitation with reduced amounts of Co, respectively.

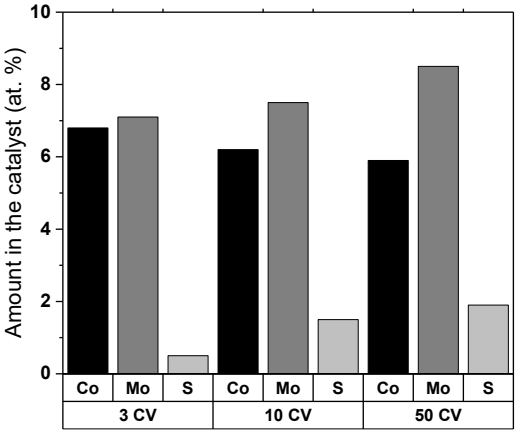

Fig. 3.37. Column plot for XPS elemental composition data of 3CV, 10CV and 50CV electrodes

The results presented in Figure 3.38 clearly show the importance of the amount and composition of electroactive material. Linear sweep voltammetry was typically recorded in a context of catalytically inactive FTO glass substrate and Pt, as a benchmark electrode for HER. The reaction was increasingly accelerated in tandem with the progress of the film's deposition sweep cycles. The best catalytic performance was obtained by pH 6 Co–Mo–O–S film prepared after 50 sweep cycles. In this case, 1 mA/cm^2 was reached with only 140 mV overpotentials while operating in a pH 7 phosphate buffer solution.

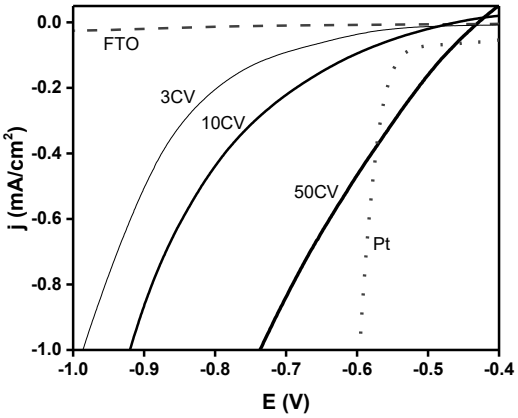

Fig. 3.38. Characteristic voltammograms of 3CV, 10CV and 50CV Co–Mo–O–S films in phosphate buffer solution (pH 7) at a scan rate 5 mV/s

The data of the linear sweep voltammetry was then used to express the fundamentals of hydrogen evolution reaction. In this case, Tafel analysis was under deeper investigation.

The key issue for HER electrocatalyst is to operate through the most effective hydrogen adsorption-desorption path. Adsorption is the most expressed when 30 mV is obtained as the initial Tafel slope and the slope around 120 mV or more, related with the increased desorption abilities, should be reached as late as possible. These particular values in mV are the fundamental Tafel slopes (constants b) benchmarking the HER path on the Pt electrode in acidic media and indicating Tafel (30 mV), Heyrovsky (40 mV), and Volmer (120 mV) steps being the rate determining at the particular potential range. However, only two different Tafel slope values are typically observed for the less active catalytic materials: a lower slope (about 40-60 mV) at low overpotentials, and a higher one (~120 mV) at high overpotentials. Nevertheless, smaller Tafel slopes are expected to be indicators of the high H adsorption and, thus, the enhanced ability of the electrocatalyst to initiate HER under low overpotentials.

For the sake of clarity, the experimental data of Pt polarization in an acidic media was included to observe all three steps of HER. Parallely, Pt was polarized in pH 7 phosphate buffer solution in the corresponding potentials window for the path of HER. These results of Pt behaviour are presented in Figure 3.39 A and are very close to the fundamental values of constant b.

The corresponding potential window (i.e. the region is between –0.5 V and –0.7 V) determined in the pH 7 media was then applied for Tafel analysis for the polarization of 3, 10, and 50 CVs Co–Mo–O–S films (Fig. 3.39 B). First of all, it can be seen that the value of b=103 mV is common for all samples at higher overpotentials, nevertheless, the enhancement of catalytic activity can be compared via the mechanism up to -0.6 V. Two steps of HER with a relatively high initial constant of b = 90 mV can be identified for the 3 CV sample. Similar electrode behaviour can be identified for the 10 CV Co–Mo–O–S sample but with lower initial constant b = 58 mV in the same potentials range. Finally, the sequence of three fundamental steps can be identified for the 50 CV film. The values of corresponding Tafel slopes are 32 mV, 56 mV, and 103 mV and the mechanism of HER on 50 CV Co–Mo–O–S film resemble the effective behaviour of Pt via the Volmer-Heyrovsky-Tafel path in the overpotentials < 200 mV.

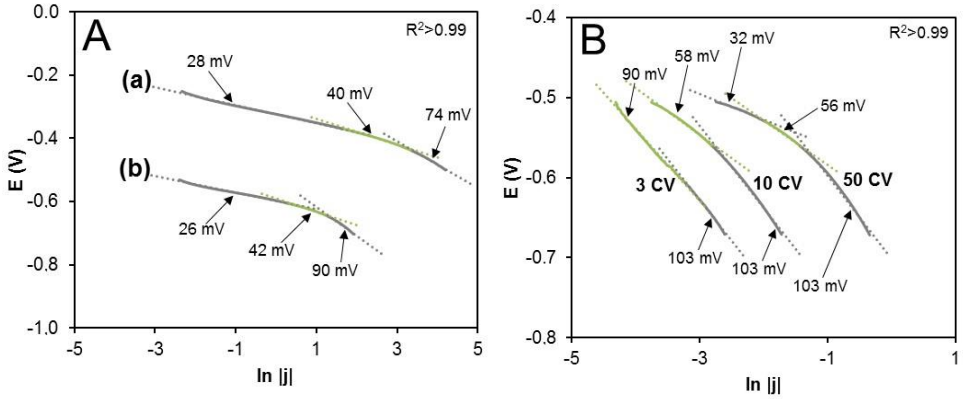

Fig. 3.39. Tafel plots and constants b for (A) platinum electrode in 1.0 M H_2SO_4 solution (pH 0) (a), in 1.0 M phosphate buffer solution (pH 7) (b) and (B) 3CV, 10CV and 50CV Co–Mo–O–S films in phosphate buffer solution (pH 7)

Figure 3.40 A represents the potentials for pH neutral hydrogen evolution expressed by chroamperommetric curves when polarizing FTO and Pt substrates at 5 mA/cm^2 current density in a phosphate buffer solution. The results confirm that the bare FTO substrate is a poor HER electrocatalyst with overpotentials of about 900 mV under specified experimental conditions. Clearly, the hindering of the HER rate can be related to both the intrinsic properties of tin oxide and the adsorption of phosphate ions on its surface. In contrast, Pt as the best known electrocatalyst for HER, show the upper limits of polarization performance in pH 7 solution (Fig. 3.40 A). However, the increase in HER overpotentials was recorded for fundamentally inert Pt electrode operating under prolonged electrolysis conditions (Fig. 3.40 B). This effect can be related to the strong affinity of phosphate ions with the metal surface. It is well-known that phosphate is widely used as a corrosion inhibitor for steels in aqueous solutions. Particularly, a detailed voltammetric study about the adsorption of phosphate species on polycrystalline Pt electrodes in a wide pH range has been performed in Gisbert et al's study [146]. The strong affinity is believed to be caused by phosphate ions exchanging with hydroxyl groups adsorbed on the surface. As this effect becomes relatively weaker at higher pH values, it can provoke the decisive consequences for the pH-dependent electrocatalytic activity of Pt.

The most promising results of Co–Mo–O–S films are presented in a context of Pt behaviour (Fig. 3.40 B). The evolution of catalytic activity with prolonged stability features under harsh H_2 bubbling electrolysis conditions was recorded parallelly with increasing the number of film deposition sweep cycles. Above all, the activity of 50 CV Co–Mo–O–S film reached the values of Pt electrode after 1 h of HER at 5 mA/cm^2 cathodic current density. These results suggest the further direction of research on Co–Mo–O–S films successfully catalyzing HER in a pH neutral solution.

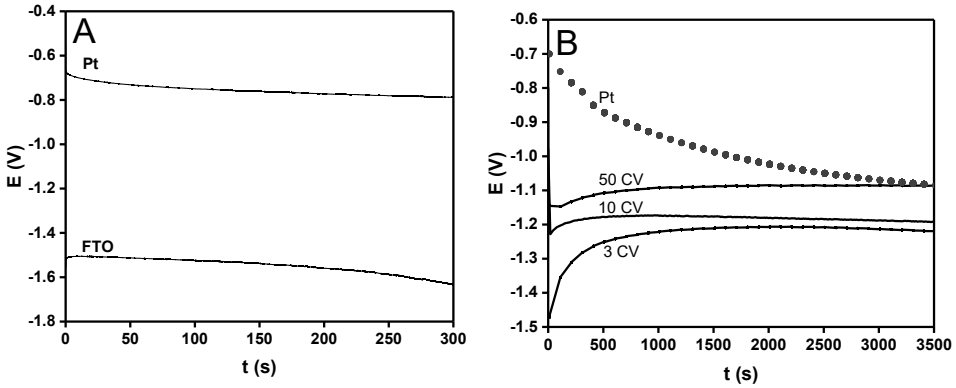

Fig. 3.40. Potentials range for Pt and FTO electrodes (A) and 3CV, 10CV, 50CV Co–Mo–O–S electrodes behaviour (B) during HER at 5 mA/cm^2 electrolysis in phosphate buffer solution (pH 7)

The research presented in this thesis provide deep insights into the Co–Mo–O–S material. However, there are several lines of research arising from this work which should be further pursued. It should be useful:

- to perform *in-situ* spectroscopic investigations and to detail the structure and morphology of the catalytic layer;
- to carry out quantitative and qualitative analysis of the generated gas;
- to evaluate the influence of process parameters (electrode area, cell volume, current density of prolonged electrolysis, etc);
- to use solution buffering to the synthesis bath;
- to engineer a water splitting cell with accommodated Co–Mo–O–S and Co–Pi electrodes, as hydrogen and oxygen evolution catalysts, respectively. The Co–Pi catalyst was previously investigated in the university's laboratory as a successful anode material. This amorphous catalyst has recently been discovered to be one of the most effective oxygen evolution materials operating exclusively in a pH 7 phosphate buffer solution [147].

CONCLUSIONS

1. One-step potentiodynamic electrochemical deposition was applied for the synthesis of various S-containing cobalt and molybdenum oxide films on conductive glass substrates. The room temperature electrodeposition, set between -1.2 V and 0.2 V potentials in an electrolysis bath containing cobalt (II) and molybdenum (VI) salts and thiourea, was proved to be an efficient technique for the synthesis of HER electrocatalysts active in pH 7 phosphate buffer solution. The mechanisms of film formation were proposed.
2. It was confirmed that the electrodeposition from thiourea and cobalt (II) chloride bath leads to the formation of amorphous, honeycomb-like S-containing cobalt oxide (Co–O–S) films. The electrochemical behaviour of Co–O–S films showed a possibility to be applied as an active electrocatalysts in electrochemical water splitting; however, the prepared films suffered from fast corrosion.
3. Amorphous S-containing molybdenum oxide (Mo–O–S) films were successfully electrodeposited using a thiourea and ammonium molybdate bath. The films had a thickness of 245 nm, a smooth surface, an enhanced stability compared to Co–O–S electrocatalysts, and a Tafel slope of 85 mV at an overpotential of 100 mV.
4. The codeposition of cobalt and molybdenum oxide films significantly improved the stability and activity properties of the prepared Co–Mo–O–S films as compared to the individual Co–O–S and Mo–O–S electrocatalysts. The prolonged electrolysis at a constant current density of 5 mA/cm^2 resulted in the decrease of HER overpotential and was associated with an activation-induced effect for Co–Mo–O–S films.
5. It was determined that the activity of Co–Mo–O–S films was extremely dependent on the pH of the electrolysis bath, the precursor concentration and the number of electrodeposition cycles. The optimization of the synthesis conditions revealed that the best HER performance was obtained for 1950 nm thick films prepared under the following conditions: pH 6 solution, up to 50 deposition cycles, the Co:Mo ratio being close to 1:1.5.
6. The electrocatalytic behavior of the best-performing Co–Mo–O–S films was found to be very close to the polycrystalline Pt electrode. The results of a Tafel analysis suggested that the HER on the surface of Co–Mo–O–S films proceeded through the Volmer-Heyrovsky-Tafel path at the overpotentials < 200 mV.

ACKNOWLEDGEMENTS

I would like to express my gratitude to my supervisor *prof. Eugenijus Valatka*. Thank you for thinking with me, for motivation and for guiding me with big doses of patience. I greatly appreciate the opportunities you created to find my own path and the support you offered when needed. It was an invaluable experience to observe the both: the H_2 evolution and the evolution of your impressive career.

Special thanks are dedicated to *Martynas Lelis* and *Simona Tučkutė* (LEI) for their major contribution in sample analysis. My sincere thanks also go to *Ingrida Ancutienė, Nijolė Dukštienė, Žaneta Rukuižienė, Andrius Jaskūnas* and *Patrick Chemaly* for their time, cooperation and professional advice dedicated to this thesis.

Some special words of gratitude go to my labmates *Agnė Šulčiūtė* and *Simona Ostachavičiūtė* for the beginning of my path and *Ieva Barauskienė* for the support at the end. I also thank my PhD colleagues *Rūta Sidaravičiūtė*, *Dalia Buivydienė* and *Deimantė Simanavičiūtė* for their friendship, cooperation and the best coffee breaks. Many thanks go to my friends *Aušra Kizelevičiūtė*, *Vita Sereikaitė* and *Esmira Mamedova* for more than 10 years of fun with and without chemistry.

Last but not the least, I would like to thank my parents, *Anelė Mardosienė* and *Sigitas Mardosa*, my brother *Gintaras Mardosa* and his family, along with my source of happiness *Povilas Ivanauskas* for always believing in me. Your wisdom and knowledge have encouraged me to follow the highest standards.

REFERENCES

1. International Energy Agency (2017) World Energy Outlook 2017. [e-resource] http://www.iea.org/media/weowebsite/2017/Chap2011_WEO2017.pdf (accessed Feb 13, 2018)
2. Züttel, A., Borgschulte, A., Schlapbach, L. (2008) *Hydrogen as a Future Energy Carrier*. Wiley-VCH
3. World Energy Council (2016) World Energy Resources 2016. [e-resource] https://www.worldenergy.org/wp-content/uploads/2016/2010/World-Energy-Resources-Full-report-2016.2010.2003.pdf (accessed Feb 13, 2018)
4. Dincer, I., Acar, C. (2015) Review and evaluation of hydrogen production methods for better sustainability. *International Journal of Hydrogen Energy*. 40, 11094-11111
5. European Environment Agency (2017) Trends and projections in the EU ETS in 2017. In The EU Emissions Trading System in numbers [e-resource] https://www.eea.europa.eu/publications/trends-and-projections-EU-ETS-2017 (accessed Feb 13, 2018)
6. Godula-Jopek, A. (2015) *Hydrogen Production: by Electrolysis*. Wiley-VCH; 1 edition
7. Grochala, W., Edwards, P. P. (2004) Thermal Decomposition of the Non-Interstitial Hydrides for the Storage and Production of Hydrogen. *Chemical Reviews*. 104, 1283-1316
8. Muradov, N. Z., Veziroğlu, T. N. (2005) From hydrocarbon to hydrogen–carbon to hydrogen economy. *International Journal of Hydrogen Energy*. 30, 225-237
9. Sørensen, B., Spazzafumo, G. (2018) *Hydrogen and Fuel Cells (Third Edition)*. Academic Press
10. Holladay, J. D., Hu, J., King, D. L., Wang, Y. (2009) An overview of hydrogen production technologies. *Catalysis Today*. 139, 244-260
11. Ursua, A., Gandia, L. M., Sanchis, P. (2012) *Hydrogen Production From Water Electrolysis: Current Status and Future Trends.* Proceedings of the IEEE. 100, 410-426
12. Balat, M. (2008) Potential importance of hydrogen as a future solution to environmental and transportation problems. *International Journal of Hydrogen Energy*. 33, 4013-4029
13. Council, N. R., Engineering, N. A. o. (2004) The Hydrogen Economy: Opportunities, Costs, Barriers, and R&D Needs. *The National Academies Press*, Washington, DC
14. Balat, H., Kırtay, E. (2010) Hydrogen from biomass – Present scenario and future prospects. *International Journal of Hydrogen Energy*. 35, 7416-7426
15. Hallenbeck, P. C., Abo-Hashesh, M., Ghosh, D. (2012) Strategies for improving biological hydrogen production. *Bioresource Technology*. 110, 1-9
16. Levin, D. B., Pitt, L., Love, M. (2004) Biohydrogen production: prospects and limitations to practical application. *International Journal of Hydrogen Energy*. 29, 173-185

17. Janssen, H., Bringmann, J. C., Emonts, B., Schroeder, V. (2004) Safety-related studies on hydrogen production in high-pressure electrolysers. *International Journal of Hydrogen Energy*. 29, 759-770
18. Steinfeld, A. (2005) Solar thermochemical production of hydrogen—a review. *Solar Energy*. 78, 603-615
19. Rajeshwar, K., McConnell, R., Licht, S. E. (2008) *Solar Hydrogen Generation - Toward a Renewable Energy Future*. Springer-Verlag New York
20. Aroutiounian, V. M., Arakelyan, V. M., Shahnazaryan, G. E. (2005) Metal oxide photoelectrodes for hydrogen generation using solar radiation-driven water splitting. *Solar Energy*. 78, 581-592
21. Ozbilen, A., Dincer, I., Rosen, M. A. (2011) A comparative life cycle analysis of hydrogen production via thermochemical water splitting using a Cu–Cl cycle. *International Journal of Hydrogen Energy*. 36, 11321-11327
22. Léon, A. (2008) *Hydrogen Technology. Mobile and Portable Applications*. Springer-Verlag Berlin Heidelberg
23. Züttel, A. (2004) Hydrogen storage methods. *Naturwissenschaften*. 91, 157-172
24. Sakintuna, B., Lamari-Darkrim, F., Hirscher, M. (2007) Metal hydride materials for solid hydrogen storage: A review. *International Journal of Hydrogen Energy*. 32, 1121-1140
25. Yang, J., Sudik, A., Wolverton, C., Siegel, D. J. (2010) High capacity hydrogen storage materials: attributes for automotive applications and techniques for materials discovery. *Chemical Society Reviews*. 39, 656-675
26. Zheng, J., Liu, X., Xu, P., Liu, P., Zhao, Y., Yang, J. (2012) Development of high pressure gaseous hydrogen storage technologies. *International Journal of Hydrogen Energy*. 37, 1048-1057
27. Stetson, N. (2017) U.S. Department of Energy, Hydrogen and Fuel Cells Program; 2017 Annual Merit Review and Peer Evaluation Meeting, [e-resource] https://www.hydrogen.energy.gov/pdfs/review17/st000_stetson_2017_o.pdf (accessed Feb 12, 2018)
28. Cardella, U., Decker, L., Sundberg, J., Klein, H. (2017) Process optimization for large-scale hydrogen liquefaction. *International Journal of Hydrogen Energy*. 42, 12339-12354
29. Panella, B., Hirscher, M., Roth, S. (2005) Hydrogen adsorption in different carbon nanostructures. *Carbon*. 43, 2209-2214
30. Nagar, R., Vinayan, B. P., Samantaray, S. S., Ramaprabhu, S. (2017) Recent advances in hydrogen storage using catalytically and chemically modified graphene nanocomposites. *Journal of Materials Chemistry A*. 5, 22897-22912
31. Hirscher, M., Panella, B. (2007) Hydrogen storage in metal–organic frameworks. *Scripta Materialia*. 56, 809-812
32. Murray, L. J., Dinca, M., Long, J. R. (2009) Hydrogen storage in metal-organic frameworks. *Chemical Society Reviews*. 38, 1294-1314
33. Qiu, S., Chu, H., Zou, Y., Xiang, C., Xu, F., Sun, L. (2017) Light metal borohydrides/amides combined hydrogen storage systems: composition, structure and properties. *Journal of Materials Chemistry A*. 5, 25112-25130

34. Sapountzi, F. M., Gracia, J. M., Weststrate, C. J., Fredriksson, H. O. A., Niemantsverdriet, J. W. (2017) Electrocatalysts for the generation of hydrogen, oxygen and synthesis gas. *Progress in Energy and Combustion Science*. 58, 1-35
35. Turner, J., Sverdrup, G., Mann Margaret, K., Maness, P. C., Kroposki, B., Ghirardi, M., Evans Robert, J., Blake, D. (2007) Renewable hydrogen production. *International Journal of Energy Research*. 32, 379-407
36. Yu, B., Zhang, W., Xu, J., Chen, J., Luo, X., Stephan, K. (2012) Preparation and electrochemical behavior of dense YSZ film for SOEC. *International Journal of Hydrogen Energy*. 37, 12074-12080
37. Li, X., Hao, X., Abudula, A, Guan, G. (2016) Nanostructured catalysts for electrochemical water splitting: current state and prospects. *Journal of Materials Chemistry A*. 4, 11973-12000
38. Wang, M., Wang, Z., Gong, X., Guo, Z. (2014) The intensification technologies to water electrolysis for hydrogen production – A review. *Renewable and Sustainable Energy Reviews*. 29, 573-588
39. Seo, B., Joo, S. H. (2017) Recent advances in unveiling active sites in molybdenum sulfide-based electrocatalysts for the hydrogen evolution reaction. *Nano Convergence*. 4, 19
40. Zeng, M., Li, Y. (2015) Recent advances in heterogeneous electrocatalysts for the hydrogen evolution reaction. *Journal of Materials Chemistry A*. 3, 14942-14962
41. Lin, M.-Y., Hourng, L.-W., Kuo, C.-W. (2012) The effect of magnetic force on hydrogen production efficiency in water electrolysis. *International Journal of Hydrogen Energy*. 37, 1311-1320
42. Li, S.-D., Wang, C.-C., Chen, C.-Y. (2009) Water electrolysis in the presence of an ultrasonic field. *Electrochimica Acta*. 54, 3877-3883
43. Lao, L., Ramshaw, C., Yeung, H. (2011) Process intensification: water electrolysis in a centrifugal acceleration field. *Journal of Applied Electrochemistry*. 41, 645-656
44. Conway, B. E., Tilak, B. V. (2002) Interfacial processes involving electrocatalytic evolution and oxidation of H_2, and the role of chemisorbed H. *Electrochimica Acta*. 47, 3571-3594
45. Kahyarian, A., Brown, B., Nesic, S. (2017) Mechanism of the Hydrogen Evolution Reaction in Mildly Acidic Environments on Gold. *Journal of The Electrochemical Society*. 164, H365-H374
46. Vilekar, S. A., Fishtik, I., Datta, R. (2010) Kinetics of the Hydrogen Electrode Reaction. *Journal of The Electrochemical Society*. 157, B1040-B1050
47. Seh, Z. W., Kibsgaard, J., Dickens, C. F., Chorkendorff, I., Nørskov, J. K., Jaramillo, T. F. (2017) Combining theory and experiment in electrocatalysis: Insights into materials design. *Science*. 355, 6321
48. Li, Y., Wang, H., Xie, L., Liang, Y., Hong, G., Dai, H. (2011) MoS_2 Nanoparticles Grown on Graphene: An Advanced Catalyst for the Hydrogen Evolution Reaction. *Journal of the American Chemical Society*. 133, 7296-7299

49. Jiao, Y., Zheng, Y., Jaroniec, M., Qiao, S. Z. (2015) Design of electrocatalysts for oxygen- and hydrogen-involving energy conversion reactions. *Chemical Society Reviews*. 44, 2060-2086
50. Greeley, J., Jaramillo, T. F., Bonde, J., Chorkendorff, I., Nørskov, J. K. (2006) Computational high-throughput screening of electrocatalytic materials for hydrogen evolution. *Nature Materials*. 5, 909-913
51. Nørskov, J. K., Bligaard, T., Logadottir, A., Kitchin, J. R., Chen, J. G., Pandelov, S., Stimming, U. (2005) Trends in the Exchange Current for Hydrogen Evolution. *Journal of The Electrochemical Society*. 152, J23-J26
52. Skúlason, E., Tripkovic, V., Björketun, M. E., Gudmundsdóttir, S., Karlberg, G., Rossmeisl, J., Bligaard, T., Jónsson, H., Nørskov, J. K. (2010) Modeling the Electrochemical Hydrogen Oxidation and Evolution Reactions on the Basis of Density Functional Theory Calculations. *The Journal of Physical Chemistry C*. 114, 18182-18197
53. Morales-Guio, C. G., Stern, L.-A., Hu, X. (2014) Nanostructured hydrotreating catalysts for electrochemical hydrogen evolution. *Chemical Society Reviews*. 43, 6555-6569
54. Benck, J. D., Hellstern, T. R., Kibsgaard, J., Chakthranont, P., Jaramillo, T. F. (2014) Catalyzing the Hydrogen Evolution Reaction (HER) with Molybdenum Sulfide Nanomaterials. *ACS Catalysis*. 4, 3957-3971
55. Maiyalagan, T., Chemelewski, K. R., Manthiram, A. (2014) Role of the Morphology and Surface Planes on the Catalytic Activity of Spinel $LiMn_{1.5}Ni_{0.5}O_4$ for Oxygen Evolution Reaction. *ACS Catalysis*. 4, 421-425
56. Marković, N. M., Grgur, B. N., Ross, P. N. (1997) Temperature-Dependent Hydrogen Electrochemistry on Platinum Low-Index Single-Crystal Surfaces in Acid Solutions. *The Journal of Physical Chemistry B*. 101, 5405-5413
57. Eftekhari, A. (2017) Electrocatalysts for hydrogen evolution reaction. *International Journal of Hydrogen Energy*. 42, 11053-11077
58. Soares, D. M., Teschke, O., Torriani, I. (1992) Hydride Effect on the Kinetics of the Hydrogen Evolution Reaction on Nickel Cathodes in Alkaline Media. *Journal of The Electrochemical Society*. 139, 98-105
59. Strmcnik, D., Lopes, P. P., Genorio, B., Stamenkovic, V. R., Markovic, N. M. (2016) Design principles for hydrogen evolution reaction catalyst materials. *Nano Energy*. 29, 29-36
60. Faber, M. S., Jin, S. (2014) Earth-abundant inorganic electrocatalysts and their nanostructures for energy conversion applications. *Energy & Environmental Science*. 7, 3519-3542
61. Su, J., Zhou, J., Wang, L., Liu, C., Chen, Y. (2017) Synthesis and application of transition metal phosphides as electrocatalyst for water splitting. *Science Bulletin*. 62, 633-644
62. Vrubel, H., Hu, X. (2012) Molybdenum Boride and Carbide Catalyze Hydrogen Evolution in both Acidic and Basic Solutions. *Angewandte Chemie International Edition*. 51, 12703-12706

63. Wirth, S., Harnisch, F., Weinmann, M., Schröder, U. (2012) Comparative study of IVB–VIB transition metal compound electrocatalysts for the hydrogen evolution reaction. *Applied Catalysis B: Environmental*. 126, 225-230
64. Wang, H., Gao, L. (2018) Recent developments in electrochemical hydrogen evolution reaction. *Current Opinion in Electrochemistry*. 7, 7-14
65. Xing, Z., Li, Q., Wang, D., Yang, X., Sun, X. (2016) Self-supported nickel nitride as an efficient high-performance three-dimensional cathode for the alkaline hydrogen evolution reaction. *Electrochimica Acta*. 191, 841-845
66. Hinnemann, B., Moses, P. G., Bonde, J., Jørgensen, K. P., Nielsen, J. H., Horch, S., Chorkendorff, I., Nørskov, J. K. (2005) Biomimetic Hydrogen Evolution: MoS_2 Nanoparticles as Catalyst for Hydrogen Evolution. *Journal of the American Chemical Society*. 127, 5308-5309
67. Jaramillo, T. F., Jørgensen, K. P., Bonde, J., Nielsen, J. H., Horch, S., Chorkendorff, I. (2007) Identification of Active Edge Sites for Electrochemical H_2 Evolution from MoS_2 Nanocatalysts. *Science*. 317, 100-102
68. Sultana, U. K., He, T., Du, A., O'Mullane, A. P. (2017) An amorphous dual action electrocatalyst based on oxygen doped cobalt sulfide for the hydrogen and oxygen evolution reactions. *RSC Advances*. 7, 54995-55004
69. García-Valenzuela, J. A. (2017) Simple Thiourea Hydrolysis or Intermediate Complex Mechanism? Taking up the Formation of Metal Sulfides from Metal–Thiourea Alkaline Solutions. *Comments on Inorganic Chemistry*. 37, 99-115
70. García, G., Rodríguez, J. L., Lacconi, G. I., Pastor, E. (2004) Spectroscopic Investigation of the Adsorption and Oxidation of Thiourea on Polycrystalline Au and Au(111) in Acidic Media. *Langmuir*. 20, 8773-8780
71. Bolzán, A. E., Wakenge, I. B., Salvarezza, R. C., Arvia, A. J. (1999) Electrochemical response of thiourea and formamidine disulphide on polycrystalline platinum in aqueous 0.5 M sulphuric acid. *Journal of Electroanalytical Chemistry*. 475, 181-189
72. Azzaroni, O., Andreasen, G., Blum, B., Salvarezza, R. C., Arvia, A. J. (2000) Scanning Tunneling Microscopy Studies of the Electrochemical Reactivity of Thiourea on Au(111) Electrodes. *The Journal of Physical Chemistry B*. 104, 1395-1398
73. Brunetti, V., Blum, B., Salvarezza, R. C., Arvia, A. J., Schilardi, P. L., Cuesta, A., Gayone, J. E., Zampieri, G. (2002) Scanning Tunneling Microscopy, Fourier Transform Infrared Reflection−Absorption Spectroscopy, and X-ray Photoelectron Spectroscopy of Thiourea Adsorption from Aqueous Solutions on Silver (111). *The Journal of Physical Chemistry B*. 106, 9831-9838
74. Su, X., Hatton, T. A. (2017) Electrosorption at functional interfaces: from molecular-level interactions to electrochemical cell design. *Physical Chemistry Chemical Physics*. 19, 23570-23584
75. Nicosia, C., Huskens, J. (2014) Reactive self-assembled monolayers: from surface functionalization to gradient formation. *Materials Horizons*. 1, 32-45
76. Luo, F., Li, J., Yuan, H., Xiao, D. (2014) Rapid synthesis of three-dimensional flower-like cobalt sulfide hierarchitectures by microwave assisted heating

method for high-performance supercapacitors. *Electrochimica Acta*. 123, 183-189
77. Kristl, M., Dojer, B., Gyergyek, S., Kristl, J. (2017) Synthesis of nickel and cobalt sulfide nanoparticles using a low cost sonochemical method. *Heliyon*. 3, e00273
78. Bao, S.-J., Li, Y., Li, C. M., Bao, Q., Lu, Q., Guo, J. (2008) Shape Evolution and Magnetic Properties of Cobalt Sulfide. *Crystal Growth & Design*. 8, 3745-3749
79. Wang, M., Anghel, A. M., Marsan, B., Cevey Ha, N.-L., Pootrakulchote, N., Zakeeruddin, S. M., Grätzel, M. (2009) CoS Supersedes Pt as Efficient Electrocatalyst for Triiodide Reduction in Dye-Sensitized Solar Cells. *Journal of the American Chemical Society*. 131, 15976-15977
80. Sun, Y., Liu, C., Grauer, D. C., Yano, J., Long, J. R., Yang, P., Chang, C. J. (2013) Electrodeposited Cobalt-Sulfide Catalyst for Electrochemical and Photoelectrochemical Hydrogen Generation from Water. *Journal of the American Chemical Society*. 135, 17699-17702
81. Huo, J., Zheng, M., Tu, Y., Wu, J., Hu, L., Dai, S. (2015) A high performance cobalt sulfide counter electrode for dye-sensitized solar cells. *Electrochimica Acta*. 159, 166-173
82. Zheng, L., Sun, X., Chen, L., Bao, C., Luo, W., Huang, N., Sun, P., Sun, Y., Fang, L., Wang, L. (2016) One-step in situ growth of Co_9S_8 on conductive substrate as an efficient counter electrode for dye-sensitized solar cells. *Journal of Materials Science*. 51, 4150-4159
83. Kim, H.-J., Kim, S.-W., Gopi, C. V. V. M., Kim, S.-K., Rao, S. S., Jeong, M.-S. (2014) Improved performance of quantum dot-sensitized solar cells adopting a highly efficient cobalt sulfide/nickel sulfide composite thin film counter electrode. *Journal of Power Sources*. 268, 163-170
84. Shengyuan, Y., Nair, A. S., Peining, Z., Ramakrishna, S. (2012) Electrospun TiO_2 nanostructures sensitized by CdS in conjunction with CoS counter electrodes: Quantum dot-sensitized solar cells all prepared by successive ionic layer adsorption and reaction. *Materials Letters*. 76, 43-46
85. Lin, J.-Y., Liao, J.-H., Chou, S.-W. (2011) Cathodic electrodeposition of highly porous cobalt sulfide counter electrodes for dye-sensitized solar cells. *Electrochimica Acta*. 56, 8818-8826
86. Ray, R. S., Sarma, B., Jurovitzki, A. L., Misra, M. (2015) Fabrication and characterization of titania nanotube/cobalt sulfide supercapacitor electrode in various electrolytes. *Chemical Engineering Journal*. 260, 671-683
87. Liu, T., Liang, Y., Liu, Q., Sun, X., He, Y., Asiri, A. M. (2015) Electrodeposition of cobalt-sulfide nanosheets film as an efficient electrocatalyst for oxygen evolution reaction. *Electrochemistry Communications*. 60, 92-96
88. Kornienko, N., Resasco, J., Becknell, N., Jiang, C.-M., Liu, Y.-S., Nie, K., Sun, X., Guo, J., Leone, S. R., Yang, P. (2015) Operando Spectroscopic Analysis of an Amorphous Cobalt Sulfide Hydrogen Evolution Electrocatalyst. *Journal of the American Chemical Society*. 137, 7448-7455
89. Swami, S. K., Chaturvedi, N., Kumar, A., Kapoor, R., Dutta, V., Frey, J., Moehl, T., Grätzel, M., Mathew, S., Nazeeruddin, M. K. (2015) Investigation of

electrodeposited cobalt sulphide counter electrodes and their application in next-generation dye sensitized solar cells featuring organic dyes and cobalt-based redox electrolytes. *Journal of Power Sources*. 275, 80-89
90. Lin, J.-Y., Liao, J.-H. (2011) Mesoporous Electrodeposited-CoS Film as a Counter Electrode Catalyst in Dye-Sensitized Solar Cells. *Journal of The Electrochemical Society*. 159, D65-D71
91. Huo, J., Wu, J., Zheng, M., Tu, Y., Lan, Z. (2015) Effect of ammonia on electrodeposition of cobalt sulfide and nickel sulfide counter electrodes for dye-sensitized solar cells. *Electrochimica Acta*. 180, 574-580
92. Karim, N. A., Ludin, N. A., Mat-Teridi, M. A., Sepeai, S., Ibrahim, M. A., Kouhnavard, M., Sopian, K., Arakawa, H. (2018) Effects of deposition time on of cobalt sulfide thin film electrode formation. *Malaysian Journal of Analytical Sciences*. 22, 80-86
93. Tran, P. D., Tran, T. V., Orio, M., Torelli, S., Truong, Q. D., Nayuki, K., Sasaki, Y., Chiam, S. Y., Yi, R., Honma, I., Barber, J., Artero, V. (2016) Coordination polymer structure and revisited hydrogen evolution catalytic mechanism for amorphous molybdenum sulfide. *Nature materials*. 15, 640-646
94. Saji Viswanathan, S., Lee, C. W. (2012) Molybdenum, Molybdenum Oxides, and their Electrochemistry. *ChemSusChem*. 5, 1146-1161
95. Morales-Guio, C. G., Hu, X. (2014) Amorphous Molybdenum Sulfides as Hydrogen Evolution Catalysts. Accounts of Chemical Research. 47, 2671-2681
96. Aliyev, A. S., Elrouby, M., Cafarova, S. F. (2015) Electrochemical synthesis of molybdenum sulfide semiconductor. *Materials Science in Semiconductor Processing*. 32, 31-39
97. Bouroushian, M. (2010) *Electrochemistry of Metal Chalcogenides*. Springer
98. Merki, D., Fierro, S., Vrubel, H., Hu, X. (2011) Amorphous molybdenum sulfide films as catalysts for electrochemical hydrogen production in water. *Chemical Science*. 2, 1262-1267
99. Vrubel, H., Hu, X. (2013) Growth and Activation of an Amorphous Molybdenum Sulfide Hydrogen Evolving Catalyst. *ACS Catalysis*. 3, 2002-2011
100. Redman, D. W., Rose, M. J., Stevenson, K. J. (2017) Electrodeposition of Amorphous Molybdenum Chalcogenides from Ionic Liquids and Their Activity for the Hydrogen Evolution Reaction. *Langmuir*. 33, 9354-9360
101. Morales-Guio Carlos, G., Liardet, L., Mayer Matthew, T., Tilley, S. D., Grätzel, M., Hu, X. (2014) Photoelectrochemical Hydrogen Production in Alkaline Solutions Using Cu_2O Coated with Earth-Abundant Hydrogen Evolution Catalysts. *Angewandte Chemie International Edition*. 54, 664-667
102. Kendall, B., Dahl, T. W. and Anbar, A. D. (2017) The stable isotope geochemistry of molybdenum. *Reviews in Mineralogy and Geochemistry*. 82, 683-732
103. Chandra, S., Sahu, S. N. (1984) Electrodeposited semiconducting molybdenum selenide films. I. Preparatory technique and structural characterisation. *Journal of Physics D: Applied Physics*. 17, 2115-2123

104. Dukstiene, N., Kazancev, K., Prosicevas, I., Guobiene, A. (2004) Electrodeposition of Mo-Se thin films from a sulfamatic electrolyte. *Journal of Solid State Electrochemistry*. 8, 330-336
105. Ponomarev, E. A., Neumann-Spallart, M., Hodes, G., Lévy-Clément, C. (1996) Electrochemical deposition of MoS_2 thin films by reduction of tetrathiomolybdate. *Thin Solid Films*. 280, 86-89
106. Ghosh, S. K., Bera, T., Karacasu, O., Swarnakar, A., Buijnsters, J. G., Celis, J. P. (2011) Nanostructured MoS_x-based thin films obtained by electrochemical reduction. *Electrochimica Acta*. 56, 2433-2442
107. Li, Q., Walter, E. C., van der Veer, W. E., Murray, B. J., Newberg, J. T., Bohannan, E. W., Switzer, J. A., Hemminger, J. C., Penner, R. M. (2005) Molybdenum Disulfide Nanowires and Nanoribbons by Electrochemical/ Chemical Synthesis. *The Journal of Physical Chemistry B*. 109, 3169-3182
108. Chianelli, R. R., Berhault, G., Torres, B. (2009) Unsupported transition metal sulfide catalysts: 100 years of science and application. *Catalysis Today*. 147, 275-286
109. Staszak-Jirkovský, J., Malliakas, Christos D., Lopes, Pietro P., Danilovic, N., Kota, Subrahmanyam S., Chang, K.-C., Genorio, B., Strmcnik, D., Stamenkovic, Vojislav R., Kanatzidis, M. G., Markovic, N. M. (2015) Design of active and stable Co–Mo–S_x chalcogels as pH-universal catalysts for the hydrogen evolution reaction. *Nature Materials*. 15, 197-203
110. Hou, J., Lei, Y., Wang, F., Ma, X., Min, S., Jin, Z., Xu, J. (2017) In-situ photochemical fabrication of transition metal-promoted amorphous molybdenum sulfide catalysts for enhanced photosensitized hydrogen evolution. *International Journal of Hydrogen Energy*. 42, 11118-11129
111. Liu, Y.-R., Shang, X., Gao, W.-K., Dong, B., Chi, J.-Q., Li, X., Yan, K.-L., Chai, Y.-M., Liu, Y.-Q., Liu, C.-G. (2017) Ternary CoS_2/MoS_2/RGO electrocatalyst with CoMoS phase for efficient hydrogen evolution. *Applied Surface Science*. 412, 138-145
112. Bose, R., Jin, Z., Shin, S., Kim, S., Lee, S., Min, Y.-S. (2017) Co-catalytic Effects of CoS_2 on the Activity of the MoS_2 Catalyst for Electrochemical Hydrogen Evolution. *Langmuir*. 33, 5628-5635
113. Dai, X., Du, K., Li, Z., Liu, M., Ma, Y., Sun, H., Zhang, X., Yang, Y. (2015) Co-Doped MoS_2 Nanosheets with the Dominant CoMoS Phase Coated on Carbon as an Excellent Electrocatalyst for Hydrogen Evolution. *ACS Applied Materials & Interfaces*. 7, 27242-27253
114. Li, Y., Zhang, H., Jiang, M., Kuang, Y., Wang, H., Sun, X. (2016) Amorphous Co-Mo-S ultrathin films with low-temperature sulfurization as high-performance electrocatalysts for the hydrogen evolution reaction. *Journal of Materials Chemistry A*. 4, 13731-13735
115. Liu, Y.-R., Shang, X., Gao, W.-K., Dong, B., Li, X., Li, X.-H., Zhao, J.-C., Chai, Y.-M., Liu, Y.-Q., Liu, C.-G. (2017) In situ sulfurized CoMoS/$CoMoO_4$ shell-core nanorods supported on N-doped reduced graphene oxide (NRGO) as efficient electrocatalyst for hydrogen evolution reaction. *Journal of Materials Chemistry A*. 5, 2885-2896

116. Merki, D., Vrubel, H., Rovelli, L., Fierro, S., Hu, X. (2012) Fe, Co, and Ni ions promote the catalytic activity of amorphous molybdenum sulfide films for hydrogen evolution. *Chemical Science*. 3, 2515-2525
117. Shen, X., Xia, X., Ye, W., Du, Y., Wang, C. (2017) Hexagram-like CoS-MoS_2 composites with enhanced activity for hydrogen evolution reaction. *Journal of Solid State Electrochemistry*. 21, 409-417
118. Zhang, N., Ma, W., Jia, F., Wu, T., Han, D., Niu, L. (2016) Controlled electrodeposition of $CoMoS_x$ on carbon cloth: A 3D cathode for highly-efficient electrocatalytic hydrogen evolution. *International Journal of Hydrogen Energy*. 41, 3811-3819
119. Premnath, K., Theerthagiri, J., Madhavan, J., Arunachalam, P., Ghanem, M. A., Al-Mayouf, A. M. (2018) Electrodeposited $Co_{1-x}Mo_xS$ thin films as highly efficient electrocatalysts for hydrogen evolution reaction in acid medium. *Journal of Solid State Electrochemistry*. 22, 2641-2647
120. Palomar-Pardavé, M., Scharifker, B. R., Arce, E. M., Romero-Romo, M. (2005) Nucleation and diffusion-controlled growth of electroactive centers: Reduction of protons during cobalt electrodeposition. *Electrochimica Acta*. 50, 4736-4745
121. Haynes, W. M. (2012) *CRC Handbook of Chemistry and Physics*, 93rd Edition. Taylor & Francis Inc, Bosa Roca, United States
122. Santos, J. S., Matos, R., Trivinho-Strixino, F., Pereira, E. C. (2007) Effect of temperature on Co electrodeposition in the presence of boric acid. *Electrochimica Acta*. 53, 644-649
123. Badawy, W. A., Al-Kharafi, F. M., Al-Ajmi, J. R. (2000) Electrochemical behaviour of cobalt in aqueous solutions of different pH. *Journal of Applied Electrochemistry*. 30, 693-704
124. Wang, X., Ding, J., Yao, S., Wu, X., Feng, Q., Wang, Z., Geng, B. (2014) High supercapacitor and adsorption behaviors of flower-like MoS_2 nanostructures. *Journal of Materials Chemistry A*. 2, 15958-15963
125. Pandey, K., Yadav, P., Singh, D., Gupta, S. K., Sonvane, Y., Lukačević, I., Kim, J., Kumar, M. (2016) First step to investigate nature of electronic states and transport in flower-like MoS_2: Combining experimental studies with computational calculations. *Scientific Reports*. 6, 32690
126. Zhang, X. H., Wang, C., Xue, M. Q., Lin, B. C., Ye, X., Lei, W. N. (2016) Hydrothermal synthesis and characterization of ultrathin MoS_2 nanosheets. *Chalcogenide Letters*. 13, 27-34
127. Fikret Cafarova, S., Shikhan Aliyev, A., Elrouby, M., Soltanova, N., Babir Tagiyev, D. (2015) Studying the electrochemical deposition process of molybdenum from aqueous solution of molybdate ions. *Journal of Electrochemical Science and Engineering*. 5, 231-235
128. Skwarek, E., Khalameida, S., Janusz, W., Sydorchuk, V., Konovalova, N., Zazhigalov, V., Skubiszewska-Zięba, J., Leboda, R. (2011) Influence of mechanochemical activation on structure and some properties of mixed vanadium–molybdenum oxides. *Journal of Thermal Analysis and Calorimetry*. 106, 881-894

129. Özcan, M., Dehri, İ., Erbil, M. (2004) Organic sulphur-containing compounds as corrosion inhibitors for mild steel in acidic media: correlation between inhibition efficiency and chemical structure. *Applied Surface Science*. 236, 155-164
130. Popczun, E. J., McKone, J. R., Read, C. G., Biacchi, A. J., Wiltrout, A. M., Lewis, N. S., Schaak, R. E. (2013) Nanostructured Nickel Phosphide as an Electrocatalyst for the Hydrogen Evolution Reaction. *Journal of the American Chemical Society*. 135, 9267-9270
131. de Castro Isabela, A., Datta Robi, S., Ou Jian, Z., Castellanos-Gomez, A., Sriram, S., Daeneke, T., Kalantar-zadeh, K. (2017) Molybdenum Oxides – From Fundamentals to Functionality. *Advanced Materials*. 29, 1701619
132. Maheshwari, N., Muralidharan, G. (2017) Controlled synthesis of nanostructured molybdenum oxide electrodes for high performance supercapacitor devices. *Applied Surface Science*. 416, 461-469
133. Kumar, V., Sundararajan, R. (2015) Optical, Thermal and Nonlinear Properties of Tristhiourea Lanthanum Nitrate. *Journal of Minerals and Materials Characterization and Engineering*. 3, 118-124
134. Tian, H., Roberts, C. A., Wachs, I. E. (2010) Molecular Structural Determination of Molybdena in Different Environments: Aqueous Solutions, Bulk Mixed Oxides, and Supported MoO_3 Catalysts. *The Journal of Physical Chemistry C*. 114, 14110-14120
135. Windom, B. C., Sawyer, W. G., Hahn, D. W. (2011) A Raman Spectroscopic Study of MoS_2 and MoO_3: Applications to Tribological Systems. *Tribology Letters*. 42, 301-310
136. Patil, R. S., Uplane, M. D., Patil, P. S. (2006) Structural and optical properties of electrodeposited molybdenum oxide thin films. *Applied Surface Science*. 252, 8050-8056
137. Theerthagiri, J., Senthil, R. A., Buraidah, M. H., Madhavan, J., Arof, A. K., Ashokkumar, M. (2016) One-step electrochemical deposition of $Ni_{1-x}Mo_xS$ ternary sulfides as an efficient counter electrode for dye-sensitized solar cells. *Journal of Materials Chemistry A*. 4, 16119-16127
138. Huang, J. H., Kargl-Simard, C., Oliazadeh, M., Alfantazi, A. M. (2004) pH-Controlled precipitation of cobalt and molybdenum from industrial waste effluents of a cobalt electrodeposition process. *Hydrometallurgy*. 75, 77-90
139. Shang, X., Dong, B., Chai, Y.-M., Liu, C.-G. (2018) In-situ electrochemical activation designed hybrid electrocatalysts for water electrolysis. *Science Bulletin*. 63, 853-876
140. Yang, C., Gao, M. Y., Zhang, Q. B., Zeng, J. R., Li, X. T., Abbott, A. P. (2017) In-situ activation of self-supported 3D hierarchically porous Ni_3S_2 films grown on nanoporous copper as excellent pH-universal electrocatalysts for hydrogen evolution reaction. *Nano Energy*. 36, 85-94
141. Chia, X., Ambrosi, A., Sofer, Z., Luxa, J., Pumera, M. (2015) Catalytic and Charge Transfer Properties of Transition Metal Dichalcogenides Arising from Electrochemical Pretreatment. *ACS Nano*. 9, 5164-5179
142. Voiry, D., Fullon, R., Yang, J., de Carvalho Castro e Silva, C., Kappera, R., Bozkurt, I., Kaplan, D., Lagos, M. J., Batson, P. E., Gupta, G., Mohite, Aditya D.,

Dong, L., Er, D., Shenoy, V. B., Asefa, T., Chhowalla, M. (2016) The role of electronic coupling between substrate and 2D MoS_2 nanosheets in electrocatalytic production of hydrogen. *Nature Materials*. 15, 1003-1009

143. Safizadeh, F., Ghali, E., Houlachi, G. (2015) Electrocatalysis developments for hydrogen evolution reaction in alkaline solutions – A Review. *International Journal of Hydrogen Energy*. 40, 256-274
144. Jayabal, S., Saranya, G., Wu, J., Liu, Y., Geng, D., Meng, X. (2017) Understanding the high-electrocatalytic performance of two-dimensional MoS_2 nanosheets and their composite materials. *Journal of Materials Chemistry A*. 5, 24540-24563
145. Zhang, H., Li, Y., Xu, T., Wang, J., Huo, Z., Wan, P., Sun, X. (2015) Amorphous Co-doped MoS_2 nanosheet coated metallic CoS_2 nanocubes as an excellent electrocatalyst for hydrogen evolution. *Journal of Materials Chemistry A*. 3, 15020-15023
146. Gisbert, R., García, G., Koper, M. T. M. (2010) Adsorption of phosphate species on poly-oriented Pt and Pt(111) electrodes over a wide range of pH. *Electrochimica Acta*. 55, 7961-7968
147. Kanan, M. W., Nocera, D. G. (2008) In Situ Formation of an Oxygen-Evolving Catalyst in Neutral Water Containing Phosphate and Co^{2+}. *Science*. 321, 1072-1075

LIST OF PUBLICATIONS ON THE THEME OF DISSERTATION

Publications on the dissertation topic in the journals of the main list of *Clarivate Analytics Web of Science* database

1. Mardosaite, R., Valatka, E. (2019). Electrochemical deposition of S-containing molybdenum oxide films for pH neutral hydrogen evolution. International Journal of Electrochemical Science 14 (1), 387–401. ISSN 1452-3981

2. Mardosaitė, R., Valatka, E. (2017). Structure and electrocatalytic properties of amorphous cobalt–sulphide films on fto substrate. Chalcogenide Letters, 14(5), 171-179. ISSN 1584-8663

3. Ostachavičiūtė, S., Mardosaitė, R., Valatka, E. (2014). Photoelectrochemical behavior of WO_3 and TiO_2 films modified with cobalt-based oxygen evolution catalyst. Chemija: mokslo darbai, 25(3), 154-160. ISSN 0235-7216

Publications in Proceedings of Conferences

1. Valatka, E., Mardosaitė, R., Dukštienė, N., Ancutienė, I. (2017). Synthesis and activity of cobalt-sulfide electrocatalysts for photoelectrochemical water splitting. In 21st Topical Meeting of the International Society of Electrochemistry [e-resource]: Photoelectrochemistry of semiconductors at the nanoscale: from fundamental aspects to practical applications, 23-26 April 2017, Szeged, Hungary

2. Mardosaitė, R., Gustainis, V., Valatka, E. (2017). Structure and morphology of Co-Mo-S films electrodeposited on FTO substrate. In Chemistry and chemical technology 2017: proceedings of the international conference, April 28th, 2017, Kaunas: Kauno technologijos universitetas. ISSN 25387359

3. Mardosaitė, R., Valatka, E. (2016). Structure and properties of electrodeposited cobalt sulfide catalyst. In Chemistry and chemical technology: international conference of Lithuanian Society of Chemistry: Lithuanian Academy of Science, Vilnius, Lithuania, April 28-29, 2016: book of abstracts. ISBN 9786099551135

SL344. 2019-01-21, 12,5 leidyb. apsk. l. Tiražas 14 egz. Užsakymas *22*.
Išleido Kauno technologijos universitetas, K. Donelaičio g. 73, 44249 Kaunas
Spausdino leidyklos „Technologija“ spaustuvė, Studentų g. 54, 51424 Kaunas